A Detailed Analysis of Guard-Heated Wall Shear Stress Sensors for Turbulent Flows

by

Seyed Ali Ale Etrati Khosroshahi
B.Sc., University of Tehran, 2011

A Thesis Submitted in Partial Fulfilment of the
Requirements for the Degree of

MASTER OF APPLIED SCIENCE

in the Department of Mechanical Engineering

University of Victoria

A Detailed Analysis of Guard-Heated Wall Shear Stress Sensors for Turbulent Flows

by

Seyed Ali Ale Etrati Khosroshahi
B.Sc., University of Tehran, 2011

Supervisory Committee

Dr. Rustom Bhiladvala, Supervisor
(Department of Mechanical Engineering)

Dr. Curran Crawford, Departmental Member
(Department of Mechanical Engineering)

Dr. Nedjib Djilali, Departmental Member
(Department of Mechanical Engineering)

Supervisory Committee

Dr. Rustom Bhiladvala, Supervisor
(Department of Mechanical Engineering)

Dr. Curran Crawford, Departmental Member
(Department of Mechanical Engineering)

Dr. Nedjib Djilali, Departmental Member
(Department of Mechanical Engineering)

ABSTRACT

This thesis presents a detailed, two-dimensional analysis of the performance of multi-element guard-heated hot-film wall shear stress microsensors for turbulent flows. Previous studies of conventional, single-element sensors show that a significant portion of heat generated in the hot-film travels through the substrate before reaching the fluid, causing spectral and phase errors in the wall shear stress signal and drastically reducing the spatial resolution of the sensor. Earlier attempts to reduce these errors have focused on reducing the effective thermal conductivity of the substrate. New guard-heated microsensor designs proposed to overcome the severe deficiencies of the conventional design are investigated in this thesis. Guard-heaters remove the errors associated with substrate heat conduction, by forcing zero temperature gradient at the edges and bottom face of the hot-film, and hence, block the indirect heat transfer to the flow. Air and water flow over the sensors are studied numerically to investigate design, performance and signal strength of the guard-heated sensors. Our results show, particularly for measurements in low-conductivity fluids such as air, that edge guard-heating needs to be supplemented by a sub-surface guard-heater, to make substrate conduction errors negligible. With this two-plane guard-heating, a strong non-linearity in the standard single-element designs can be corrected, and spectral and phase errors arising from substrate conduction can be eliminated.

Contents

List of Tables

List of Figures

NOMENCLATURE

ACRONYMS

CTA	Constant Temperature Anemometry
$GH1P$	Single-Plane Guard-Heated
$GH2P$	Two-Plane Guard-Heated
SE	Single-Element
TCR	Temperature Coefficient of Resistance
WSS	Wall Shear Stress

SYMBOLS

A	Amplitude, Constant	$-$
C	Thermal Capacity	$JkgK^{-1}$
D	Pipe Diameter	m
E	Electrical Potential	V
Gr	Grashof Number	$-$
g	Acceleration Due to Earth's Gravity	ms^{-2}
h	Convection Coefficient	$Wm^{-2}K^{-1}$
I	Electrical Current	A
K	$(k_f/k_s)^2(\alpha_s/\alpha_f)$	$-$
k	Thermal Conductivity	$Wm^{-1}K^{-1}$
L	Hot-Film Length	m
Nu	Nusselt Number	$-$
Pe	Peclet Number	$-$

Pr	Prandtl Number	$-$
Q	Heat Transfer Rate	W
R	Electrical Resistance	Ω
Re_D	Pipe Reynolds Number	$-$
s	Shear Rate	s^{-1}
T	Temperature	K
t	Time Coordinate	s
U	Pipe Velocity	ms^{-1}
u	Streamwise Velocity	ms^{-1}
u_τ	Friction Velocity	ms^{-1}
v	Wall-Normal Velocity	ms^{-1}
W	Hot-Film Width	m
w	Spanwise Velocity	ms^{-1}
x	Streamwise Spatial Coordinate	m
y	Wall-Normal Spatial Coordinate	m
z	Spanwise Spatial Coordinate	m

GREEK

α	Thermal Diffusivity, Temperature Coefficient of Resistance	m^2s^{-1},K^{-1}
β	Volumetric Thermal Expansion Coefficient	K^{-1}
δ_t	Thermal Boundary Layer Thickness	m
θ	Dimensionless Temperature	$-$

μ	Dynamic Viscosity	$kgm^{-1}s^{-1}$
ν	Kinematic Viscosity	m^2s^{-1}
ρ	Density	kgm^{-3}
τ_w	Wall Shear Stress	Pa
ϕ	Phase	$^\circ$
ω	Frequency of shear fluctuation	s^{-1}
ω^*	Dimensionless Frequency	$-$
ω_η	Kolmogorov Frequency	s^{-1}

SUPERSCRIPTS

$'$	Dimensionless Parameter, Per Unit Depth
$+$	Non-Dimensionalized in Wall-Units

SUBSCRIPTS

a	Air
F, f	Fluid
h	hot
lev	Leveque Solution
S, s	Substrate
w	Water

ACKNOWLEDGEMENTS

First and foremost I would like to thank my supervisor, Rustom Bhiladvala, for giving me the opportunity to pursue MASc degree at University of Victoria. I am grateful to him for sharing his deep knowledge on turbulence and thermal anemometry with me, being patient, trusting and supportive when work was slowed down or stalled and believing in me, making me more confident.

I am also grateful to my dear friends in Victoria, Nima, Sahar, Elsa and Azadeh, with whom I have great memories of laughter, eating and drinking tea. I have to thank them, especially Nima, for listening to me complaining about everything for several hours. Golnoosh, Hamidreza and Ghazal, Alireza and Mahkameh, Elham, Navid and Azadeh, welcomed me whenever I went to Vancouver and made me feel like home from the first days of my arrival in Canada. My officemates Jean, Oliver and Tom made the long rainy days tolerable and the sunny days more exciting.

I would also like to thank my best friend Sahra, for being by my side at all times and supporting me in the low moments. My friends Sepehr, Sam and Mahsa shared their love and support from very long distances, and did not let me feel alone for one second.

Last but not least, I have to thank my parents, Abbas and Malak, and my sisters, Aydin and Samira, for educating me, supporting me, teaching me to be a good person and always being there for me.

DEDICATION

I want to dedicate this thesis to my beloved parents, who have supported me in every step of my life, and have done everything they could for me without any reservations.

Chapter 1

Introduction

1.1 Overview

Accurate measurement of wall shear stress (WSS) provides a direct measure of the tangential fluid force on a solid surface, which is a crucial missing piece in our knowledge of wall-bounded turbulent flow. An accurate quantitative model relating wall shear stress, pressure and turbulent velocity fields very close to the wall, would increase our ability to understand, predict and control turbulence significantly.

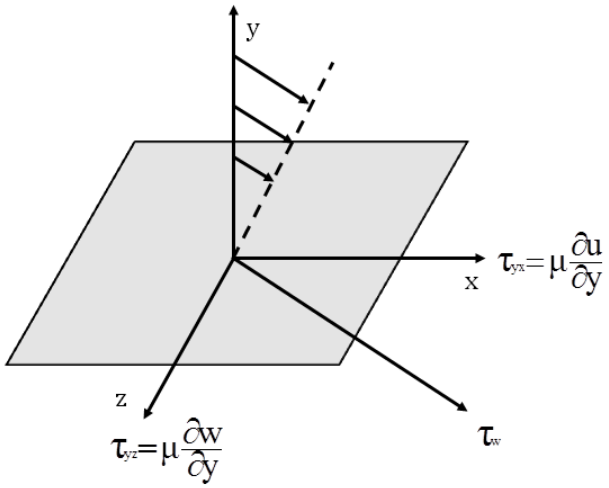

Figure 1.1: Schematic of wall shear stress vector and its components.

Wall shear stress is a result of the viscous drag force exerted by a fluid passing over a solid surface. At relatively low Reynolds numbers, when the flow regime is laminar, the value of wall shear stress τ_w can be obtained by knowing the velocity

profile as

$$\tau_w = \mu \left. \frac{\partial V}{\partial y} \right|_{y=0}, \tag{1.1}$$

where μ is the fluid viscosity, V is the velocity and y is the wall-normal direction. Mean wall shear stress $\overline{\tau}_w$ is the basis for velocity scale $u_\tau = (\overline{\tau}_w/\rho)^{1/2}$ called friction velocity (also shown as u^*), in wall-bounded turbulent flows. Its role in the collapse of the mean velocity profiles in different regions of wall-bounded turbulent flow gives it a central place in theory for wall turbulence.

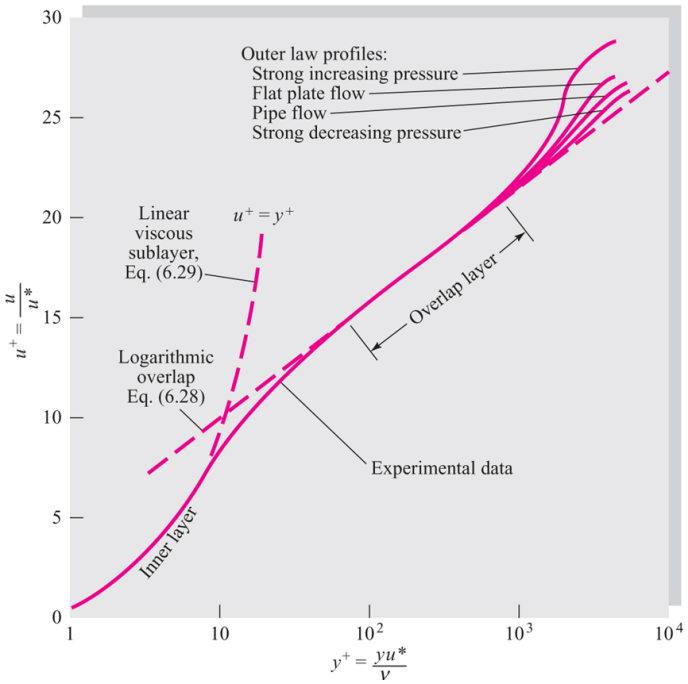

Figure 1.2: Mean velocity profiles near the wall including inner, outer and overlap layer laws in turbulent flows. Picture reproduced by permission from [1].

In turbulent flows, wall shear stress fluctuates with a large range of frequencies. Fluctuations in wall shear stress $\tau_w^{'}$ are defined as the deviation of the instantaneous value τ_w from average wall shear stress $\overline{\tau}_w$

$$\tau_w^{'} = \tau_w - \overline{\tau}_w. \tag{1.2}$$

It has been found that streamwise vortices are responsible for "sweep" and "ejection" events, resulting in fluctuations in the near-wall velocity and wall shear stress [2, 3, 4]. These streamwise vortices transport high momentum fluid to the low momentum region near the wall and thus result in sudden "kicks" in streamwise wall shear stress

fluctuations. As a result, compared to velocity fluctuations, probability distribution functions (PDF) show that fluctuations of wall shear stress which are much stronger than the mean value, occur far more frequently than those described by a normal (Gaussian) distribution. These strong fluctuations, although less frequent compared to the weaker fluctuations, could have much more significant effects, for instance on structural loads on wind turbines or sediment transport and erosion in riverbanks.

Turbulent flows are prevalent in most engineering applications, industrial processes and in nature. Flow around aircraft, cars and wind turbines, buildings, in pipe flows, large blood vessels and heat exchangers as well as flow responsible for sediment or sand transport, are all examples of turbulent flows. Numerical solution of Reynolds-averaged Navier-Stokes equations (RANS), obtained by time-averaging the Navier-Stokes equations, is commonly used to model turbulent flows, especially in engineering applications. Models for RANS equations do not provide accurate results, possibly due to inadequate boundary conditions. Direct Numerical Simulations (DNS) are the most accurate numerical tools as they resolve all scales in the flow without any modelling for the near-wall flow. They are, however, limited to low Reynolds numbers and simple flows due to high computational cost. Large Eddy Simulations (LES) are computationally less expensive than DNS. Their computational cost and accuracy relies on the wall-models they use to resolve the near-wall region. Piomelli *et al.*(2008) provides a review of accuracy and computational cost of different wall-layer models [5]. Resolving the near-wall region, in which the numerical errors are largest, greatly increases the CPU time of LES. Thus an accurate relation must be found to relate the wall shear stress to outer-layer flow [6]. Simultaneous wall shear/velocity measurements would help us obtain more accurate boundary conditions for numerical simulation of turbulent flows.

Direct measurement of wall shear stress, or numerical simulation with wall-models improved from experimental data, would greatly help us to enhance our designs for better performance and efficiency. Furthermore, manipulating the turbulent flow near the wall can have beneficial results. Environmental and energy saving concerns have resulted in a great focus on developing efficient active flow control systems to control turbulence to achieve drag reduction, separation delay, vibration suppression, flow-induced noise reduction and turbulent mixing and heat transfer enhancement [7, 2, 8]. Spatially distributed values of the instantaneous wall shear stress can be used in a feedback control loop to effect beneficial changes in the turbulent boundary layer [9]. Using active flow control systems for energy saving through drag reduction,

requires accurate wall shear stress sensors with high spatial and temporal resolution. Turbulence and flow separation effects leading to difficulties in aircraft control or shock loading in wind turbines could be better controlled through understanding and direct measurement of wall shear stress. For instance, wind turbine active control ("smart rotor") systems using measurement of wind-induced blade surface forces, could help combat stall, reduce fatigue and extreme load failures as well as power fluctuations. Various extensive reviews of the broad subject of flow control are already available [4, 10, 11, 12].

The measurement of turbulent wall shear stress, particularly at high Reynolds numbers has proved challenging. These fluctuations represent a change in velocity gradient in a region that may be limited to a few microns in thickness. Several methods have been developed and used and several new principles are being tried for wall shear stress measurements, such as floating-element probes [13, 14, 15], micro-pillars [16], optical methods [17] and electrochemical [18] and thermal sensors [9, 13, 19, 20, 21].

Thermal sensing using constant temperature anemometry (CTA) has provided a significant portion of the experimental data on which quantitative models in turbulence are based, due to an early achievement of high spatial and temporal resolution and insensitivity to pressure fluctuations. Conventional single-element hot-film sensors for wall shear stress measurement, consist of a single film flush-mounted on a solid wall and kept at a fixed temperature difference over that of fluid. Such wall shear stress sensors present in addition, the advantages of being non-intrusive and not prone to fouling and contamination. In spite of all these advantages, these sensors suffer from severe errors due to unwanted heat transfer to the substrate. This heat, which eventually goes to the fluid, introduces a coupled set of unacceptably large flow dependent errors in measurement of wall shear stress. The idea of using a guard-heater to block this unwanted heat transfer has led to a new hot-film design. In this thesis, we investigate to what extent this new sensor design will help us eliminate the effects of substrate heat conduction from the sensor signal and thus enable accurate wall shear stress measurements even for the particularly challenging case of thermal measurement of wall shear stress in low conductivity fluids such as air.

1.2 Purpose of This Thesis

In this thesis, we investigate the guard-heated hot-film wall shear stress microsensor, a novel design proposed to overcome some of the most severe sources of errors and uncertainties associated with the conventional single-element hot-film sensors. A numerical model is built to study static and dynamic behaviour of the new design and compare its performance to the conventional hot-film sensor. Although the sensor is designed for measurements in turbulent flows, turbulence is not modelled in this work. Instead, following the common practice for studying hot-film sensors, a simple, two-dimensional flow with an instantaneously linear velocity profile, with slope allowed to change harmonically, is used. The amplitude and phase lag of the heat transfer to harmonic shear is studied over a range of frequencies. This simple model enables us to compare the new design to the conventional design and study the deviations from the calibration equation used for hot-film sensors. A few known turbulent flow characteristics are used to constrain the thermal transport of the simplified model. This prevents the introduction of significant deviations from the simplified model when the probe is operated in a turbulent flow.

Although the primary purpose of this work is to examine the improvements of the new design over the conventional hot-film sensors, we wish to provide a more practical study of wall shear stress measurement using hot-film sensors. As we will show in the next chapter, a single sensor size cannot provide accurate measurements in all flows. We try to provide a guideline for the reader, to become aware of the limits of the hot-film sensors, and be able to choose a sensor size suited for measurements in given flow conditions. To do this, it is necessary to start with the equations governing the conjugate heat transfer. We will show that we can quantify several limits of these sensors, and even make predictions for their frequency response, analytically. Our detailed numerical calculations provide further details while confirming the predictions of analysis and validate the choice of non-dimensional parameters used in the analysis. These details allow us to see how each of these limits depend on physical quantities, such as the sensor size, the shear rate, etc., and thus yield practical information useful for selecting probes appropriate to flow conditions.

1.3 Thesis Outline

In this Chapter, we have provided an introduction to the work in this thesis, the motivation behind our work, and the objectives.

In Chapter 2, we introduce thermal sensors and anemometers, describe how they work and what are the advantages and disadvantages over other wall shear stress sensing principles. We also briefly explain the difficulties of accurate wall shear stress measurements associated with conventional, single-element hot-film sensors. Next, we introduce our proposed guard-heated design, and describe what improvements over the singe-element design we wish to achieve.

Chapter 3 contains a detailed analysis of the equations, governing conjugate heat transfer in the fluid and solid, and list the assumptions made to derive the sensor calibration equation from them. The analysis provides a quantitative map to organize the operational limits and errors of conventional hot-film sensors, which we wish to remove with the new design. The analysis is carried out using appropriate non-dimensional parameters. A translation of these limits to dimensional variables in the case of fully-developed pipe flow is also provided, to help the reader understand the real-world limitations of a single-element hot-film sensors.

In Chapter 4 we introduce the numerical model and explain the methods used to examine the performance of the new guard-heated design, using both steady and unsteady calculations to determine the response to the frequency and amplitude of applied harmonic shear stress. We evaluate the improvements over the conventional single-element hot-film sensor designs and compare the results to our predictions from the analysis results presented in Chapter 3.

Chapter 5 contains a summary of this work, conclusions and recommendations for future work.

Chapter 2

Turbulent Wall Shear Stress Sensing

2.1 Thermal Sensors for Turbulent Flows

Thermal sensors using Constant Temperature Anemometry (CTA), measure turbulent fluctuations by sensing the changes in heat transfer from a small, electrically heated sensing element exposed to the fluid motion. Their small size allows high spatial resolution and frequency response, which makes them especially suitable for studying details in turbulent flows [22], and a considerable fraction of turbulence theory relies on velocity field data measured by CTA for its basis.

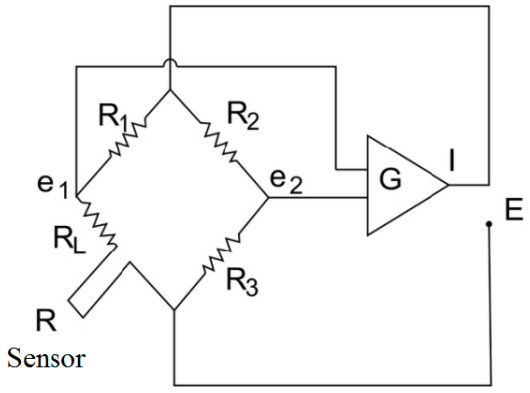

Figure 2.1: A Wheatstone bridge with a fast servo-amplifier is used in a CTA, to maintain the sensor temperature constant.

A simple thermal anemometer is shown in Figure 2.1. The electrical resistance R of the sensor can be represented by

$$R = R_{ref}[1 + \alpha(T_h - T_{ref})], \tag{2.1}$$

where R_{ref} is resistance at reference temperature T_{ref}, T_h is the chosen constant sensor temperature and α is Temperature Coefficient of Resistance (TCR). In CTA, the sensor is kept at a constant electrical resistance, and hence, a constant temperature, higher than the fluid temperature. This is done using a Wheatstone bridge with a fast servo-amplifier. A stronger flow fluctuation, takes away more heat from the sensor. Sensor materials, typically chosen with high TCR, begin to change the resistance R, and hence potential difference $(e_1 - e_2)$ in Figure 2.1. This change is used as the input to the fast servo-amplifier, which increases the current to restore $(e_1 - e_2)$, R and probe temperature at their set constant values. The response of the circuit is typically much faster than the fastest fluctuation in the flow. The fluctuations in the current I passing through the sensor are saved. Since the heat taken away from the sensor by the fluid flow, is equal to the heat generated in the sensor, which is equal to I^2R, we can translate the recorded values of I, using a suitable calibration equation, to fluctuations in the flow field.

The sensor used in the thermal anemometry system can be either a hot-wire or a hot-film. Each of these designs has been used for both velocity and WSS sensing. Thermal sensors are categorized as indirect methods [23], as they indirectly measure WSS or velocity by measuring the heat transfer rate and using established correlations between the flow field in the vicinity of the device and the heat transfer.

2.2 Conventional Single-Element Hot-Film Sensors for WSS

Sensors made as single hot-films, flush-mounted with the wall, have several characteristics desired from an ideal WSS sensor. They are non-intrusive, the low thermal inertia of thin films allows high-frequency response, they can be small in size to enable good spatial resolution, they are insensitive to pressure variations and not prone to dust contamination or fouling.

Figure 2.2 shows a schematic of a conventional hot-film sensor, consisting of a

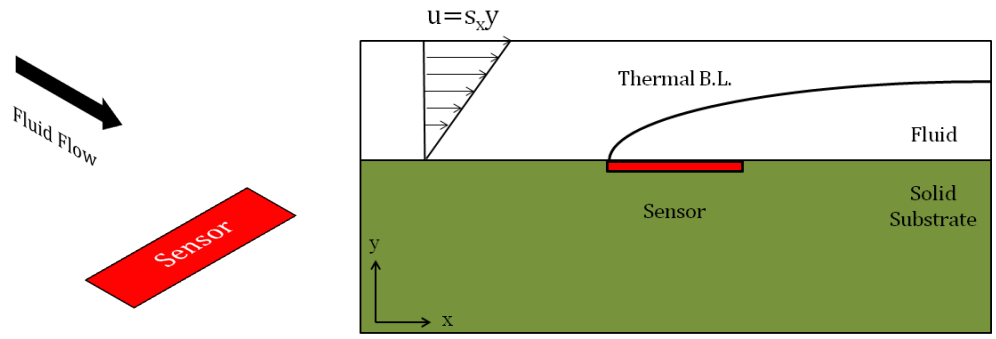

(a) (b)

Figure 2.2: A schematic of the single-element hot-film sensor and two-dimensional representation of its domain. x and y denote the streamwise and wall-normal directions. The spanwise direction is normal to this plane.

single film flush-mounted on a solid substrate. The material used for the film is a high TCR material such as nickel and the substrate is made of a low conductivity material such as glass. The sensor is connected to a CTA circuit, as described before, and its temperature is kept at a constant value higher than the fluid temperature. Because of the temperature difference, heat goes from the sensor to the fluid. As a result, a thermal boundary layer starts growing from the leading edge of the sensor. Based on classical hot-film theory, the rate of heat transfer from the sensor to the fluid Q_F is related to the WSS τ_w as

$$\tau_w \sim Q_F^3. \tag{2.2}$$

This expression has been derived by many researchers [24, 25, 26]. The underlying assumptions for the use of this relation for turbulent WSS measurement are that the thermal boundary layer is contained within the viscous sublayer, streamwise and spanwise diffusion are negligible and that no heat conduction to the substrate occurs. We will discuss assumptions in greater detail in Chapter 3.

Single-element hot-film sensors suffer from several deficiencies. The assumptions made to get the calibration relation, impose limits on the length of the sensor, and on the range of shear rates and frequencies in which they can be used in turbulent flows. Some of these limits, as will be shown in the next chapter, are in conflict with each other. Accuracy for time-resolved measurements introduces additional limits. The finite inertia of the thermal boundary layer limits the response of the sensor at high

frequencies, causing amplitude attenuation at the high frequency end of spectrum.

The most significant source of error in conventional hot-film sensors, is heat conduction to the substrate. The heat transport to the substrate, eventually goes to the fluid from upstream and downstream of the sensor. This has been shown schematically in Figure 2.3. With this additional, unwanted, heat going out of the sensor, the total rate of heat generated in the sensor is $Q = Q_F + Q_S$ instead of being $Q = Q_F$ as desired. The rate of heat conduction to the substrate Q_S can be much larger than the heat going directly to the fluid Q_F, especially for fluids with a low thermal conductivity, such as air. Thermal conductivity of a substrate material like glass is about 25 times higher than that of air. In this case the heat transfer through the substrate becomes tens of times higher than heat transfer to the fluid [27].

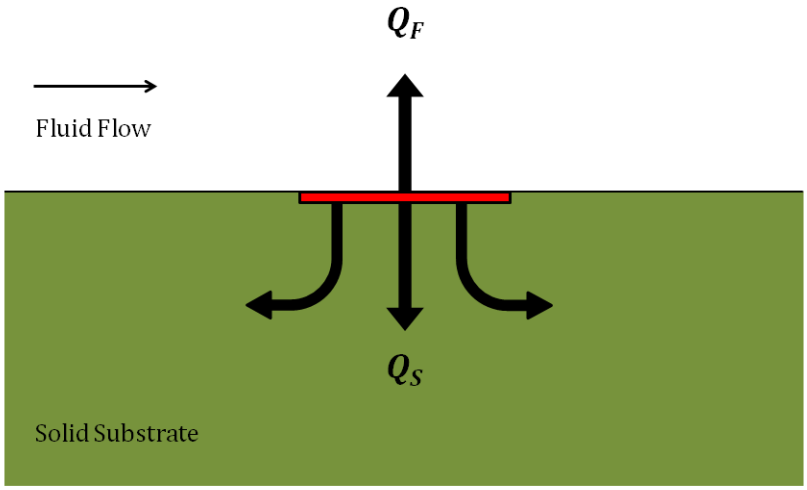

Figure 2.3: Single-element(SE) sensor.

Heat transfer through the substrate has several undesirable effects. Heat transfer from the sensor to the fluid happens over an area much larger than the physical area of the sensor. Thus the effective size of the sensor is larger than the actual size of the sensor and its spatial resolution is reduced. As we will see, the amount of heat transfer to the substrate and the effective sensor size both change with shear rate and frequency. Thus we will have a sensor with variable, flow-dependent spatial resolution, which is unacceptable. Moreover, if a high percentage of the total heat transfer is due to the heat transfer through the substrate, the sensitivity of the sensor to the changes in the WSS weakens [23].

The frequency response of the sensor is also affected by the frequency and shear

dependent heat transfer through the substrate [23, 13]. The time-constant of the substrate is typically much larger than the sensor itself, and its frequency limit is much lower than the limit imposed by the heat transfer in the fluid [27]. Tardu *et al.* (2005) investigated the effects of axial diffusion and substrate conduction on the frequency response of hot-film sensors. They found that when conductivity of the substrate is much higher than that of the fluid, heat transfer through the substrate becomes dominant. As a result, in the case of air as the fluid and glass as the solid, the frequency response of the sensor drops at very low frequencies because of the substrate heat conduction [28]. Because the dynamic behaviour of the substrate and the fluid are different, and depend on various flow field parameters, a static calibration cannot be used for turbulent flows [29]. Using a typical static calibration (based on laminar flow) results in under-prediction of the r.m.s turbulent shear-stress levels when the substrate heat conduction is significant [30].

Many researchers have realised and tried to eliminate the problems introduced by the substrate conduction. One of the methods used, aimed at reducing the effective conductivity for substrate heat transfer path, is separating the sensor from the substrate by a vacuum pocket, and placing the sensor on a diaphragm. Q. Lin *et al.* (2004) proposed and studied a novel MEMS thermal sensor, with a single hot-film placed on a silicon nitride or Parylene diaphragm [19]. An air/vacuum pocket beneath the diaphragm separated their sensor from the substrate. Yamagami *et al.* (2005) [11] and Liu *et al.* (1999) [31] also used a diaphragm to suspend the sensor from the substrate. However, heat conduction from the probe to the diaphragm on which they are deposited can cause spatial averaging and phase distortion. Although Liu *et al.* shows that the new design has higher sensitivity and better frequency response from a square wave test, the effects of heat transfer through the diaphragm are not characterized and studied. Ruedi *et al.* (2004) used a hot-film placed on a $1.2\mu m$ thick silicon-nitride diaphragm with a $2\mu m$ deep vacuum cavity to reduce substrate conduction. They compared the results of their measurements in air to wall-wire measurements and found that frequency response of the suspended hot-films dropped faster than hot-wires. They argued that this may be a result of unsteady heat transfer effects in the membrane/substrate. Huang *et al.* (1995) deposited a poly-silicon strip on the top of a thin silicon nitride film. By using a sacrificial-layer technique, a cavity (vacuum chamber) was placed between the silicon nitride film and silicon substrate. They found that the vacuum cavity improved the sensor sensitivity but resulted in a slower frequency response [32]. It appears that no results have been reported on heat

loss to the diaphragm and its effects on spatial resolution and signal quality of this type of sensor.

To avoid substrate conduction difficulties of hot-films, hot-wires located very close to the wall are also used to find the value of wall shear stress by measuring velocity and assuming a linear velocity profile [33, 34]. Near-wall hot-wires are suitable for low Reynolds numbers, since they should be located in the viscous sublayer. At high Reynolds numbers, however, the viscous sublayer becomes very thin, requiring the hot-wires to be place very close to the wall, and subsequently aerodynamic interference from the wall and heat transfer to the wall introduce errors [34]. Therefore, corrections are required for prongs and wall interference and heat losses . Another method used to reduce substrate heat conduction effects is making a cavity underneath a flush-mounted hot-wire [35, 27].

Aoyagi *et al.* (1986) used a sensor made of two commercial probes glued back-to-back, one serving as the sensing device and the other as the guard-heater, located beneath the first probe [36]. They found that using this configuration, errors of using laminar calibration to measure mean wall shear stress in a turbulent flow were greatly reduced. Ajagu *et al.* (1982) used a near-wall hot-wire with a flush-mounted hot-film underneath serving as a guard-heater [29]. Their laminar calibration results show deviations from linearity at low shear rates, which they argue is due to natural convection. However, they do not consider possible effects of axial diffusion. Detailed study of frequency characteristics of this sensor are not reported.

2.3 Guard-Heated Sensor Design

From the above efforts and a number of other published reports, it seems likely that we cannot obtain accurate, time-resolved measurements with hot-film or hot-wire sensors, unless we eliminate the effects of the substrate conduction on the sensor signal. Most attempts appear to have been focused on decreasing the effective conductivity of the substrate, *i.e.* by using a cavity underneath the sensor, to reduce the substrate conduction. This may sound promising at first, but when doing measurements in a fluid with such a low thermal conductivity as air, not much can be done to lower the thermal conductivity ratio of the substrate to the fluid. Instead of abandoning hot-film thermal measurements, we propose a design to *block* any heat transfer from the sensor to the substrate. We will refer to this new sensor design as the *guard-heated* design.

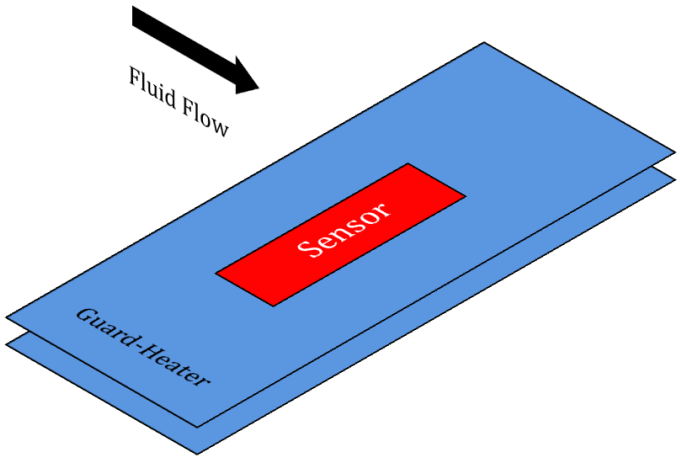

Figure 2.4: A schematic of the guard-heated sensor design.

Figure 2.4 shows a schematic of the guard-heated WSS sensor design. In comparison to the conventional single-element sensor of Figure 2.3, in the guard-heated design the sensor is surrounded by an *in-plane* guard-heater. We can also add another guard-heater plane underneath this setup. Thus we can have a *single-plane guard-heated* sensor, consisting of a sensor with an in-plane guard-heater, or a *two-plane guard-heated* sensor by adding a second guard-heater to the single-plane design.

2.3.1 The Idea Behind Guard-Heating

How might guard-heating help us with WSS measurements? The substrate heat transfer consists solely of heat diffusion into the solid, governed by the thermal diffusivity of the substrate material and the temperature gradient at the sensor film interface. Most attempts to eliminate the substrate heat conduction have been focused on reducing the effective thermal diffusivity of the substrate. Some researchers have used a vacuum pocket underneath the sensor, allowing it to be mounted on a diaphragm. However, the diaphragm itself, although thin, has high conductivity compared to air as well as low thermal inertia and thus cannot eliminate the effects of the indirect heat transfer. Other researchers have used hot-wires with a cavity underneath to reduce the indirect heat transfer. This way the conductivity ratio of the fluid and the new substrate (consisting of a cavity and the substrate material) is still 1 at best.

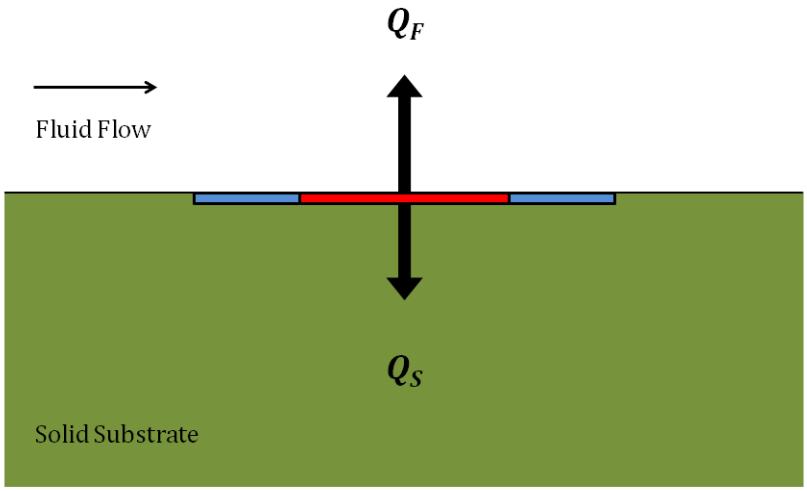

(a) Single-Plane (GH1P)

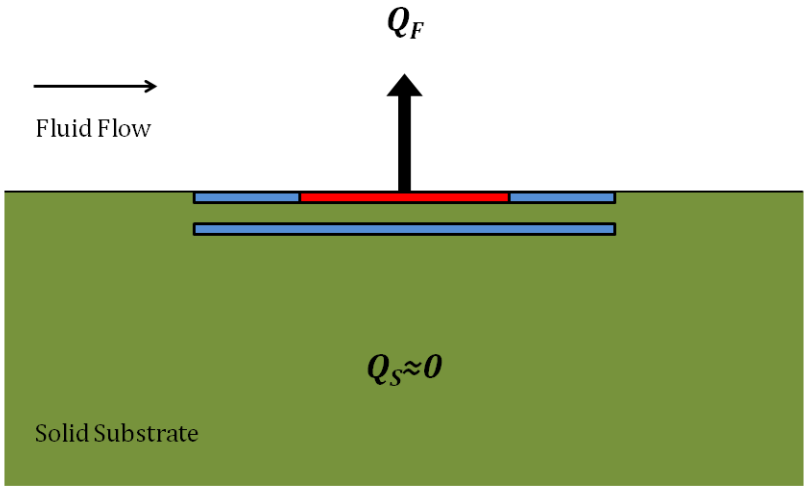

(b) Two-Plane (GH2P)

Figure 2.5: Guard-heated sensors.

The novelty of a guard-heated microsensor is in seeking to eliminate substrate heat conduction by eliminating the temperature gradient in the substrate, instead of lowering the effective conductivity of the substrate. If we surround the sensor by a film kept at the same temperature (by a separate CTA circuit) as the sensor itself, then the temperature gradient in the substrate at the edges of the sensor is forced to be zero. This film is the in-plane guard heater, which should be expected to reduce heat transfer from sensor edges and substrate. It will also eliminate the streamwise and spanwise temperature gradients within the fluid, which we will see, reduces one

of the calibration errors. Figure 2.5-a shows a schematic of the single-plane guard-heated design. By reducing the axial temperature gradient, the amount of heat going into the substrate decreases. However, because a wall-normal temperature gradient still exists, some heat will diffuse into the substrate. If we use another guard-heater beneath the sensor (Figure 2.5-b), the wall-normal gradient may be reduced further, allowing for the possibility of blocking any heat from diffusing into the substrate.

The guard-heaters block heat transfer from the sensor to the substrate. However, the substrate still picks up heat from the guard-heaters. In fact, the substrate will pick up more heat since the guard-heaters are larger than the sensor itself. So how does guard-heating help us, if at all, if it heats the substrate more than before? The answer to this question is crucial and lies in the fact that the guard-heaters are electrically isolated from the sensor and are connected to a separate CTA bridge circuit. Only the signal coming from the sensor is used for measurements. With no heat transfer from the sensor to the substrate occurring, the sensor signal is only dependent on the rate of heat transfer from the sensor to the fluid. Thus the sensor does not account for heat conduction in the substrate. Both guard heating elements may be connected in series to be operated as a single resistance, using just one additional CTA bridge circuit.

2.3.2 Fabrication of the Guard-Heated Sensors

In terms of the fabrication process, a single-point, single-component guard-heated sensor needs one additional anemometer circuit in comparison to a single-element sensor to maintain the guard temperature. However, multiple-element probes can encompass several inner sensors for two-component or multi-point measurements, using one guard-heater.

Four different guard-heated sensors in a plane have been fabricated in various sizes by R.B. Bhiladvala (2009) [37]. He created sensors of four sizes: $12 \times 60\mu m$, $24 \times 96\mu m$, $72 \times 288\mu m$, and $250 \times 1000\mu m$, ranging from 0.004 to 1.3 times the area of the smallest commercial single-element WSS sensor, made by DANTEC (probe model:55R46). In all these sensors, the sensing element is placed in the middle of a guard heater three times its streamwise length. As a result of work in this thesis, a suitable size can be selected depending on the body geometry and flow parameters. In addition, signal-to-noise ratio becomes crucial when the sensor is small. Thus, use of a smaller, microfabricated sensor which improves spatial resolution must also

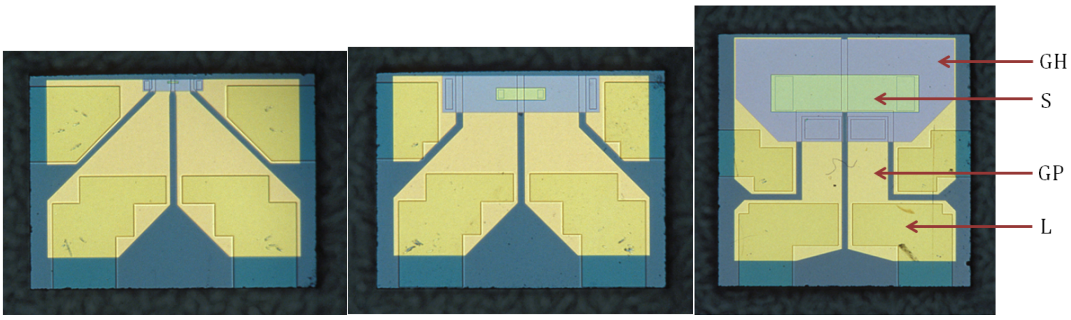

(a) (b) (c)

Figure 2.6: Guard-heated sensor chips fabricated in different sizes. GH: Guard-heater, S: Sensor, GP: Gold pad, L: Lead attachment area.

provide adequate signal-to-noise ratio.

Six levels of photolithography patterning and deposition/etching were required using a silicon wafer with a silicon oxide surface layer, to make the sensor chip. A brief outline of the fabrication process is provided below to establish that the proposed sensor design can be fabricated.

1. A thin dielectric layer of silicon oxide was grown on a silicon wafer base.

2. The first layer of photlithographic patterning and gold-film evaporation, was used to create four gold bonding pad, to enable lead from the CTA circuit to provide current for the thin film heating elements. Each pad was then attached to one of the two ends of the rectangular-shaped sensor and guard heater elements, seen in Figure 2.6.

3. This gold bonding pad layer was covered by depositing a layer of silicon dioxide to electrically isolate it from the other layers.

4. Since the dielectric layer covers the whole area of the gold pads, two holes were etched through the silicon dioxide using photolithographic patterning. The required electric current to provide a constant temperature in the guard heater was supported by these holes.

5. The guard heater was created by evaporating a layer of nickel, which makes contact to the guard-heater's bonding pads, patterned in step 4. The required electric current to provide a constant temperature in the guard-heater was supported by these contacts.

6. Another dielectric layer was deposited, to electrically isolate the guard-heater.

7. Steps 4-6 were then repeated to pattern and electrically insulate the sensing element.

8. At the end, to connect the gold bonding pads to the leads, some connecting areas were patterned and insulating oxide was removed by etching.

The chip was located in a ceramic holder, over a central air cavity to reduce chip heat loss to the mounting assembly. Four connecting leads were made by thin film evaporation, to prevent wires from intruding into the flow.

Chapter 3

Analysis of the Conjugate Heat Transfer Process

The goal of this thesis is to examine the viability of guard-heated WSS sensors. In the previous chapter, we mentioned some of the most severe errors and limitations associated with conventional single-element sensors, which, judging by the absence of publications, are no longer used for WSS fluctuation measurements by the turbulence research community. To establish the viability of guard-heated sensors, we will first quantify the limitations in the use of the conventional single-element hot-film sensors, and see how we might expect to reduce the errors with the guard-heated design proposed. In this chapter, we present an analytical framework with non-dimensionalized governing equations for the conjugate fluid-solid heat transfer problem, which shows that conflicting requirements allow virtually no window of operation free of large errors for the conventional single-element sensor. We will use our framework to see how guard-heating disables these conflicts and allows ranges of operation free of systemic errors. Our goal is to answer the following questions by the end of this chapter:

1. What assumptions are made in the derivation of the calibration relation used? Are they valid?

2. What factors constrain the choice of sensor size? In particular, if nano-fabrication techniques allow the sensor to be made small enough to resolve the smallest fluctuations in WSS, could we make do with a single sensor?

3. What is the range of frequencies that the sensor can measure?

4. What systemic errors can we anticipate in the phase and spectra of the WSS fluctuations measured? To what extent does guard heating reduce these errors? These questions are of concern for the construction of models for near-wall turbulence.

5. Will sensor sensitivity and signal-to-noise ratio be adequate?

6. What other design considerations must be taken into account for a thermal WSS sensor?

3.1 Governing Equations

The wall shear stress is measured through its relation to the heat transfer from a heated film to a fluid flow. We will use the advection-diffusion equation in the fluid flow and heat conduction in the solid substrate. The condition of heat flux continuity at the interface provides the coupling between these equations for this conjugate heat transfer problem. Figure 3.1 shows a schematic of the problem with fluid and solid domains.

The governing equation for heat transfer in the fluid is the unsteady energy equation for an incompressible, constant property flow

$$\frac{\partial T}{\partial t} + u\frac{\partial T}{\partial x} + v\frac{\partial T}{\partial y} + w\frac{\partial T}{\partial z} = \alpha_f \left(\frac{\partial^2 T}{\partial x^2} + \frac{\partial^2 T}{\partial y^2} + \frac{\partial^2 T}{\partial z^2} \right), \tag{3.1}$$

where $T(x, y, z, t)$ is the temperature field, u, v and w are axial, wall-normal and spanwise components of the velocity field, respectively, and α_f is the thermal diffusivity of the fluid. Zero temperature gradient boundary condition is imposed at all unmarked external boundaries in Figure 3.1. Hot-film sensors are made with high width-to-length ratio to make heat transfer to the fluid less sensitive to spanwise fluctuations w. Moreover, we will later work under the imposed requirement that the thermal boundary layer is thin enough to be contained within a region where v fluctuations are small relative to u fluctuations (*i.e.* viscous sublayer). This requirement will impose a restraint on sensor length, to be consistent with the assumption we make here, which is that turbulent transport by v and w are negligible. With the no-slip condition, and for small distances from the wall, it is reasonable to follow the common practive of assuming that the velocity profile is linear at any instant. As a result, a Couette flow with a harmonic shear rate proves to be an adequate model for

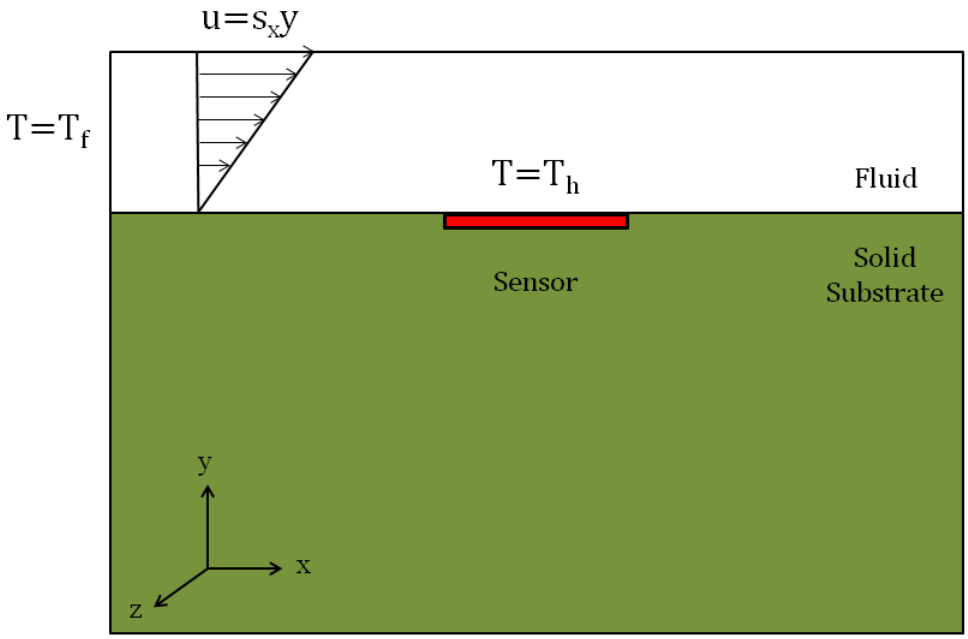

Figure 3.1: Geometry of the conjugate heat transfer problem. x, y and z are the axial (streamwise), wall-normal and spanwise directions respectively. At the domain boundaries where no temperature boundary condition is specified, zero temperature gradient boundary condition is imposed.

studying sensor response. For the streamwise velocity u we can write

$$u = s_x y, \tag{3.2}$$

where $s_x = \overline{s}_x(1 + \cos(\omega t))$ is the imposed harmonic shear rate with the frequency of ω. We can now rewrite Equation 3.1 as

$$\frac{\partial T}{\partial t} + s_x y \frac{\partial T}{\partial x} = \alpha_f \left(\frac{\partial^2 T}{\partial x^2} + \frac{\partial^2 T}{\partial y^2} + \frac{\partial^2 T}{\partial z^2} \right), \tag{3.3}$$

In the solid substrate where heat conduction occurs, the energy equation is

$$\frac{\partial T}{\partial t} = \alpha_s \left(\frac{\partial^2 T}{\partial x^2} + \frac{\partial^2 T}{\partial y^2} + \frac{\partial^2 T}{\partial z^2} \right), \tag{3.4}$$

where α_s is the thermal diffusivity of the substrate material.

The interface between the fluid and solid regions needs special treatment. We can

couple the energy equations by using continuity of heat flux, which dictates that the amount of heat flux coming from the solid region should equal the amount of heat flux going to the fluid region. We can write this as

$$k_s \left(\frac{\partial T}{\partial y}\right)_s = k_f \left(\frac{\partial T}{\partial y}\right)_f, \tag{3.5}$$

where k_s and k_f are thermal conductivities of the substrate and the fluid, respectively.

3.1.1 Non-Dimensional Equations

We will now non-dimensionalize the energy equations and the interface condition obtained in the previous section. The rest of our analysis in this chapter will be based on the order-of-magnitude analysis of the dimensionless terms that appear in the non-dimensionalized equations.

To non-dimensionalize the fluid energy equation, we will use the frequency of the applied shear ω for time t and hot-film length L and width W for axial and spanwise coordinates x and z. For the wall-normal coordinate y, we will use thermal boundary layer thickness δ_t. Since shear rate fluctuation magnitude as well as frequency are both $\sim t^{-1}$, with the lack of any other physical lengths that can be taken as a characteristic length, we choose L for the axial coordinate. For the solid substrate, we will again use ω for time, and for the axial, wall-normal and spanwise coordinates x, y and z, we use substrate "temperature penetration length" L_s. Two things should be noted here. It should be noted that we do not know anything about the temperature penetration length L_s in the solid substrate yet. We define dimensionless temperature as

$$\theta = \frac{T - T_f}{T_h - T_f}, \tag{3.6}$$

where T_h and T_f are the hot-film and the fluid temperature, respectively. The dimensionless variables for the energy equation in the fluid are chosen as

$$x' = \frac{x}{L}, y' = \frac{y}{\delta_t}, z' = \frac{z}{W}, \theta = \frac{T - T_f}{T_h - T_f}. \tag{3.7}$$

The dimensionless variables for the energy equation in the solid substrate are

$$x' = \frac{x}{L_s}, y' = \frac{y}{L_s}, z' = \frac{z}{L_s}, \theta = \frac{T - T_f}{T_h - T_f}. \tag{3.8}$$

For the interface condition we use the variables

$$y_s' = \frac{y_s}{L_s}, y_f' = \frac{y_f}{\delta_t}, \theta = \frac{T - T_f}{T_h - T_f}. \tag{3.9}$$

Following standard practice, for convenience we will drop the primes ($'$) from now. Using these dimensionless variables we will rewrite the energy equations and the interface condition. We begin with the fluid energy equation. It can be written as

$$\omega \frac{\partial \theta}{\partial t} + s_x y \left(\frac{1}{L}\right) \frac{\partial \theta}{\partial x} = \alpha_f \left[\left(\frac{1}{L^2}\right) \frac{\partial^2 \theta}{\partial x^2} + \left(\frac{1}{\delta_t^2}\right) \frac{\partial^2 \theta}{\partial y^2} + \left(\frac{1}{W^2}\right) \frac{\partial^2 \theta}{\partial z^2} \right]. \tag{3.10}$$

By multiplying this equation by δ_t^2/α_f and some reordering, we can rewrite it as

$$\frac{\omega L^2}{\alpha_f} \left(\frac{\delta_t}{L}\right)^2 \frac{\partial \theta}{\partial t} + \frac{s_x L^2}{\alpha_f} \left(\frac{\delta_t}{L}\right)^3 y \frac{\partial \theta}{\partial x} = \left(\frac{\delta_t}{L}\right)^2 \frac{\partial^2 \theta}{\partial x^2} + \frac{\partial^2 \theta}{\partial y^2} + \left(\frac{L}{W}\right)^2 \left(\frac{\delta_t}{L}\right)^2 \frac{\partial^2 \theta}{\partial z^2}. \tag{3.11}$$

We can see that new dimensionless terms appear as $\omega L^2/\alpha_f$, $s_x L^2/\alpha_f$ and δ_t/L, which are crucial in our analysis and we will get back to them later. Similarly, we may rewrite Equation 3.4 as

$$\frac{\omega L^2}{\alpha_f} \left(\frac{L_s}{L}\right)^2 \left(\frac{\alpha_f}{\alpha_s}\right) \frac{\partial \theta}{\partial t} = \frac{\partial^2 \theta}{\partial x^2} + \frac{\partial^2 \theta}{\partial y^2} + \frac{\partial^2 \theta}{\partial z^2}. \tag{3.12}$$

We have written Equation 3.12 such that the dimensionless term $\omega L^2/\alpha_f$ appears again, to be consistent with Equation 3.11. The non-dimentionalized form of the interface equation may be written as

$$\frac{k_s}{L_s} \left(\frac{\partial \theta}{\partial y}\right)_s = \frac{k_f}{L} \left(\frac{\partial \theta}{\partial y}\right)_f. \tag{3.13}$$

Again, to be consistent with the Equation 3.11 and Equation 3.12 regarding the dimensionless terms, we will rewrite this equation as

$$\frac{k_s}{k_f} \left(\frac{L}{L_s}\right) \left(\frac{\delta_t}{L}\right) \left(\frac{\partial \theta}{\partial y}\right)_s = \left(\frac{\partial \theta}{\partial y}\right)_f. \tag{3.14}$$

We now have a set of non-dimensional equations with several dimensionless terms $\omega L^2/\alpha_f$, $s_x L^2/\alpha_f$, δ_t/L and L/L_s. The other two terms, L/W and k_s/k_f depend on the geometry of the sensor and the fluid and substrate materials. We define a

dimensionless frequency as

$$\omega^* = \frac{\omega L^2}{\alpha_f}, \tag{3.15}$$

and an instantaneous Peclet number, which is a dimensionless measure of the shear strength, as

$$Pe = \frac{s_x L^2}{\alpha_f}. \tag{3.16}$$

From now on, we will use these two dimensionless quantities whenever we talk about frequency and shear strength. We can rewrite our governing equations as

$$\omega^* \left(\frac{\delta_t}{L}\right)^2 \frac{\partial \theta}{\partial t} + Pe \left(\frac{\delta_t}{L}\right)^3 y \frac{\partial \theta}{\partial x} = \left(\frac{\delta_t}{L}\right)^2 \frac{\partial^2 \theta}{\partial x^2} + \frac{\partial^2 \theta}{\partial y^2} + \left(\frac{L}{W}\right)^2 \left(\frac{\delta_t}{L}\right)^2 \frac{\partial^2 \theta}{\partial z^2}, \tag{3.17}$$

and

$$\omega^* \left(\frac{L_s}{L}\right)^2 \left(\frac{\alpha_f}{\alpha_s}\right) \frac{\partial \theta}{\partial t} = \frac{\partial^2 \theta}{\partial x^2} + \frac{\partial^2 \theta}{\partial y^2} + \frac{\partial^2 \theta}{\partial z^2}. \tag{3.18}$$

We will thoroughly investigate these terms and see what they mean for the performance of the hot-film sensors in section 3.2. In the next section, we briefly consider the basis and assumptions for the calibration relation.

3.1.2 The Leveque Solution

The functional form of calibration equation used for hot-film WSS sensors is based on the Leveque solution [25], which is important to understand for this work, as several features of our guard-heated design are motivated by the need to reduce deviations from this calibration relation. Let us examine the fluid energy equation (Equation 3.3) again. If transport due to all but axial convection and wall-normal diffusion could be neglected, the energy equation for the fluid reduces to

$$\frac{\partial T}{\partial t} + s_x y \frac{\partial T}{\partial x} = \alpha_f \frac{\partial^2 T}{\partial y^2}, \tag{3.19}$$

Now, if we only consider slow fluctuations, we can neglect the time derivative term. We will now have a quasi-steady energy equation, since s_x is time-dependent but there are no time derivatives. The simplified, quasi-steady energy equation is

$$s_x y \frac{\partial T}{\partial x} = \alpha_f \frac{\partial^2 T}{\partial y^2}. \tag{3.20}$$

An analytical solution exists for the above equation for a semi-infinite hot-film lying on perfectly insulating surface, which is called the Leveque's solution. The solution is

$$Nu' \equiv \frac{Q'}{k_f(T_h - T_f)} = 0.807 Pe^{\frac{1}{3}}, \tag{3.21}$$

where Q is the total heat transfer from the hot-film to the fluid and *Nusselt* number Nu is dimensionless heat transfer rate. The prime sign ($'$) indicates the quantities are per unit depth. We will drop this sign and use Q and Nu from now on for dimensional and dimensionless heat transfer rates per unit depth. The complete derivation of the Leveque solution is available in Appendix A.

There are several assumptions made in the Leveque solution, simplifying Equation 3.3 to Equation 3.20:

1. The hot-film is semi-infinite; meaning there is no trailing edge for the film.
2. The hot-film lies on an insulating surface, hence, no heat transfer from the substrate to the fluid occurs.
3. Axial and spanwise heat conduction in the fluid is negligible at all Peclet numbers,
4. Fluctuations are slow enough that the time it takes for them to pass over the hot-film is greater than the time needed for heat to diffuse across the thermal boundary layer thickness.

We can assess each of these assumptions through numerical or analytical study, except for Assumption 1, which represents a geometrically unphysical condition.

As stated before, Equation 3.21 is the calibration relation used for all hot-film WSS sensors, hence, all numerical results in Chapter 4 will be compared to the Leveque solution to see how much each sensor deviates from what Equation 3.21 predicts.

3.2 Analysis

We now return to the non-dimensional governing equations for analysis. Balancing the axial convection term with the wall-normal diffusion term in Equation 3.17, implies that

$$\frac{\delta_t}{L} \approx Pe^{-\frac{1}{3}}. \tag{3.22}$$

Hence, several terms in the fluid energy equation have Pe dependencies. We can rewrite Equation 3.17 as

$$\omega^* Pe^{-\frac{2}{3}} \frac{\partial \theta}{\partial t} + y \frac{\partial \theta}{\partial x} = Pe^{-\frac{2}{3}} \frac{\partial^2 \theta}{\partial x^2} + \frac{\partial^2 \theta}{\partial y^2} + Pe^{-\frac{2}{3}} \left(\frac{L}{W} \right)^2 \frac{\partial^2 \theta}{\partial z^2}. \tag{3.23}$$

We can now revisit the assumptions made for the Leveque solution. Both axial and spanwise diffusion term have Pe dependencies. Therefore, assumptions 3 in section 3.1.2 is only valid for high Pe values. Spanwise heat conduction also depends on the geometry of the sensor; choosing a higher width-to-length ratio, decreases the spanwise diffusion. We could have predicted both of these statements even without looking at Equation 3.23. Higher Pe means higher shear rate, or higher streamwise fluid velocity. At higher velocities, convection dominates diffusion in the axial direction and heat cannot diffuse to the upstream of the hot-film. The same claim can be made in the spanwise direction.

The unsteady term in Equation 3.23 has both Pe and ω^* dependencies. If $\omega^* Pe^{-\frac{2}{3}}$ is $\mathcal{O}(1)$, then the time needed for the fluctuations to pass through the sensor is comparable to the time needed for heat to diffuse across the thermal boundary layer thickness. Thus, the thermal inertia of the boundary layer becomes important and the sensor signal suffers from phase lag and amplitude attenuation. If $\omega^* Pe^{-\frac{2}{3}}$ becomes very large, meaning $\omega^* Pe^{-\frac{2}{3}} \gg 1$, then the fluctuations are too fast for the sensor to be sensed. In this range, the fluctuations are so fast that there is not enough time for heat transfer in the fluid to *react* to the changes in the velocity field, the sensor does not sense the fluctuations at all, and no change in the signal will be reported by the sensor. This results in truncation of the spectrum at high frequencies. For the energy equation in the fluid to be quasi-steady, or the assumption 4 in section 3.1.2 to be true, $\omega^* Pe^{-\frac{2}{3}}$ must be much less than one, or $\omega^* Pe^{-\frac{2}{3}} \ll 1$.

For any practical material choice for the substrate, heat will diffuse into it. This heat will go to the fluid eventually, mostly upstream of the sensor. Hence, assumption 2 of section 3.1.2 will not be valid. We will analyze the solid energy equation and the interface condition to get more insight on the substrate conduction.

Let us look back at Equation 3.18 for the solid and Equation 3.14 for the interface. There is no immediately obvious Pe dependency in Equation 3.18. We stated earlier that we do not know anything about the temperature penetration length L_s yet. We will now try to reasonably relate L_s/L to quantities we are already familiar with. We wrote Equation 3.14 such that δ_t/L and L_s/L would appear. We already know that

δ_t/L is $\mathcal{O}(Pe^{-\frac{1}{3}})$. We can now rewrite the interface condition as

$$\frac{k_s}{k_f}\left(\frac{L}{L_s}\right)Pe^{-\frac{1}{3}}\left(\frac{\partial\theta}{\partial y}\right)_s = \left(\frac{\partial\theta}{\partial y}\right)_f. \tag{3.24}$$

By balancing the left and right hand side terms, which are wall-normal temperature gradients in the solid and fluid on the interface, we will get

$$\frac{L_s}{L} =\approx \frac{k_s}{k_f}Pe^{-\frac{1}{3}}. \tag{3.25}$$

We can now replace L_s/L in the solid energy equation by $(k_s/k_f)Pe^{-\frac{1}{3}}$ and get

$$\omega^* Pe^{-\frac{2}{3}}\left(\frac{\alpha_f}{\alpha_s}\right)\left(\frac{k_s}{k_f}\right)^2\frac{\partial\theta}{\partial t} = \frac{\partial^2\theta}{\partial x^2}+\frac{\partial^2\theta}{\partial y^2}+\frac{\partial^2\theta}{\partial z^2}. \tag{3.26}$$

Note the $\omega^* Pe^{-\frac{2}{3}}$ term of the fluid energy equation appears here again. We have succeeded in replacing the unknown term we had with familiar ones, $\omega^* Pe^{-\frac{2}{3}}$ and $(k_s/k_f)^2(\alpha_f/\alpha_s)$. In fact, the latter term is only a function of the thermal conductivity and the thermal diffusivity of the fluid and the substrate material. For convenience, we will define a new parameter, K, equal to this term

$$K = \left(\frac{k_f}{k_s}\right)^2\left(\frac{\alpha_s}{\alpha_f}\right). \tag{3.27}$$

We can rewrite Equation 3.26 as

$$\omega^* Pe^{-\frac{2}{3}}\left(\frac{1}{K}\right)\frac{\partial\theta}{\partial t} = \frac{\partial^2\theta}{\partial x^2}+\frac{\partial^2\theta}{\partial y^2}+\frac{\partial^2\theta}{\partial z^2}. \tag{3.28}$$

We can do an analysis for frequency, analogous to what we did for the fluid energy equation. If $\omega^* Pe^{-\frac{2}{3}} \gg K$, the fluctuations are too fast for heat transfer through the substrate. If $\omega^* Pe^{-\frac{2}{3}} \ll K$, the fluctuations are slow enough for the substrate to respond to them instantaneously and without any phase lag and the amplitude of the fluctuations of the substrate heat transfer rate will be equal to that of the quasi-steady case. If $\omega^* Pe^{-\frac{2}{3}}$ is anywhere between these two ranges, *i.e.* $\omega^* Pe^{-\frac{2}{3}} \approx K$, then the substrate heat conduction will react to the fluctuations with phase lag and amplitude smaller than the quasi-steady amplitude. This causes phase distortion in the spectrum if a considerable portion of the signal is due to the substrate conduction. We will look

more closely at the frequency response of the sensor in Section 3.4.1 of this chapter, after we have considered the opposing constraints on sensor length selection.

3.3 Sensor Length Considerations

We can fabricate WSS sensors in different sizes. Commercial WSS hot-film sizes are between a few hundred microns to a few millimetres. New micro-fabrication techniques allow us to build sensors as small as a few microns. In this section, we will try to find and quantify the limitations on the sensor size, if any, and see if we can get eliminate any of these limitations, using guard-heaters.

3.3.1 Spatial Averaging

A loss of resolution due to spatial averaging occurs whenever the size of the sensor is larger than the length scale of a given fluctuation. Spatial averaging can be a significant source of error, since all fluctuations with length scales smaller than the dimension of the sensor will be averaged, and hence, will be measured incorrectly as low intensity fluctuations. As a result, we will see spectral attenuation or truncation of smaller length scales. To avoid spatial averaging, the dimensions of the sensor must be as small as the smallest length scales in the flow, which decrease with increasing Reynolds number. Thus, avoiding spatial averaging requires using smaller sensors in flows with higher Reynolds numbers.

A common way to scale lengths in flows with different Reynolds numbers is to use the viscous length scale ν/u_τ, where ν is the kinematic viscosity of the fluid and u_τ is friction velocity defined as

$$u_\tau = \sqrt{\frac{\overline{\tau}_w}{\rho}} = \sqrt{\frac{\mu \overline{s}_x}{\rho}} = \sqrt{\nu \overline{s}_x}, \tag{3.29}$$

with $\overline{\tau}_w$ being the averaged wall shear stress. In a given flow geometry, the viscous length scale, or wall unit, decreases with increasing Reynolds number. Hence, a fixed physical length is larger in wall units for a flow with higher Reynolds number. We can scale the length and width of a sensor with wall units

$$L^+ = \frac{L u_\tau}{\nu}, W^+ = \frac{W u_\tau}{\nu}. \tag{3.30}$$

We will use Mitchell & Hanratty [18] criterion for pipe flows to avoid spatial averaging which states $W^+ < 8$. This criterion is based on multi-point measurements with electrochemical sensing. If we choose a width-to-length ratio of 4 to help reduce the spanwise heat conduction, as mentioned earlier in this chapter, this would yield the condition the for sensor length,

$$L^+ < 2. \tag{3.31}$$

We will use Equation 3.31 from now on as a criterion for avoiding spatial averaging, which requires the length to be smaller than $2\nu/u_\tau$.

3.3.2 Thermal Boundary Layer Thickness

One of the main assumptions made to get the calibration equation of hot-film sensors is that thermal boundary layer is contained within the viscous sublayer, therefore, the velocity profile can be assumed to be linear. Thus, the thickness of both the thermal boundary layer and the viscous sublayer must be checked. If δ_ν is the thickness of the viscous sublayer, then $\delta_t < \delta_\nu$ should be true at all times. We know from our earlier analysis that δ_t/L is $\approx Pe^{-1/3}$. We will use the following relation for δ_t [38]

$$\frac{\delta_t}{L} = \frac{1}{Nu}. \tag{3.32}$$

If we use the relation of Equation 3.21 we get

$$\frac{\delta_t}{L} = \frac{1}{0.807} Pe^{-\frac{1}{3}}. \tag{3.33}$$

In the viscous sublayer $y^+ = u^+$ and its boundary is at $y^+ = 5$. y^+ is the distance from wall in wall units and u^+ is axial velocity normalized by friction velocity. Thus, the thickness of viscous sublayer in wall units is equal to 5

$$\delta_\nu = \frac{5\nu}{u_\tau}. \tag{3.34}$$

Hence, using Equation 3.34, for the thermal boundary layer to be contained within the viscous sublayer we must have

$$\frac{1}{0.807} LPe^{-\frac{1}{3}} < \frac{5\nu}{u_\tau}. \tag{3.35}$$

Using the definitions of Pe and u_τ we can write

$$\frac{1}{0.807} L \frac{\alpha_f^{1/3}}{\overline{s}_x^{1/3} L^{2/3}} < 5\sqrt{\frac{\nu}{\overline{s}_x}}. \tag{3.36}$$

By raising both sides to the power of 3 and rearranging we get

$$L\sqrt{\frac{1}{\overline{s}_x \nu}} < 65.7 \frac{\nu}{\alpha_f}, \tag{3.37}$$

or simply

$$L^+ < 65.7 Pr. \tag{3.38}$$

Equation 3.38 shows that the assumption of thermal boundary layer being thinner than the viscous sublayer, imposes an upper limit on the size of the sensor. This limit depends on the properties of the flow and the shear strength. For air and water, the fluids of most frequent interest, Pr is 0.7 and 7 respectively, and Equation 3.31 is the more restrictive condition on sensor length.

3.3.3 Axial Diffusion

Another limit on the sensor length is imposed by the assumption of negligible axial diffusion in Equation (3.23), requiring $Pe \gg 1$ (large L for a given shear rate). To obtain a rough estimate, we take both x and y derivative terms to be 1 on the right hand side of Equation (3.23). A fractional error below 0.01 from axial conduction would then require $Pe^{-2/3} < 0.01$, or $Pe > 1000$. A more accurate solution by Ling [39] shows that the fractional error to the Leveque solution from axial conduction is given by $0.235 Pe^{-1/2}$, which yields, for fractional error below 0.01, the limiting condition

$$Pe > 500. \tag{3.39}$$

Since $Pe = L^{+2} Pr$ we can rewrite Equation 3.39 as

$$L^+ > 22.3 Pr^{-\frac{1}{2}}. \tag{3.40}$$

Equation 3.40 shows that the length of the sensor must be larger than a certain value, depending on the fluid properties and shear strength. Otherwise, the assumption of negligible axial diffusion is not correct. In physical terms, because of the

sudden change in temperature near the leading and trailing edges of the hot-film, the neglected terms become significant [9] and the heat transfer would be dominated by edge effects [28]. We observe here that reducing errors due to spatial averaging and fluid thermal boundary layer thickness both call for smaller sensor length L, but doing so could increase errors from the calibration due to axial heat diffusion in the fluid. We will see how guard-heating disables this and other conflicts, later in this chapter, after discussing the design requirements introduced in the following section.

3.4 Design Requirements

So far in this chapter, we have found a number of constraints relating shear strength, frequency and sensor length for the single element sensor design, by studying the governing equation. Several of these constraints are in conflict with each other. To choose the right design parameters for a sensor, one has to answer the following questions:

1. Are the fluctuations slow enough for the sensor to detect?
2. Does substrate heat conduction distort the spectrum of measured WSS fluctuations?
3. Is the sensor small enough to avoid spatial averaging?
4. Are axial and spanwise diffusion terms negligible?
5. Is the sensor signal strong enough?
6. Is natural convection negligible?

3.4.1 Frequency Response

Let us look back at the conditions we found for frequency. We want the sensor heat transfer to be responsive, with negligible phase lag, to any fluctuations in the fluid. This yields the following condition

$$\omega^* Pe^{-\frac{2}{3}} \ll 1. \tag{3.41}$$

However, things are more complicated for the substrate. For the substrate to be *unresponsive* to the fluctuations we should have

$$\omega^* Pe^{-\frac{2}{3}} \gg K, \tag{3.42}$$

and for the substrate to respond instantaneously to the fluctuations without any phase lag we should have

$$\omega^* Pe^{-\frac{2}{3}} \ll K. \tag{3.43}$$

We recall that the sensor signal depends on the heat transfer rate from the sensor to the fluid directly and to the solid substrate. From now on, we will refer to these two heat transfer rates as *direct* and *indirect*, respectively, having in mind that the heat going to the substrate goes to the fluid eventually, thus it goes from the sensor to the fluid *indirectly*.

Table 3.1: Frequency analysis of fluid and substrate heat transfers.

	$\omega^* Pe^{-\frac{2}{3}} \ll 1$	$\omega^* Pe^{-\frac{2}{3}} \gg 1$
$\omega^* Pe^{-\frac{2}{3}} \ll K$	Both fluid and substrate respond instantaneously.	Fluctuations are too fast for the fluid. Any change in signal is due to substrate.
$\omega^* Pe^{-\frac{2}{3}} \gg K$	Fluctuations are too fast for the substrate. Any change in signal is due to fluid.	Fluctuations are too fast for both fluid and substrate.

If both conditions of Equation 3.41 and 3.43 are met, then both substrate and fluid heat transfer rates change instantaneously. If so, we can use a static calibration curve for measurements. A static calibration curve can be obtained by calibrating in a laminar flow at fixed Peclet numbers and measuring the heat transfer at each value. If conditions of Equation 3.41 and 3.42 are met, meaning the fluid heat transfer changes instantaneously but the substrate heat transfer does not change at all, we cannot use the above-mentioned static calibration curve since it accounts for changes in both direct and indirect heat transfer rates with Pe. If condition of Equation 3.41 is met but neither of the conditions of Equation 3.42 and 3.43 are met, then the substrate will respond to the fluctuations with phase lag and hence introduces distortion in the signal. The complexities introduced by the substrate heat transfer in thermal WSS sensing now become more apparent.

Let us see what is the value of K for both water-glass and air-glass cases to get a better understanding of the requirements for frequency. Using these values, K_w and

Table 3.2: Thermal properties of water, air and glass.

Material	Thermal Conductivity, k $(W/m.K)$	Thermal Diffusivity, α $10^{-7}(m^2/s)$
Water	0.6	1.44
Air	0.024	196
Glass	1.38	8.34

K_a which are K for water and air, respectively, as fluid and glass as substrate will be $K_w \approx 1$ and $K_a \approx 10^{-5}$. If we look back at Table 3.1, we can see that for both fluid and substrate to respond instantaneously to any fluctuations, or for the quasi-steady assumption to be true in both fluid and substrate, we should have

$$\text{Water:} \quad \omega^* Pe^{-\frac{2}{3}} \ll 1, \tag{3.44}$$

$$\text{Air:} \quad \omega^* Pe^{-\frac{2}{3}} \ll 10^{-5}. \tag{3.45}$$

Equation 3.44 shows that both water and glass become unresponsive to the fluctuations at the same frequency. Thus we can use a static calibration to do measurements in water as long as condition of Equation 3.44 is met. In air, however, the limitation on the frequency becomes much more stringent if static calibration is to be used, requiring $\omega^* Pe^{-\frac{2}{3}} \ll 10^{-5}$. Moreover, in the frequency range of $10^{-5} < \omega^* Pe^{-\frac{2}{3}} < 1$ amplitude attenuation and phase lag of the substrate conduction affects the sensor signal. This can explain why it has been reported by other researchers that using a static calibration works for water but in air results in much lower r.m.s values of wall shear stress [40, 41]

How much does the frequency response of the sensor signal depend on the substrate conduction? We have to see what percentage of the signal is due to substrate conduction or indirect heat transfer. We will investigate through numerical calculations in Chapter 4.

We want to see how the size of the sensor affects the frequency response according

to the analysis we have done so far. We remind that

$$\omega^* Pe^{-\frac{2}{3}} = \frac{\omega L^2}{\alpha_f} \left(\frac{\overline{s}_x L^2}{\alpha_f} \right)^{-\frac{2}{3}}, \tag{3.46}$$

thus

$$\omega^* Pe^{-\frac{2}{3}} \propto L^{\frac{2}{3}}. \tag{3.47}$$

Hence, for a given frequency and shear rate, a smaller sensor results in a smaller $\omega^* Pe^{-\frac{2}{3}}$, which is desirable in ensuring that $\omega^* Pe^{-\frac{2}{3}} \ll 1$ is met. In other words, a smaller sensor delays the amplitude attenuation and phase lag to higher frequencies.

3.4.2 Sensor Size

From our analysis in the previous section we know that there are three limitations on the length of the sensor. Equations 3.31 shows the limit for the sensor size to avoid spatial averaging. According to Equation 3.38, the length of the sensor should not exceed some value if thermal boundary layer is to be contained within the viscous sublayer. Equation 3.40 shows that we cannot freely decrease the length of the sensor as axial diffusion will become significant, making the calibration equation invalid.

We want to look at all these limitations on the size of the sensor to find a safe range for L^+ and be able to choose the right size for the right flow conditions. If we take Prandtl number values of 0.7 and 7.0 for air and water, respectively, Equation 3.38 becomes

$$\text{Water:} \quad L^+ < 460, \tag{3.48}$$

$$\text{Air:} \quad L^+ < 46. \tag{3.49}$$

By comparing Equation 3.31 to Equation 3.48 and 3.49, we can see that the condition for spatial averaging is more restrictive. The limiting number 2 in Equation 3.31 may seem rather arbitrary. It was a result of taking width-to-length ratio of 4 to reduce the spanwise diffusion and using the $W^+ < 8$ criterion for avoiding spatial averaging. However, we can argue that spatial averaging is more restrictive on sensor length than thermal boundary layer thickness, *i.e.*, if we choose the sensor size so that we avoid spatial averaging, we do not have to worry about thermal boundary layer thickness exceeding the viscous sublayer thickness.

Let us revisit Equation 3.40 for both water and air. Again, by using $Pr = 7.0$ for

water and $Pr = 0.7$ for air, we get

$$\text{Water:} \quad L^+ > 8.4, \tag{3.50}$$

$$\text{Air:} \quad L^+ > 26.7. \tag{3.51}$$

We get yet another set of conflicting requirements, this time for the length of the sensor. Let us combine Equation 3.31 with the above equations

$$\text{Water:} \quad 8.4 < L^+ < 2, \tag{3.52}$$

$$\text{Air:} \quad 26.7 < L^+ < 2. \tag{3.53}$$

Equations 3.52 and 3.53 imply that we cannot take care of spatial averaging and axial diffusion at the same time. If we use a the sensor small enough to avoid spatial averaging, axial diffusion will become significant, and if we make the sensor large enough to reduce the effect of axial diffusion, spatial averaging will occur. This is another conflicting requirement for the single-element sensor, proving no matter what the size of the sensor is, we will have errors in our measurements.

3.4.3 Natural Convection

So far, we have assumed that natural convection is negligible, and that heat transfer from the hot-film to the fluid is done only through forced convection. We have to investigate this assumption as it may be contradicted, especially at low Peclet number where forced convection is weak and natural convection might become comparable to it.

We will use the following equation for heat transfer per unit depth due to natural convection over upward facing horizontal flat plates [42]

$$Nu_{NC} = 0.394 Gr^{\frac{1}{5}} Pr^{\frac{1}{4}}, \tag{3.54}$$

where Gr is Grashof number and subscript NC denotes heat transfer due to natural convection. The Grashof number can be calculated using

$$Gr = \frac{g\beta(T_h - T_f)L^3}{\nu^2}, \tag{3.55}$$

where g is gravitational acceleration, β is volumetric thermal expansion coefficient and

L is the characteristic length, here the sensor length. $T_h - T_f$ is the the temperature difference between the hot-film and the fluid. By looking at Equations 3.54 and 3.55, we can see that Nu_{NC} is a function of fluid properties, over-temperature and sensor length. Hence care should be taken since in low Pe the assumption of negligible natural convection might become invalid.

3.4.4 Choosing Sensor Size

Both L^+ and $\omega^* Pe^{-\frac{2}{3}}$ depend on the sensor length, shear strength and the fluid properties. We know that scale with L and $L^{\frac{2}{3}}$, respectively. For the sensor signal, or the heat transfer rate

$$Nu \propto Pe^{\frac{1}{3}} \propto L^{\frac{2}{3}}, \tag{3.56}$$

hence, Nu scales with $L^{\frac{2}{3}}$.

Before listing the shear strength dependency of these quantities, we wish to find out how they scale with a parameter which is easier to work with, *e.g.*, pipe Reynolds number

$$Re_D = \frac{UD}{\nu}, \tag{3.57}$$

where U is the average pipe velocity, D is the pipe diameter and ν is the fluid viscosity. The subscript D shows that this Reynolds number is based on the pipe diameter D, and not the sensor length. This way, studying shear strength dependency is useful because most of the available experimental data for WSS sensors are from pipe flow experiments. Moreover, choosing a range of acceptable Re_D is easier than choosing $\overline{s}_x$. By using the Haaland equation and writing the relation between the Darcy friction factor and friction velocity (see Appendix B), for $Re_D > 10^3$ we can write

$$\overline{s}_x \propto Re_D^{1.8}. \tag{3.58}$$

Using Equation 3.58 we can find Re_D dependency of Pe and hence $\omega^* Pe^{-\frac{2}{3}}$ and Nu. For L^+ we can write

$$L^+ = \frac{Lu_\tau}{\nu} = L\sqrt{\frac{\overline{s}_x}{\nu}} \propto Re_D^{0.9}. \tag{3.59}$$

Table 3.3 lists L and Re_D dependency of the quantities of our interest for a given pipe diameter and fluid properties. Note that for a given pipe Reynolds number, increasing L results in higher L^+, $\omega^* Pe^{-\frac{2}{3}}$ and Nu. The advantage of this is less axial diffusion, less phase distortion because of heat transfer fluctuations in substrate and

Table 3.3: Sensor length and pipe Reynolds number dependency of important quantities.

Quantity	L dependency	Re_D dependency
L^+	L	$Re_D^{0.9}$
$\omega^* Pe^{-2/3}$	$L^{2/3}$	$Re_D^{-1.2}$
Pe	L^2	$Re_D^{1.8}$
Nu	$L^{2/3}$	$Re_D^{0.6}$
Nu_{NC}	$L^{0.6}$	–

stronger sensor signal. The downside is higher chance of spatial averaging and the frequencies being too fast for the sensor. For a fixed sensor length, increasing Re_D results in higher L^+ and Nu and lower $\omega^* Pe^{-\frac{2}{3}}$. All these imply that we cannot use a single sensor size for all flows. We have to use smaller sensors in flows for higher Reynolds numbers to avoid spatial averaging. A constant sensor length is larger in wall units for higher Reynolds numbers.

Natural convection heat transfer rate Nu_{NC} changes linearly with over-temperature and changes with $L^{0.6}$. Nu_{NC} is a slightly stronger function of L compared to Nu and is not a function of Re_D, hence, at slow flows it may become comparable to Nu. Moreover, Nu_{NC} is a function of ΔT, but Nu is not. This means working with high over-temperatures may result in high natural convection. We will do some calculations for natural convection in section 3.7 to see how it compares to forced convection heat transfer rate of Leveque solution.

One important thing should be noted about the frequency analysis. We cannot simply argue that since $\omega^* Pe^{-\frac{2}{3}}$ changes with $Re_D^{-1.2}$, the same sensor will become more responsive in flows with higher Reynolds numbers for all range of frequencies. As the Reynolds number increases, the highest frequencies of the fluctuations increase too. To better make our point, we can scale the frequency ω with friction velocity and viscosity, *i.e.*, with inner variables of a near wall turbulent flow

$$\omega^+ = \omega \frac{\nu}{u_\tau^2} = \frac{\omega}{\overline{s}_x} = \frac{\omega^*}{Pe}. \tag{3.60}$$

Thus, ω^+ changes with $Re_D^{-1.8}$. A rather high frequency in a low Reynolds number flow, is a low frequency for a flow with higher Reynolds number. Therefore, the range

of the frequencies over which $\omega^* Pe^{-\frac{2}{3}}$ must be $\ll 1$ to have a highly responsive sensor, changes with Re_D. We can replace ω^* with $\omega^+ Pe$ and get

$$\omega^* Pe^{-\frac{2}{3}} = \omega^+ Pe^{\frac{1}{3}}. \tag{3.61}$$

Now for a constant ω^+, which translates to higher frequencies in flows with higher Reynolds numbers, $\omega^* Pe^{-\frac{2}{3}} = \omega^+ Pe^{\frac{1}{3}}$ changes with $Re_D^{0.6}$. Hence, at high Reynolds numbers, the condition for responsiveness of the sensor to the fluctuations with the highest frequencies becomes more severe. Since for constant ω^+, this term still changes with $L^{2/3}$, a smaller sensor helps to relax this condition.

3.5 Substrate Heat Conduction

As stated in Chapter 2, the indirect heat transfer to the fluid, through the substrate can be significant. We have already talked about the errors introduced in measurements because of the phase lag of the substrate response to fluctuations. However, it should be noted that the conditions of Equation 3.42 and 3.43 are for our simple model, that is a flow with a sinusoidal shear stress with frequency of ω. The actual turbulent flow in which the measurements are going to be done, will be much more complex, and will have fluctuations with a range of frequencies and amplitudes instead of one. Hence, at some instances during the measurements, either the condition of Equation 3.42 or Equation 3.43 may hold true, and at some instances neither of them.

Recall that the sensor signal that we get comes from the amount of heat generated in the sensor to keep the temperature constant. Thus, it accounts for the total heat leaving the sensor. This includes both the heat going directly to the fluid, and the heat going to the substrate. Since, the heat transfer through the substrate depends on both fluctuation strength and frequency, and its dependency is different to that of the fluid, it is impossible to know how much of the signal is due to the heat transfer to the substrate. Note that it is not easy to calibrate out this through calibration, since the calibration curve depends on the measurement in which it has been obtained. Therefore, instead of trying to quantify the errors due to heat transfer through substrate, it is better to remove the effects of substrate heat conduction to avoid any uncertainties. This is what we wish to achieve by using guard-heaters.

In addition to the problem mentioned above, *variable spatial averaging* is an issue

too. The heat going into the substrate will eventually go to the fluid. Thus, the heat transfer from the sensor to the fluid now happens over a length much larger than the physical length of the sensor. Hence, we should use *effective length* L_e instead of L in all equations. This introduces a non-linearity in the governing equations and makes the limiting conditions on the sensor length more severe. The amount of indirect heat transfer, and consequently L_e, depends on the shear strength. This makes the analysis of the single-element sensor much more difficult since our characteristic length is now variable.

If the total heat going out of the sensor is Q_{tot}, the heat going directly to the fluid is Q_F and the heat going to the substrate is Q_S, then at any instant the following relation is true

$$Q_{tot} = Q_F + Q_S. \tag{3.62}$$

To be consistent, we will non-dimensionalize the heat transfer rates by dividing them by $k_f \Delta T$ and rewrite Equation 3.62 as

$$Nu_{tot} = Nu_F + Nu_S. \tag{3.63}$$

Since the temperature is to be kept constant, the total heat leaving the sensor must be balanced by the heat generated in the hot-film

$$\frac{I^2 R}{W k_f \Delta T} = Nu_{tot}, \tag{3.64}$$

where I and R are electrical current and resistance of the hot-film respectively. Note that I^2R/W is the rate of heat generation per unit depth in the sensor. We can now write

$$\frac{E^2}{RW k_f \Delta T} = \frac{I^2 R}{W k_f \Delta T} = Nu_F + Nu_S, \tag{3.65}$$

where E is voltage.

If Nu_S is comparable to Nu_F, which is reported true (see Chapter 2), a significant uncertainty is introduced in the measurements. The frequency response of the sensor depends on both substrate and fluid. If Nu_{tot} is dominated by Nu_S, then the frequency response of the sensor follows that of the substrate closely. This means for the case of air-glass, the truncation of the spectrum happens much earlier. By using guard-heaters, we want to eliminate Nu_S and get as close to $E^2/RWk_f\Delta T = Nu_F$ as possible. The variable effective length will also vanish as a result of this.

3.5.1 Signal Strength and Signal Quality

A significant portion of the signal we get from the sensor can be due to the heat transfer to the substrate. By using the guard-heaters, we wish to decrease or completely eliminate this portion of the signal, so that the signal is only due to the heat transfer to the fluid. Guard-heaters do this by reducing the temperature gradient near the sensor in the substrate. However, an inevitable outcome of using such method is decreased heat transfer rate to the fluid as well. Hence by using the guard-heaters we will see reduced indirect heat transfer rate, but at the cost of reduced direct heat transfer rate as well. The combined result is a weaker signal, but one which is less due to the indirect heat transfer.

When reporting the results of the different sensor designs and comparing their performances, it is necessary to be able to compare both the signal strength Nu_F and the ratio of the direct heat transfer rate to the total heat transfer rate Nu_F/Nu_{tot}. From now on, we will use Nu_{signal} for the total heat transfer rate to emphasize that the signal we get from the sensor is equal to the total rate of heat going out of the sensor and depends on both Nu_F and Nu_S

$$Nu_{signal} \equiv Nu_{tot} = Nu_F + Nu_S. \tag{3.66}$$

It is important to bear in mind that although high signal strength is better when it comes to signal-to-noise ratio, it might be due to high substrate heat conduction and might result in inaccurate measurement data. We will use the term *signal quality* for the ratio of the direct heat transfer to the total heat transfer rate Nu_F/Nu_{signal} from now on in this thesis, to stress that a signal is better or has higher *quality* if a high portion of it comes from the direct heat transfer rate.

In Chapter 4, we will check both signal strength Nu_{signal} and signal quality Nu_F/Nu_{signal} to compare the performance of the different sensor designs.

3.5.2 Equivalent Length

We talked about the effective length L_e of the sensor, and that it changes with shear strength. We are seeking a relation for L_e to see how much larger L_e is compared to L. We can obtain such a relation if we take the amount of total heat transfer rate from the sensor Nu_{signal} and assume it happened from a sensor with the physical

length of L_e, obeying the Leveque relation

$$Nu_{signal} = 0.807 \left(\frac{\overline{s}_x L_e^2}{\alpha_f} \right)^{\frac{1}{3}}. \tag{3.67}$$

We can now right L_e as

$$\frac{L_e}{L} = Pe_L^{-\frac{1}{2}} \left[\frac{Nu_{signal}}{0.807} \right]^{\frac{3}{2}}, \tag{3.68}$$

where $Pe_L = \overline{s}_x L^2/\alpha_f$ is Peclet number based on physical length of the sensor. We will call this a *Leveque equivalent length* or in short equivalent length, which is an estimation of the effective length of the sensor. This equivalent length is based on Nu_{signal}. We can define an equivalent length based on Nu_S or Nu_F, and call them $L_{e,S}$ and $L_{e,F}$ respectively. However, since L_e does not change linearly with Nu, we cannot simply write $L_e = L_{e,F} + L_{e,S}$. If we manage to eliminate indirect heat transfer we will have $L_{e,S}/L \approx 0$ and thus $L_e/L \approx L_{e,F}$.

3.6 Guard-Heated Design: Predictions

So far in this chapter we have analyzed hot-film WSS sensors, the assumptions, deficiencies and design requirements with the single-element design in mind. We introduced the idea of guard-heating in Chapter 2 and briefly explained what improvements we wish to make by utilising guard-heaters. Now that we have studied the single-element design in depth, and managed to formulate the numerous constraints on length, frequency and shear rate, we can make better predictions on the guard-heater design and the improvements it may bring. We will go through the assumptions of the Leveque solution and all the items on the check-list we made earlier in this chapter and one-by-one analyze the constraints and try to predict how the guard-heated design will perform.

By adding the in-plane guard-heater (Figure 2.5-a), the sensor will be surrounded by a plate with the same temperature as its own. As a result, the temperature gradient near the edges of the sensor will be reduced significantly. Because of the lower temperature gradient, heat diffusion will be much lower around the sensor in both axial and spanwise directions. This makes the assumptions of negligible axial and spanwise diffusion valid, even at low shear rates. Moreover, the lower limit on L^+ vanishes because of low axial diffusion, and no more we have to worry about the edge

effects dominating heat transfer over the sensors. With the lower limit on the sensor length gone, we can make the sensors as small as the micro-fabrication, signal-to-noise ratio and natural convection considerations allow us. By using smaller sensors we will have better spatial resolution and can avoid spatial averaging.

Another important benefit of the guard-heater is reducing the amount of heat transfer to the substrate Nu_S. The first plane reduces axial and spanwise temperature gradient and hence diffusion in both fluid and solid. However, wall-normal temperature gradient still exists. We have to rely on our numerical model to see to what extent will Nu_S be reduced in the single-plane guard-heated design. The second plane (Figure 2.5-b) reduces the wall-normal temperature gradient in the substrate and blocks any heat going to the substrate. This should result in $Nu_S \approx 0$ which is a significant achievement. By blocking heat from going into the substrate, the sensor signal will purely consist of the heat going directly to the fluid

$$\frac{E^2}{RWk_f\Delta T} \approx Nu_F. \tag{3.69}$$

By blocking the heat transfer to the substrate the problem of variable spatial averaging vanishes. For the frequency response of the sensor, we do not have to worry about the dynamic behaviour of the substrate. Since the sensor signal now only depends on the heat transfer to the fluid, we are only limited by the response of the fluid and the several limits on the frequency will reduce to the limit of Equation 3.41. Thus the signal response of the sensor will only drop when the fluctuations become too fast for the fluid heat transfer, meaning the frequency response of the sensor signal will be only limited by the fluid thermal inertia.

3.7 Sample Calculations

In this section, we will quantitatively investigate the constraints we have found throughout this chapter, and choose some reasonable values for the parameters for our numerical analysis. There are several determining quantities, *e.g.* sensor length, over-temperature, fluid properties, shear strength, shear frequency, *etc.* We can reduce the number of these quantities by choosing suitable non-dimensional parameters, as we have done so far. However, we still have to do our analysis for a range of values for quantities such as Pe and ω^*. Moreover, we want to do our investigation (simple calculations here and numerical analysis in the next chapter) in physically

reasonable coordinates, *i.e.*, we want to avoid working in a range of dimensionless parameters which correspond to unrealistic dimensional values, like very high velocities or frequencies.

Table 3.4: Values of different parameters for $L = 10\mu m$.

		$V(m/s)$	Pe	$\tau_w(Pa)$	$\overline{s}_x(1/s)$	L^+	Nu_{lev}	Nu_{NC}
Water	$Re_D = 10^5$	0.34	0.17	0.25	250	0.16	0.45	0.097
	$Re_D = 10^6$	3.4	11.26	16.35	16237	1.27	1.81	
Air	$Re_D = 10^5$	5	0.017	0.06	3515	0.16	0.20	0.032
	$Re_D = 10^6$	50	1.167	4.21	228547	1.27	0.82	

To begin the process of choosing a value or a range for different quantities, we will consider fully developed turbulent flow in a pipe, and begin with a pipe diameter and pipe Reynolds number. We choose a pipe diameter of $D = 30cm$, pipe Reynolds numbers of $Re_D = 10^5$ and $Re_D = 10^6$, sensor length of $L = 10\mu m$. Table 3.4 lists values of several parameters for two pipe Reynolds numbers for both water and air. The quantity V is the average pipe velocity.

We can see from Table 3.4 that we will be dealing with low Peclet numbers, especially for air, since the sensor size is very small. This will lead to small values of Nu, which would be problematic if heat transfer due to natural convection Nu_{NC} becomes comparable to Nu, or if signal-to-noise ratio becomes very small. Additionally, the equivalent length of the sensor will be much higher for low Peclet numbers.

The listed natural convection heat transfer rates Nu_{NC} are calculated using Equation 3.54 and assuming over-temperature of $\Delta T = 40K$. It can be seen that at $Re_D = 10^6$ natural convection is small compared to the Leveque heat transfer rate, but it becomes more comparable at lower Re_D. We should have this in mind that the actual sensor signal might be smaller than what the Leveque solution predicts. The sensor length has a safe value in wall-units regarding spatial averaging condition ($L^+ < 2$). Note that Nu_{lev} scales with $L^{0.67}$ and Nu_{NC} with $L^{0.6}$. Hence increasing the sensor length by a factor of 10 increases the Nu_{lev} to Nu_{NC} ratio by 16%. However, L^+ scales with L, thus it will increase by a factor of 10, which might cause spatial averaging. This, again, proves that we should not expect one single sensor design to work in all flows. We can use larger sensors in low Re_D flows to get stronger signals provided we avoid spatial averaging, and use smaller sensors in faster flows.

Table 3.5: Values of different parameters for for $L = 100\mu m$.

		$V(m/s)$	Pe	$\tau_w(Pa)$	$\overline{s}_x(1/s)$	L^+	Nu_{lev}	Nu_{NC}
Water	$Re_D = 10^5$	0.34	17.33	0.25	250	1.57	2.1	0.38
	$Re_D = 10^6$	3.4	1126.5	16.35	16237	12.7	8.4	
Air	$Re_D = 10^5$	5	1.79	0.06	3515	1.57	0.98	0.12
	$Re_D = 10^6$	50	116.7	4.21	228547	12.7	3.94	

To better see the effect of using a larger sensor, we can look at Table 3.5 which shows the same parameters of Table 3.4 but for sensor length of $L = 100\mu m$. We can see slight improvements in Nu_{lev}/Nu_{NC} ratio but at the cost of low spatial resolution at $Re_D = 10^6$. At $Re_D = 10^5$ we can use an even larger sensor without violating the spatial averaging condition, to obtain a stronger signal and higher Peclet number.

We can check Equations 3.31 and 3.38, and see what will be the limits on the physical length of the sensor L at $Re_D = 10^5$ and $Re_D = 10^6$. The spatial averaging condition, Equation 3.31, yields $L < 127\mu m$ at $Re_D = 10^5$ and $L < 16\mu m$ at $Re_D = 10^6$ for both water and air. The axial diffusion condition, Equation 3.40, at $Re_D = 10^5$ corresponds to $L > 533\mu m$ in water and $L > 1.7mm$ in air, and at $Re_D = 10^6$ corresponds to $L > 66\mu m$ in water and $L > 210\mu m$ in air.

Table 3.6: Frequency ω corresponding to $\omega^* Pe^{-\frac{2}{3}} = 1.0$.

		$L = 10\mu m$	$L = 100\mu m$	ω_η
Water	$Re_D = 10^5$	$442Hz$	$96Hz$	$350Hz$
	$Re_D = 10^6$	$7.2kHz$	$1.6kHz$	$11kHz$
Air	$Re_D = 10^5$	$13.0kHz$	$2.9kHz$	$5.2kHz$
	$Re_D = 10^6$	$217kHz$	$46.8kHz$	$170kHz$

We stated earlier that the response of the fluid will drop if $\omega^* Pe^{-\frac{2}{3}}$ becomes ≈ 1. We want to see what this number means in terms of dimensional frequency ω. We will again use the aforementioned values of Re_D to calculate mean Peclet numbers. The frequencies corresponding to $\omega^* Pe^{-\frac{2}{3}} = 1.0$ are listed in Table 3.6. For reference, the frequencies calculated from the Kolmogorov microscales (ω_η) are also listed. As expected, the smaller sensor in theory is able to resolve fluctuations with frequencies comparable to Kolmogorov frequencies, especially in air. The numbers show the

ability of the hot-film sensors to do measurements at very high frequencies in theory. Table 3.7 shows the frequencies of Table 3.6 in wall-units ω^+. For reference, the median frequency of s_x for pipe turbulence is $\omega^+_{median} \cong 2\pi(0.009)$ [38].

Table 3.7: Dimensionless frequency ω^+ corresponding to $\omega^* Pe^{-\frac{2}{3}} = 1.0$.

		$L = 10\mu m$	$L = 100\mu m$
Water	$Re_D = 10^5$	1.80	0.38
	$Re_D = 10^6$	0.45	0.09
Air	$Re_D = 10^5$	3.89	0.83
	$Re_D = 10^6$	0.95	0.20

3.8 Chapter Summary

In this chapter, we investigated the hot-film WSS sensors by non-dimensionalizing the governing equations, finding the determining dimensionless quantities and listing the design limits of the conventional single-element sensors. As we saw, we cannot use one sensor to do measurements in all flows. The problem of choosing the right sensor for a flow is described by Nu, Nu_{NC}, Pe, ω^*, K, L^+ and L/W. Most of these dimensionless quantities depend on the flow conditions and the sensor size, which makes choosing a suitable sensor for WSS measurements a difficult and cumbersome task.

The several, in some cases conflicting, design requirements for the conventional single-element sensor makes it impossible to find a window for measurements which are free of significant errors. Spatial averaging and thermal boundary layer concerns dictate the need for smaller sensors. However, errors introduced because of axial heat conduction in the fluid introduce constraints on how small we can make the sensors. Moreover, substrate conduction introduces a lot of uncertainties in the dynamic behaviour of the conventional hot-film sensors, and makes laminar calibrations unusable in turbulent flows. We expect to remove these conflicts and uncertainties by using guard-heaters to remove the effects of substrate conduction from the sensor signal.

By connecting our non-dimensional analysis to a physical problem (here pipe flow), and examining the dependency of the determining parameters and the limits on sensor length and flow characteristics (Re_D), we were able to present a framework

for choosing a sensor for given flow conditions. In the next chapter, we will numerically study the performance of the single-element and guard-heated sensor designs to check the validity of our analysis in this chapter, and address the unanswered questions.

Chapter 4

Results and Discussion

In this chapter we will present the results of our numerical analysis of hot-film WSS sensors. We will begin with introducing the numerical model we have built, describing the equations solved, the geometry, boundary conditions and data post-processing, and then show the results of our steady and unsteady models.

4.1 Numerical Model

Our model was built in COMSOL Multiphysics software, using the *Heat Transfer* module. COMSOL Multiphysics uses finite element methods to solve the problems defined. We have used the *Stationary* solver to solve our steady-state problems and set the initial conditions for the unsteady problems. The unsteady problems were solved using the *Time-Dependent* solver. Six different models were built to solve for air and water in single-element (SE), single-plane guard-heated (GH1P) and two-plane guard-heated (GH2P) designs. In all models, the substrate material was glass. The results were saved in separate files and post-processed with MATLAB. All plots in this chapter were created using MATLAB.

4.1.1 Geometry and Parameters

Figure 4.1 shows a schematic of the geometry created for our numerical model. The dimensions of the geometry are different for water and air and they were set after doing a domain size independence check.

Table 4.1 lists the parameters set for each model. For the steady results, a parametric study was done by setting a list of values for Pe. COMSOL solves for every

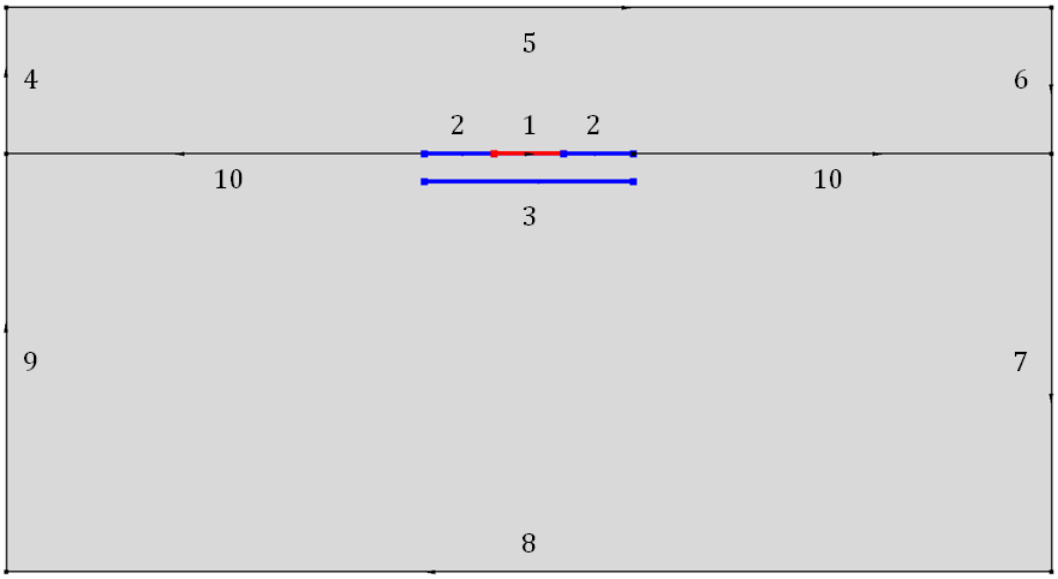

Figure 4.1: The model built with COMSOL for numerical analysis. It includes solid substrate, fluid and the hot-film. The lengths are not to scale and have been exaggerated for clarity. Edge 1 indicates the sensor, edge 2 the in-plane guard-heater and edge 3 the second guard-heater. Edges $4-10$ identify external boundaries and fluid-solid interface sections. See Table 4.2 for boundary and interface conditions.

value of the Pe, and saves the results for each one. The range of Pe was set for each case to correspond to Re_D values of 5×10^4 to 5×10^6. For sensor length of $L_{hf} = 10\mu m$ that was used in our models, this range of Re_D results in Pe range of $2-26$ for water and $0.05-2.7$ for air. The results for extended ranges of Pe values can be seen in Appendix C.

All lengths and the mesh size were set after checking mesh and domain-size independence, which will be discussed later. For the guard-heated designs, additional parameters were set. The length of sensor plus the in-plane guard-heater is L_{hf}, which was set equal to $50\mu m$, five times the length of the sensor. For the two-plane design, the gap between two planes H_G was set equal to $0.2\mu m$. It should be noted that in the guard-heated designs the dimensions of the domain were set relative to the total heated length L_{hf} instead of the sensor length L. For instance, the upstream length was $150L_{hf}$, not $150L$. The minimum and maximum mesh size, however, were set relative to the sensor length again to avoid loss of resolution near the sensor.

The fluid temperature T_f and the hot-film temperature T_h were set equal to $293.15K$ and $333.15K$ to yield over-temperature of $40K$. However the absolute val-

Table 4.1: List of parameters set in the model.

Parameter	Description	Value	
		Water	Air
L	Sensor Length	$10\mu m$	$10\mu m$
L_U	Upstream Length	$50L$	$150L$
L_D	Downstream Length	$50L$	$600L$
L_S	Substrate Height	$40L$	$150L$
L_F	Fluid Length	$15L$	$40L$
T_f	Fluid Temperature	$293.15K$	$293.15K$
T_h	Hot-Film Temperature	$333.15K$	$333.15K$
Pe	Peclet Number	–	–
$dxmin$	Minimum Mesh Size	$L/400$	$L/100$
$dxmax$	Maximum Mesh Size	$4L$	$4L$
L_{hf}	Total Heated Length	$5L$	$5L$
H_G	The Gap Between Two Planes	$0.2\mu m$	$0.2\mu m$

ues of the temperatures are not important for presentation of results, which are in non-dimensional form.

4.1.2 Mesh and Domain Size Independence

Several parameters listed in Table 4.1 contribute to the domain size. For both water-glass and air-glass models, each length was increased until the change in Nu_F and Nu_S became less than 1%. We started by setting L_U, L_D and L_S equal to $10L$ and kept increasing each one. For each model we reached independence at the values listed in Table 4.1. For the guard-heated models, we used L_{hf} which is the length of the sensor plus the guard-heater to set the domain size. Hence, the domain was much bigger for the guard-heated designs.

We used *mapped* meshing, producing a regular rectangular grid, for the first row of cells over and under the sensor and *triangular* everywhere else. The reason we used mapped meshing near the sensor is that we use the temperature over the first row of nodes over and under the sensor to calculate direct and indirect heat transfer rates. Thus we wanted to have a consistent resolution over the length of the sensor. We

control the mesh size by using a minimum mesh size dx_{min} and a maximum allowable mesh size dx_{max}. The distance between the first row of nodes near the sensor and the sensor is set as dx_{min} and the maximum allowable mesh size fore the triangular mesh over the domain is set as dx_{max}. We started with $dx_{min} = L/50$ and decreased the value of dx_{min} until the changes in Nu_F and Nu_S were less than 1%. We reached mesh size independence at $dx_{min} = L/400$. However, at $dx_{min} = L/100$ the change in the heat transfer rates were not very high, being at about 2% for the very low Pe values.

In the guard-heated air-glass model we could not use the domain and mesh sizes found through the dependence checking process at the same time. The reason is that since we used the total heated length instead of the sensor length for the domain size, the dimensions were much larger compared to the single-element model. On the other hand, we set the minimum mesh size using the sensor length. The total length and height of the domain were $L_x = 751L_{hf}$ and $L_y = 191L_{hf}$ or in terms of the sensor length, $L_x = 3755L$ and $L_y = 955L$. The minimum mesh size found in the mesh independence process was $dx_{min} = L/400$. The COMSOL software was not able to create geometry and mesh properly with these lengths, which vary about 1.5×10^6 times in magnitude. Thus we had to make a compromise. Since using $dx_{min} = L/100$ would not change the results significantly, we changed the minimum mesh size and left the domain size unaltered.

Values of L_U, L_D, L_S and L_F were initially set and then increased until the results (direct and indirect heat transfer rates) changed by less than 1%.

4.1.3 Equations and Boundary Conditions

The equations solved by COMSOL in the fluid and solid are two-dimensional forms of the energy equations written in the previous chapter. In the model built for the steady-state problem, the vector form of these equations for fluid and solid are

$$\rho_f C_{p,f} \mathbf{u}.\nabla T = \nabla.(k_f \nabla T), \tag{4.1}$$

$$\nabla.(k_s \nabla T) = 0, \tag{4.2}$$

where ρ, C_p and k are density, thermal capacity and thermal conductivity, respectively, u is velocity vector, T is temperature, and subscripts f and s denote fluid and

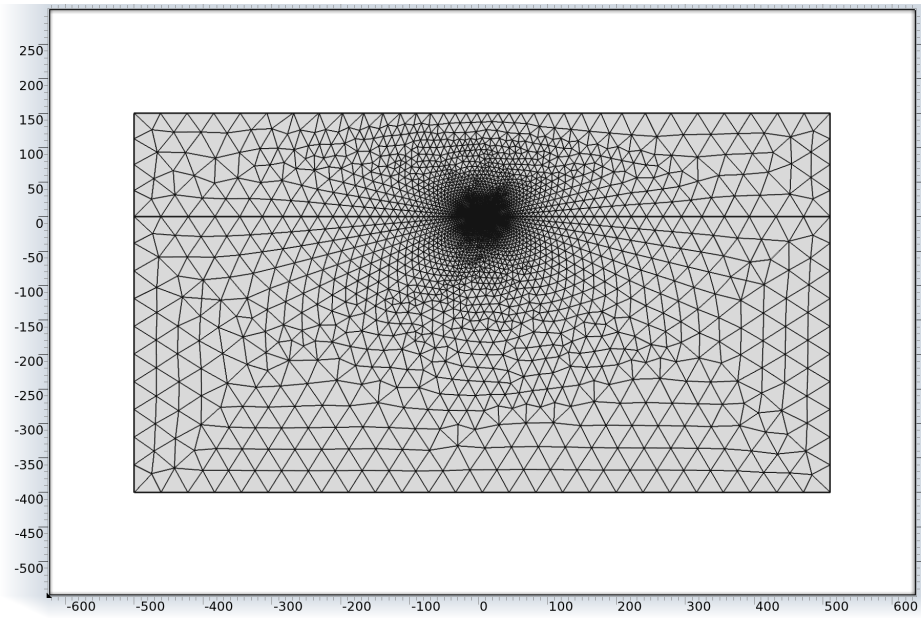

(a) Water

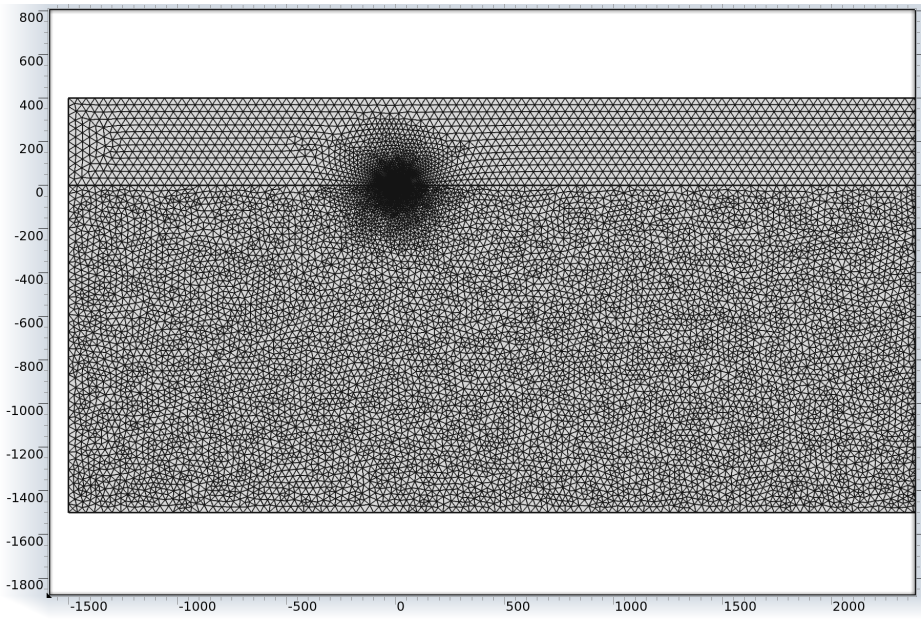

(b) Air

Figure 4.2: The mesh created in COMSOL for water-glass and air-glass models. The mesh size is very fine near the sensor and becomes coarser as we go away from it. The minimum and maximum mesh sizes are predefined in the model. The domain is much larger for the air-glass model because of higher heat penetration in the substrate.

solid respectively. In the time-dependent model, the equations are

$$\rho_f C_{p,f} \frac{\partial T}{\partial t} + \rho C_{p,f} \mathbf{u}.\nabla T = \nabla.(k_F \nabla T), \tag{4.3}$$

$$\rho_s C_{p,s} \frac{\partial T}{\partial t} = \nabla.(k_s \nabla T). \tag{4.4}$$

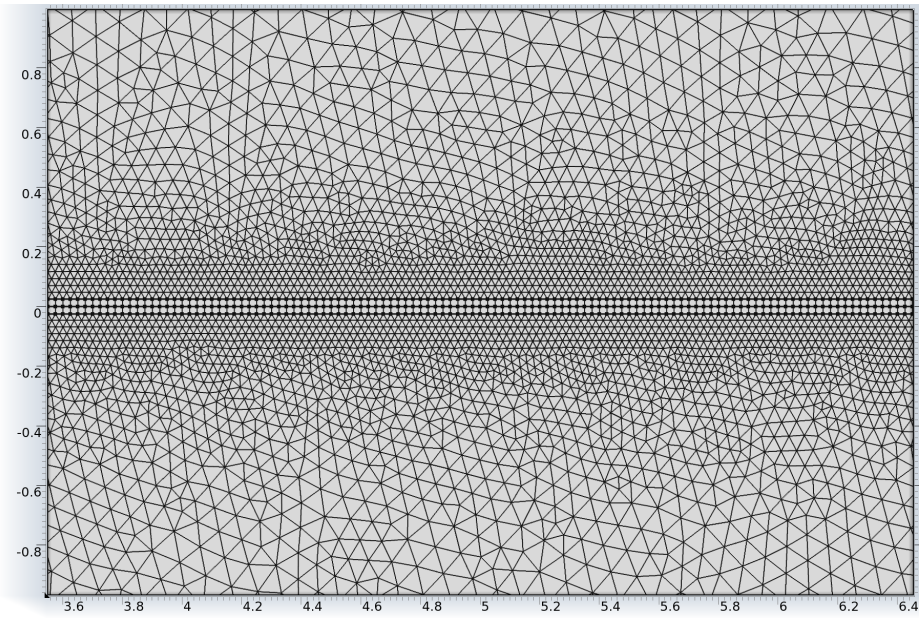

Figure 4.3: The mesh is very fine near the sensor to have better accuracy. The temperature gradient is high near the sensor and requires fine mesh size. The first row of cells near the sensor has the minimum size defined in the model.

In both set of equations, $\mathbf{u}$ is the velocity vector in the fluid. The x component of $\mathbf{u}$ is set equal to $s_x y$ where $s_x = \alpha_f Pe/L^2$ is the shear rate and y is the wall-normal coordinate. In the steady model, where we want to see how heat transfer rates change with shear rate, a *parametric study* is done using Pe, where the value of Pe is changed according to a range of values defined by us. The software then changes Pe according to the range given and saves the values of the parameters defined by us. In the steady analysis, we defined Nu_F and Nu_S as heat transfer rates from the sensor to the fluid and solid, and saved them at each run. In the unsteady or time-dependent runs, we defined a sinusoidal function for s_x as $s_x = \overline{s}_x(1 + a\sin(\omega t))$ and set the velocity field as before. $\overline{s}_x$ was defined as $\overline{s}_x = \alpha_f Pe/L^2$ with Pe being the average Peclet number. We set the amplitude a and frequency ω of the fluctuations in each run.

Figure 4.1 shows the computational domain. The type of boundary conditions set at each edge are listed in Table 4.2. No boundary conditions needed to be set on the interface (edge 10) and COMSOL automatically satisfied the interface conditions.

Table 4.2: List of the boundary conditions set in the model shown in Figure 4.1.

Fixed Temperature $T = T_h$	$1-3$
Fixed Temperature $T = T_f$	4
Thermal Insulation $-\mathbf{n}.(-k\nabla T) = 0$	$5-9$

4.1.4 Solvers and Convergence

COMSOL automatically chooses a solver suitable for the modelled physics. In both our steady and unsteady models, the solver was *Fully Coupled* with *Direct Linear Solver*. The linear solver was *PARDISO*. All internal parameters of the solver were set automatically.

In the time-dependent model, the time-step was fixed as $dt = T/100$ where $T = 2(2\pi/\omega)$ is the total time required for two complete cyclic variations of the shear rate. The COMSOL solver takes additional steps in between the defined time-steps if necessary.

The convergence criterion for the runs were set on the error. The *absolute* and *relative tolerances* control the error in each integration step. Let U be the solution vector corresponding to the solution at a certain time-step, and let E be the solver's estimate of the local error in U committed during this time step. The step is accepted if

$$\left(\frac{1}{N} \sum \left(\frac{|E|}{A_i + R|U_i|} \right)^2 \right)^{1/2} < 1, \tag{4.5}$$

where A_i is the absolute tolerance for degree of freedom i, R is the relative tolerance, and N is the number of degrees of freedom. The relative tolerance R was set equal to 10^{-3} and the absolute tolerance A as 10^{-5}.

4.1.5 Data Post-Processing

A series of MATLAB scripts were written and used to read the exported results of COMSOL and create the desired plots for this thesis. For each design (SE, GH1P or GH2P) a series of results, including Pe, Nu_F and Nu_S, were exported from COMSOL and written in a file. For the unsteady runs, for each frequency the solution was saved in a separate file, containing values of Pe, Nu_F and Nu_S for each time-step. A script was written for each model to read the steady and unsteady solutions, calculate various parameters such as frequency response and phase lag, and write them as a

MATLAB data-set. An other script was written to read and collect the data-sets of all models and create the plots presented in this thesis.

4.1.6 Model Validation

Since there is not an analytical solution available for the problem in hand, to validate our numerical model we had to use the closest physical problem for which a solution exists, which is the Leveque solution. Hence, we removed the substrate and extended the hot-film all the way to the right boundary of the domain. We numerically solved the problem once with axial conduction turned on and then with axial conduction turned off and compared the results to that of the Leveque solution. Figure 4.4 shows the results for both cases. Pe was changed from a low value of 0.1 to a high value of 1000. Water was used as the fluid but in the Leveque problem the results do not depend on the fluid properties if they are non-dimensionalized correctly.

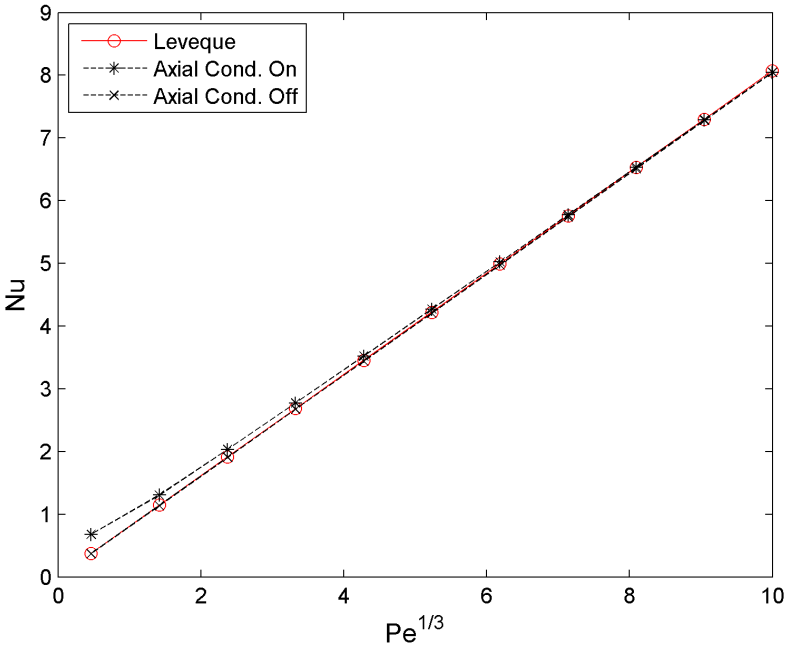

Figure 4.4: Rate of heat transfer to fluid (Nu) vs. Pe in the simulated Leveque problem. When axial diffusion is turned off, the numerical results agree well with the analytical results. With axial diffusion turned on, the results deviate from the Leveque solution at low Pe values.

The results agree well with the Leveque solution over the whole range of Pe when axial conduction is turned off. When axial conduction is turned on, the results deviate

from the Leveque solution at low values of Pe. We justify this by recalling that the Leveque solution completely neglects axial conduction, an assumption that is not true at low Pe. Fitting a linear line to both data gives $Nu = 0.805Pe^{1/3} - 0.003$ with norm of residuals of $R = 0.003$ when axial conduction is turned off, and $Nu = 0.779Pe^{1/3} + 0.216$ with $R = 0.125$ and axial conduction is turned on. Fitting a quadratic or cubic curve to the data with axial diffusion turned on gives a much lower value of residuals. We will have more to say about axial diffusion later in this chapter.

4.2 Results

Figure 4.5 shows the temperature contours for water-glass and air-glass models. We can see from the contours that the substrate warms up and causes preheating of the fluid upstream of the sensor. This heat conduction in the substrate is significant in the air-glass case. Note that the domain size shown in the air-glass model is much larger than that of the water-glass model. Figure 4.6 shows a close-up of the contours near the sensor for the water-glass model. Note that for the low Pe model heat conduction to the substrate and hence preheating of the fluid is higher, and the thermal boundary layer is thicker.

4.2.1 Guard-Heated Design Analysis

In our models, we have finally placed the sensor on the center of the guard-heater, and taken the total length of the hot-film L_{hf}, consisting of the sensor and the guard-heater, as five times the length of the sensor L. To see if there is a preferable or an optimum position for the sensor within the guard-heater, in terms of indirect heat transfer, we changed the position of the sensor and calculated Nu_S for each case. We repeated the same procedure for different Pe values for both water and air. We found that the sensor should be placed near the center of the guard-heater, between 0.4 and 0.6 of the length of the guard-heater.

How sensitive is the design to changing in-plane guard-heater length? To investigate this we changed the length of the in-plane guard-heater in both single and two-plane designs. In the single-plane design, reducing the guard-heater length results in less preheating and a higher temperature gradient around the sensor. Thus, both Nu_S and Nu_F increase, but the ratio Nu_F/Nu_{signal} decreases. Hence, we will

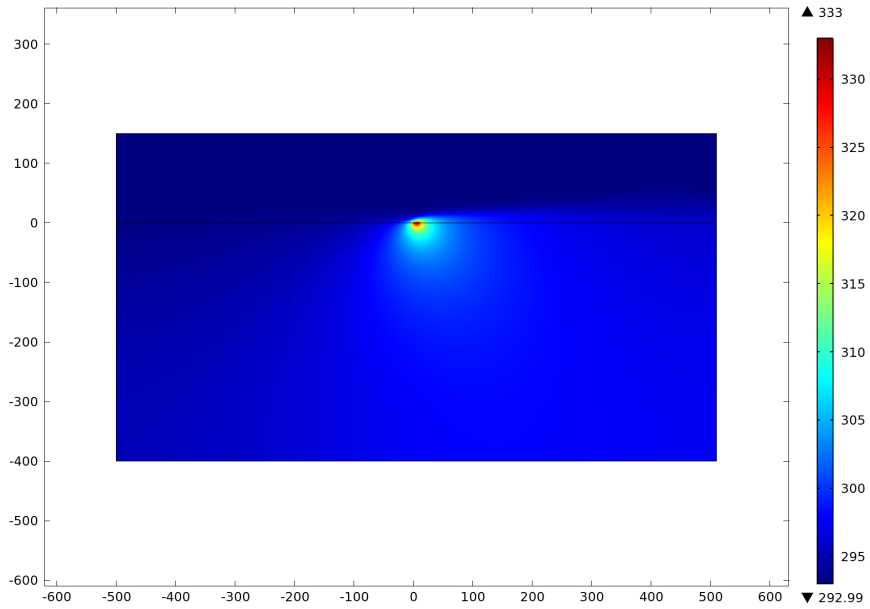

(a) Water, $Re_D = 10^6$, $Pe = 11.26$

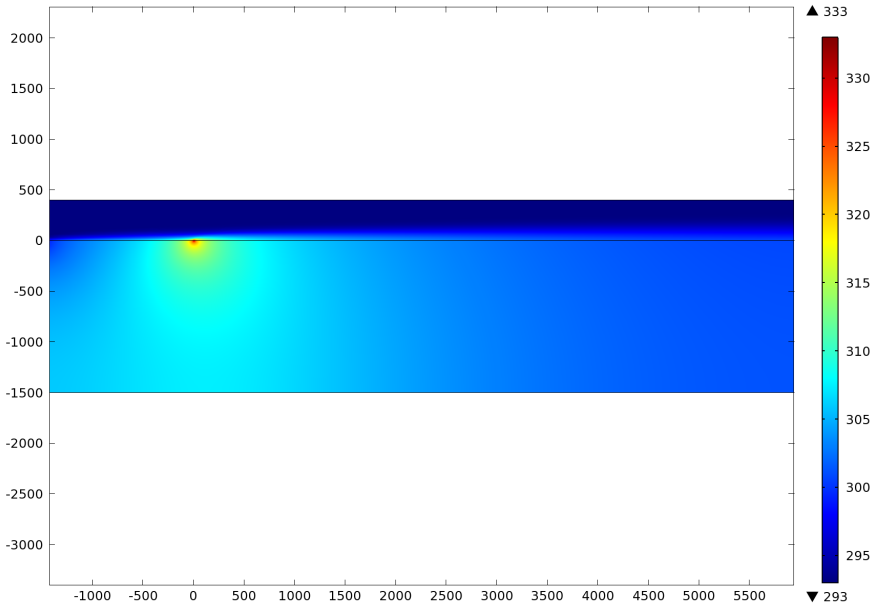

(b) Air, $Re_D = 10^6$, $Pe = 1.17$

Figure 4.5: Absolute temperature contours at $Re_D = 10^6$ for both water-glass and air-glass. The heat diffuses to the substrate and raises its temperature. The substrate temperature rises significantly in air-glass.

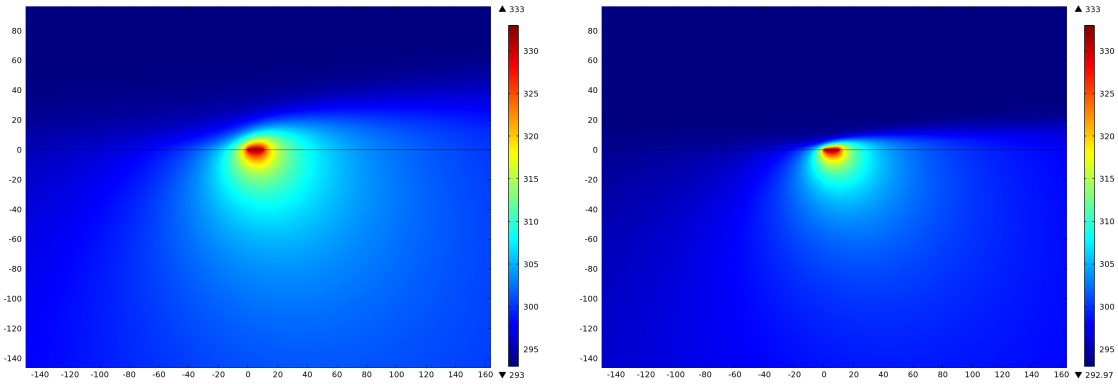

(a) $Pe = 2$ (b) $Pe = 26$

Figure 4.6: Absolute temperature contours for water-glass. At lower Pe the thermal boundary layer becomes thicker and heat diffusion to the substrate increases. The heat diffused into the substrate goes to the fluid eventually from both upstream and downstream of the sensor.

get a stronger signal but with lower quality. In the two-plane design, we first fixed the length of the second guard-heater as five times the length of the sensor, and changed the length of the guard-heater. Then, we changed the length of both guard-heaters at the same time. The schematics of the models and their results can be seen in Appendix C.

4.2.2 Steady-State Results

This section includes the results of the steady-state model. We first want to focus on the static behaviour of the sensor, and investigate various quantities such as the amount of heat transfer to the substrate, equivalent length, signal strength and quality, and the validity of the assumptions made for the Leveque solution, before investigating the dynamic behaviour of the sensor.

Axial Diffusion

One of the assumptions made to obtain the Leveque solution was that axial diffusion of heat in the fluid is negligible. This assumption resulted in a constraint on the length of the sensor (Equation 3.40). In the previous chapter, we claimed that using the in-plane guard-heater reduces axial diffusion by decreasing the temperature gradient, and thus eliminates the limit on the sensor length. We showed that even without a substrate, the heat transfer rates deviate from the Leveque solution because of axial

diffusion at low Pe values (Figure 4.4). Since our numerical analysis is done in a low range of Pe (a result of small sensor length), we will reproduce the plot of Figure 4.4 in a low range of Pe values and for a sensor length of $L = 10\mu m$. We will compare the results for both single-element and guard-heated designs to see how axial conduction affects their results.

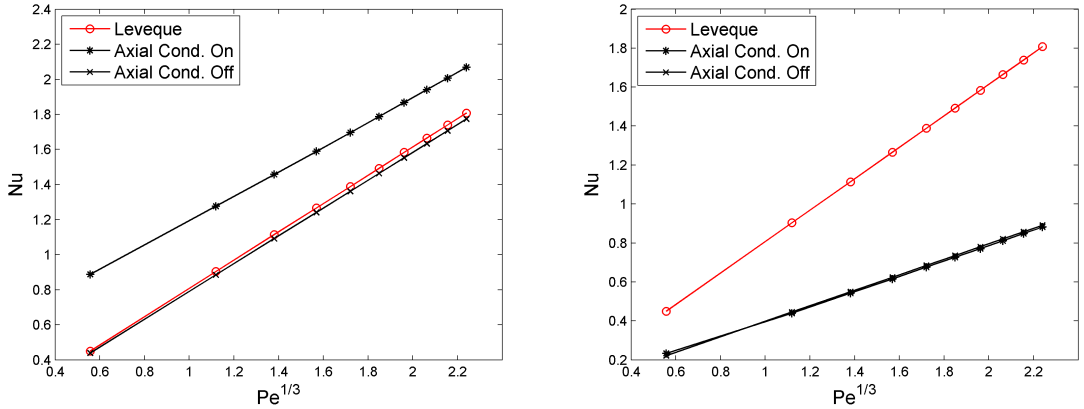

(a) Single-element (b) Guard-heated

Figure 4.7: Rate of heat transfer to the fluid (Nu) vs. Pe for single-element and guard-heated sensors without a substrate. The guard-heated sensor has lower heat transfer rate than that of the Leveque solution because of the pre-heating done by the guard-heater. The guard-heater forces zero axial temperature gradient over the edge of the sensor and removes the effects of axial diffusion on results.

Figure 4.7 shows that the $Nu-Pe$ curve of a guard-heated sensor does not depend on axial diffusion. However, the same cannot be said for a single-element sensor and the results deviate from the Leveque solution when axial conduction is turned on. In both plots, Pe changes from 0.1 to 26. For the single-element design, fitting a linear curve to the data gives $Nu = 0.709Pe^{1/3} + 0.474$ with $R = 0.022$ when axial diffusion is turned on. When axial diffusion is turned off, a linear curve fitting results in $Nu = 0.792Pe^{1/3} - 0.003$ with $R = 0.002$ which is very close to the Leveque solution $Nu_{lev} = 0.807Pe^{1/3}$. Fitting linear curves to results of the guard-heated design results in $Nu = 0.389Pe^{1/3} + 0.0129$ with $R = 0.016$ when axial diffusion is turned on and $Nu = 0.389Pe^{1/3} - 0.000$ with $R = 10^{-5}$ when axial diffusion is turned off. Thus, the guard-heated design is not affected by axial diffusion even at low Pe values, which confirms the fact that the lower limit on the sensor length of Equation 3.40 vanishes by using an in-plane guard-heater, as desired.

Heat Transfer Rates

We wish to see how the direct, indirect and total heat transfer rates of the sensors change with shear, how they compare to the Leveque solution, and what are the effects of guard-heating. Plotting the heat transfer rates separately allows us to see how much the signal is affected by the substrate conduction and compare the amount of direct and indirect heat transfers between different designs and between water and air flows.

Figures 4.8-4.10 show how Nu_F, Nu_S and Nu_{signal} with Pe in each sensor design. Recall that Nu_F is the rate of heat that goes directly from the sensor to the fluid and Nu_S is the rate of heat that goes to the solid substrate and eventually goes to the fluid, thus it is referred to as the indirect heat transfer rate. The sum of Nu_F and Nu_S is the total rate of heat leaving the sensor element alone, which is equal to the total rate of heat being generated in the sensor, and gives us the signal $(Nu_F + Nu_S)$. Ideally, we would like Nu_S to be zero.

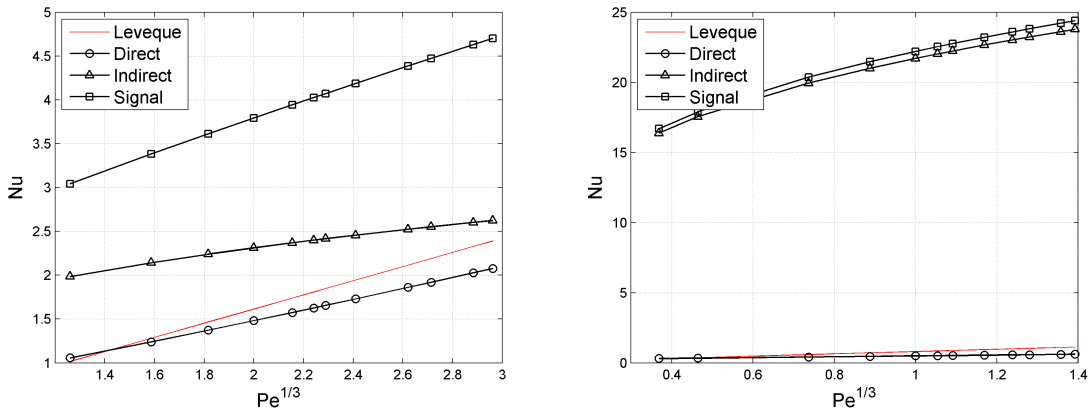

(a) Water (b) Air

Figure 4.8: Direct (Nu_F), indirect (Nu_S) and signal (Nu_{signal}) heat transfer rates vs. $Pe^{1/3}$ for the single-element (SE) sensor. The indirect heat tranfer is significantly higher than the direct heat transfer and dominates the signal in the air-glass combination. In water-glass, indirect heat transfer rate is not as high as air-glass but is still higher than direct heat transfer rate and dominates the signal.

The results show that in the single-element design the indirect heat transfer is significant. In both air and water, Nu_F is less than the Leveque solution, because of the preheating of the fluid by the substrate and thus less temperature difference between the fluid and the hot-film. In water, Nu_S is more than Nu_F but it has a

smaller slope and it might become less than Nu_F at higher Pe values. However, the total heat transfer rate will still be higher than Nu_F because of the substrate, which means loss of spatial resolution. In air the signal is dominated by the undesirable heat transfer Nu_S. Nu_S and consequently Nu_{signal} is more than 20 times bigger than Nu_F. This shows the single-element sensor performs very poorly in air. The more the signal is dominated by the indirect heat transfer, the more the dynamic behaviour of the sensor is limited by the substrate. Additionally, the loss of spatial resolution will be significant. Thus by looking just at the steady results we can conclude that the single-element sensor is too far from being acceptable for measurements in air.

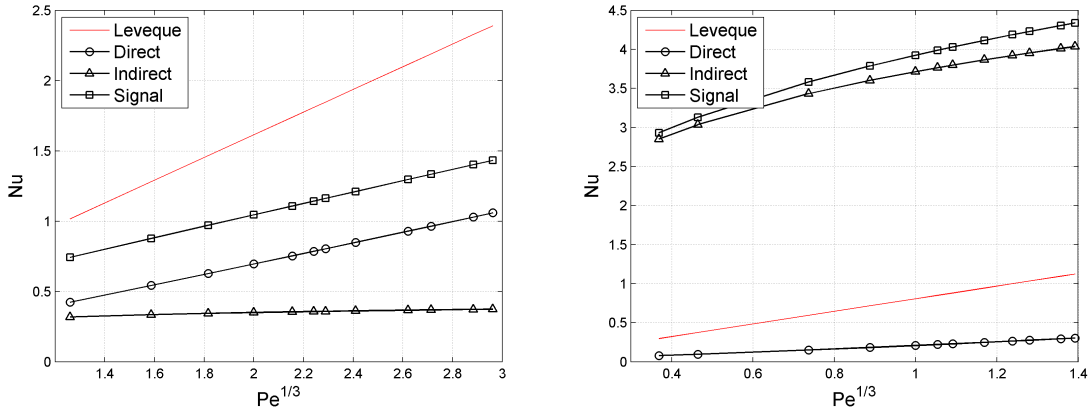

(a) Water (b) Air

Figure 4.9: Direct (Nu_F), indirect (Nu_S) and signal (Nu_{signal}) heat transfer rates vs. $Pe^{1/3}$ for the single-plane guard-heated ($GH1P$) sensor design. In water-glass, indirect heat transfer is comparable to direct heat transfer but does not change greatly with Pe. In air-glass, indirect heat transfer dominates the signal.

Results for the single-plane guard-heated sensor show some improvements over the single-element design regarding the amount of indirect heat transfer. In water, Nu_S changes weakly with Pe and its magnitude is smaller compared to the single-element sensor. It is also smaller in air but still changes strongly with Pe. In both water and air, Nu_F has become smaller than the single-element sensor because of the guard-heating, thus further reducing of the temperature difference between the fluid and the hot-film. Because both Nu_S and Nu_F become smaller, the signal of the guard-heated design is weaker than that of the single-element sensor, in which the unwanted indirect heat transfer rate Nu_S contributes substantial error to the the measured value.

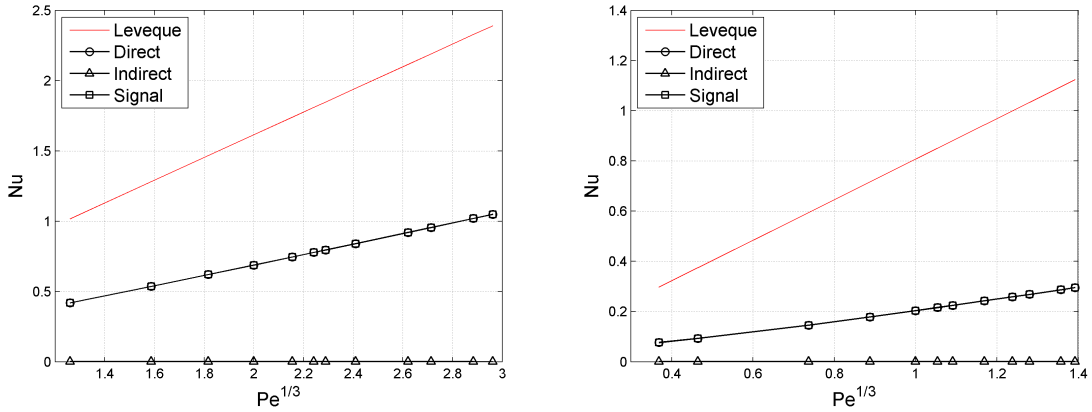

(a) Water (b) Air

Figure 4.10: Direct (Nu_F), indirect (Nu_S) and signal (Nu_{signal}) heat transfer rates vs. $Pe^{1/3}$ for the two-plane guard-heated ($GH2P$) sensor design. In both cases indirect heat transfer rate is zero and the signal only depends on the direct heat transfer rate.

The two-plane guard-heated sensor shows the most promising results. Adding the second guard-heated completely blocks any heat from the sensor going to the substrate. In both water and air Nu_S is zero (the values were as small as machine error in the numerical results). As a result the signal is purely due to direct heat transfer Nu_F, which was our goal for using guard-heaters.

The results so far have shown that the guard-heated designs decrease the amount of indirect heat transfer but at the cost of having weaker signal. The two-plane guard-heated design manages to completely eliminate the undesirable portion of the signal by ensuring zero indirect heat transfer. In the next sections, we will compare the signal strength, sensitivity and quality as well as equivalent length of the designs. First, we if the weaker signal of the guard-heated designs causes problems in data acquisition in terms of strength and sensitivity. Second, we compare the quality of the signals of the different designs and finally, we compare the amount of spatial averaging of each sensor.

Signal Strength and Sensitivity

The preheating done by the in-plane guard-heater results in lower temperature difference between the sensor and the fluid and thus weaker signal. There is a trade-off between getting a *better* signal (a signal with higher quality) and having a stronger signal. A weaker signal is not problematic unless the signal-to-noise ratio becomes

unacceptably low. Higher over-temperature, larger sensor or smaller guard-heater can be considered if the signal becomes too weak. On the other hand, it is a much more difficult task to do corrections to a strong signal with low quality.

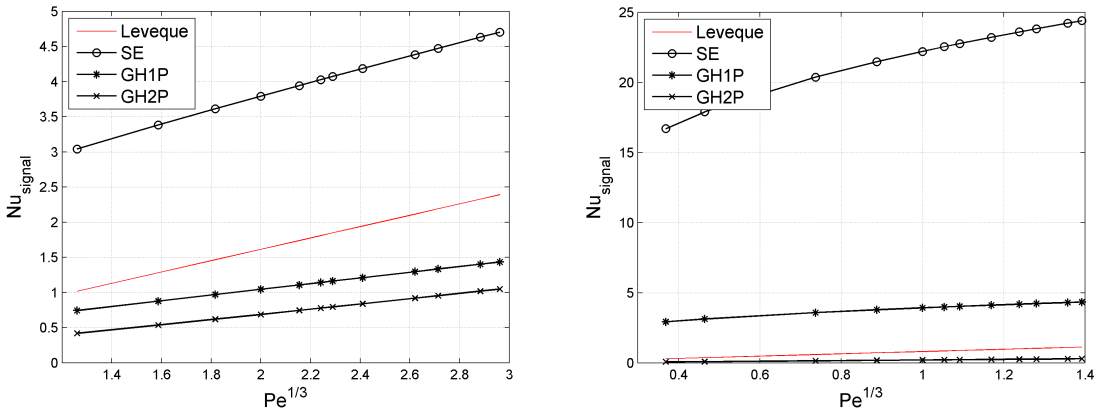

(a) Water (b) Air

Figure 4.11: Signal heat transfer rate (Nu_{signal}) vs. $Pe^{1/3}$ for different sensor designs. Nu_{signal} is much higher in the SE design, because it is dominated by indirect heat transfer.

We can calculate the power being generated in the sensors, which is equal to the rate of heat leaving the sensor (Equation 3.64).

$$I^2R = (Wk_f\Delta T)Nu_{signal}. \tag{4.6}$$

Assuming an over-temperature of $\Delta T = 40K$, if we multiply Nu_{signal} by $(Wk_f\Delta T)$ and re-plot Figure 4.11 we get Figure 4.12. The value of I^2R for the two-plane design in air is $0.021mW$ for $Pe = 1.17$ and $0.028mW$ for $Pe = 2.7$. We can use a higher over-temperature to increase the signal strength. For over-temperature of $\Delta T = 100K$, the above-mentioned values of I^2R will be multiplied by 2.5. A 12-bit A/D board has a resolution of $2.4mV$ in the $0 - 10V$ range, and a 16-bit data acquisition board has a resolution of $0.15mV$. For a typical sensor resistance of 10Ω, this resolution in voltage translates to resolution of $2.25 \times 10^{-5}mW$, which is 1000 times smaller than the value of I^2R for $Pe = 1.17$.

Fitting a linear curve to the $Nu_{signal} - Pe$ plot for the two-plane guard-heated sensor with air flow yields the relation $Nu = 0.216Pe^{1/3} - 0.008$. The constant -0.008 is very small, because of zero substrate conduction and low axial diffusion. If we neglect this constant and assume $Nu = 0.216Pe^{1/3}$, we can calculate the sensitivity

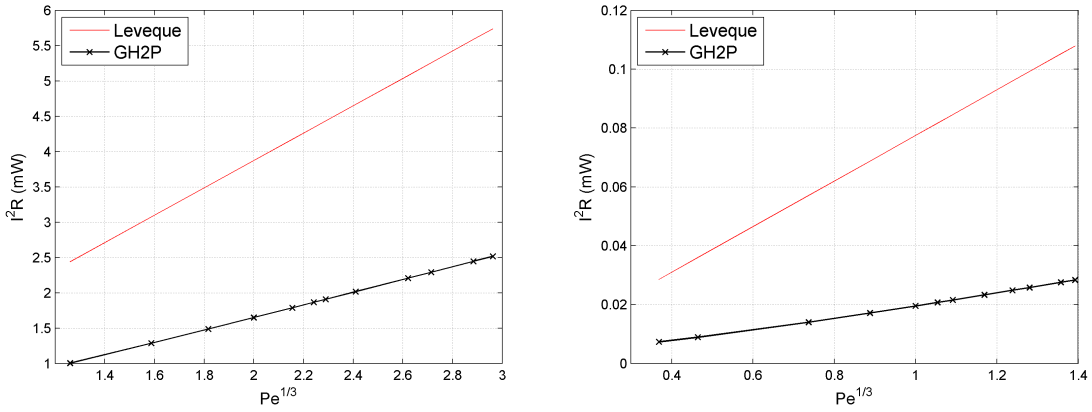

(a) Water (b) Air

Figure 4.12: Signal power (I^2R) in mW vs. $Pe^{1/3}$ for the two-plane guard-heated sensor and Leveque solution, assuming over-temperature of $40K$ and sensor size of $10\mu m \times 40\mu m$.

of the signal using

$$\Delta E = \Delta Pe \frac{dE}{dPe}, \tag{4.7}$$

which says for a change of ΔPe in Pe, E changes with ΔE. Recalling that $E^2 = RWk_f\Delta TNu$, and using $Nu = 0.216Pe^{1/3}$, we get $dE/dPe = 0.0015Pe^{-5/6}$. Thus, at $Pe = 1.17$, a voltage resolution of $\Delta E = 0.15mV$ corresponds to Pe resolution of $\Delta Pe = 0.11$, which means a fluctuation strength of about 10% in the shear stress. In practice, a gain of 10 can be used to amplify the signal before digitization by the A/D board, to obtain response to a 1% change in the shear stress, for these flow parameters.

A larger sensor can be used to increase the signal strength, which may, however, cause spatial averaging. For instance, using a sensor size of $100\mu m \times 400\mu m$ instead of $10\mu m \times 40\mu m$, results a Pe value of 100 times higher, and hence Nu_{signal} value of approximately $100^{1/3} = 4.64$ times higher. Thus, the heat generated in the sensor will become approximately 46.4 times bigger. In general, if the sensor length becomes n times bigger, the resulting heat generated in the sensor will become $n^{5/3}$ times bigger, if we assume Nu_{signal} changes linearly with $Pe^{1/3}$ between the initial Peclet number Pe_i, and n^2Pe_i.

Signal Quality

The quality of the signal, as defined in Chapter 3, shows how much of the signal is due to direct heat transfer. Comparing the signal quality of the sensor designs helps us understand how the single-element sensor performs and how much the guard-heated designs are able to help us to eliminate the indirect heat transfer rate from the sensor signal.

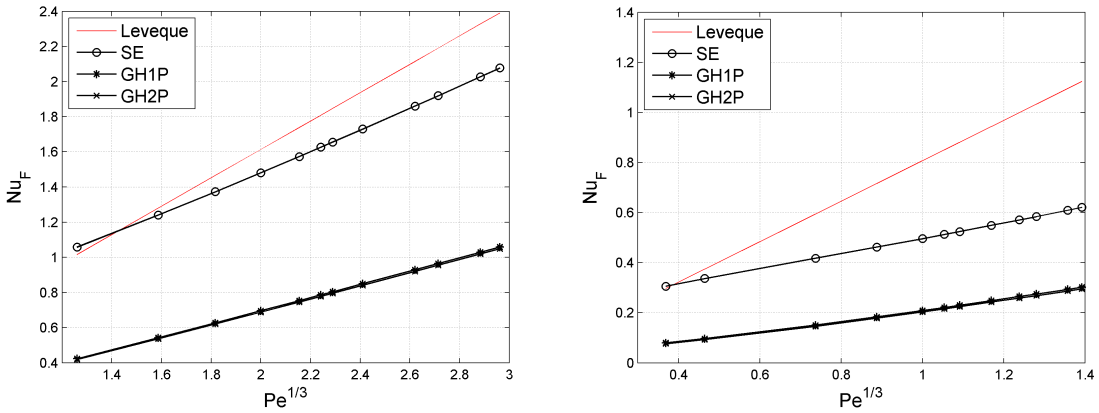

(a) Water (b) Air

Figure 4.13: Direct heat transfer rate (Nu_F) vs. $Pe^{1/3}$ for different sensor designs. For both guard-heated designs, direct heat transfer is lower than that of the single-element design and the Leveque solution because of the lower temperature difference between the sensor and the fluid.

Figure 4.13 helps us to compare Nu_F of the sensors. Nu_F in both single-element and guard-heated designs has values smaller than the Leveque solution. This can be attributed to the preheating of the fluid and the decrease in temperature difference between the hot-film and the fluid. Preheating is done by both the substrate and the guard-heater.

The signal quality of the sensors are compared in Figure 4.14. What can be immediately observed from the results is that the signal quality of the two-plane sensor remains equal to 1 for all values of Pe in both water and air. Thus the two-plane can completely eliminate the indirect heat transfer rate as predicted, making the sensor independent of the properties and dynamic behaviour of the substrate. The single-plane guard-heated design improves the quality compared to the single-element design, but fails to yield satisfactory results, especially in air. The results of the single-element sensor show the dominance of the indirect heat transfer in the signal. The

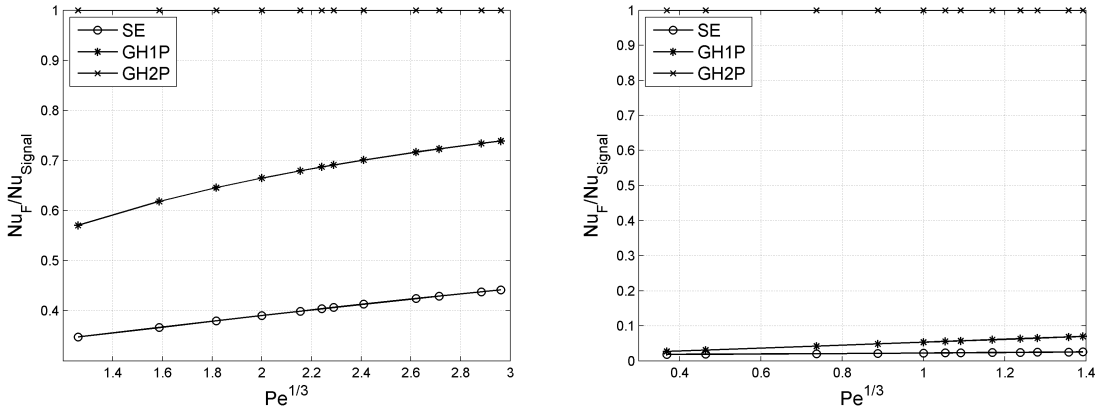

(a) Water (b) Air

Figure 4.14: Direct-to-signal heat transfer ratio vs. $Pe^{1/3}$ for different sensor designs. In the single-element design, only a small portion of the signal is due to direct heat transfer. The single-plane guard-heated design improves the quality of the signal by decreasing the indirect heat transfer. The two-plane guard-heated design completely eliminates the indirect heat transfer rate from the signal, and its signal is purely due to direct heat transfer to the fluid.

direct-to-total heat transfer ratio of less than 5% might explain why conventional single-element sensors have not been able to provide accurate WSS measurements in turbulent air flows. In the next section, we will compare the equivalent lengths of different sensors designs to see how their spatial resolution is affected by indirect heat transfer.

Equivalent Length

We recall that the equivalent length defined in Chapter 3 is a fair measure of the undesired heat exchange length of the fluid-substrate interface. Figure 4.15 shows how equivalent length based on total heat transfer rate changes with Pe for all three designs. For the single-element design, L_e/L is a strong function of Pe. In air L_e is more than 100 times bigger than L for the single-element design. In the guard-heated designs, however, L_e/L does not change significantly with Pe. It is especially significant that in the two-plane design, L_e/L remains constant. This confirms another advantage predicted in Chapter 3, for the guard-heated design, which is the elimination of the variable spatial resolution of the single-element sensors.

The value of L_e/L will not equal 1 even when there is no loss of spatial resolution,

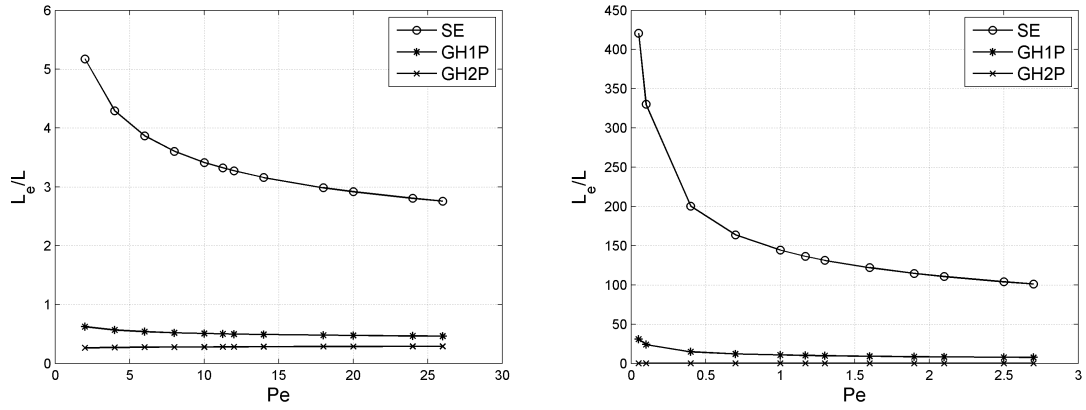

(a) Water (b) Air

Figure 4.15: The equivalent length L_{eq} vs. Pe for different designs. L_{eq} does not change with shear for the two-plane guard-heated design.

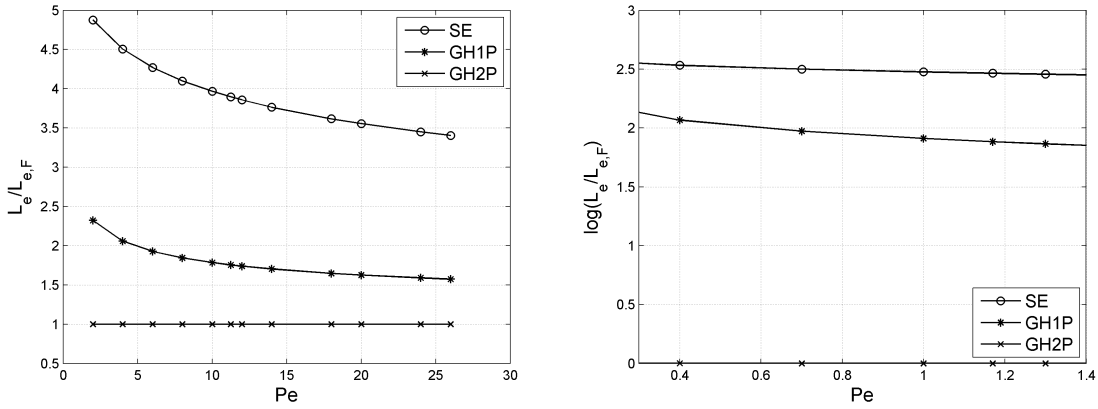

(a) Water (b) Air

Figure 4.16: The $L_e/L_{e,F}$ ratio is equal to 1 when the effective length of the sensor is equal to its physical length. When this ratio becomes larger than 1, the spatial resolution of the sensor decreases. The equivalent length of the two-plane guard-heated sensor does not change with shear rate because of zero indirect heat transfer. Thus the spatial resolution of this sensor is fixed and determined by its physical length.

because the heat transfer rate of the designs will not equal the heat transfer rate of the Leveque solution. Thus, it is better to either change the definition of L_e or scale it with a length other than L, so that it becomes equal to 1 when the spatial resolution does not change. We can scale L_e by $L_{e,F}$, the equivalent length based on

the direct heat transfer rate. When there is no indirect heat transfer and thus the spatial resolution of the sensor is fixed as its physical length, $L_e/L_{e,F}$ becomes equal to 1. $L_e/L_{e,F}$ plots are shown in Figure 4.16.

We remind the reader that we have chosen Peclet numbers appropriately to be different for air and water. This reflects real-world physically equivalent situations -such as the same range of Reynolds number for a turbulent pipe flow with the same diameter. This is more useful than taking the same range of Peclet number for both. If that was done, we would underestimate the spatial averaging problem for a conventional single-element sensor operating in air. Low Peclet number operation in air reduces the resolution of a single-element sensor by a factor of more than 100, and this problem is entirely eliminated by two-plane guard-heating.

4.2.3 Unsteady Results

The unsteady problem was solved using the *Time-dependent* solver, with the results of the steady runs as the initial condition. As described earlier, we used a sinusoidal shear rate with frequency ω and amplitude a to model a fluctuation in the velocity field. We set the average shear rate such that pipe Reynolds number would be $Re_D = 10^6$, which corresponds to $Pe = 11.26$ in water and $Pe = 1.17$ in air. The amplitude of the fluctuations was set equal to 0.1. The frequency ω was changed to cover all conditions of Table 3.1 for $\omega^* Pe^{-\frac{2}{3}}$. The total time T was set to cover two complete periods of fluctuations $T = 4\pi/\omega$. The time-step was $dt = T/100$, and both Nu_F and Nu_S were saved at each step.

At each frequency, the amplitude of the heat transfer rate fluctuations $A(\omega)$ were calculated and divided by the amplitude of low frequency fluctuations $A(0)$. The phase lag $\Delta\phi^\circ$ was calculated as the time difference between the peaks of the heat transfer rate and shear rate fluctuations, converted to degrees. One complete period of fluctuations was taken as 360° for reference.

Frequency Response

The signal response of the sensors in water and air are plotted against frequency ωHz in Figure 4.18. The frequency response of water-glass is reasonably acceptable, with attenuation starting to appear at $\omega \approx 1kHz$ for all three designs. The two-plane guard-heated designs shows slightly better response, followed by the single-plane guard-heated design and then the single-element. The response of air-glass

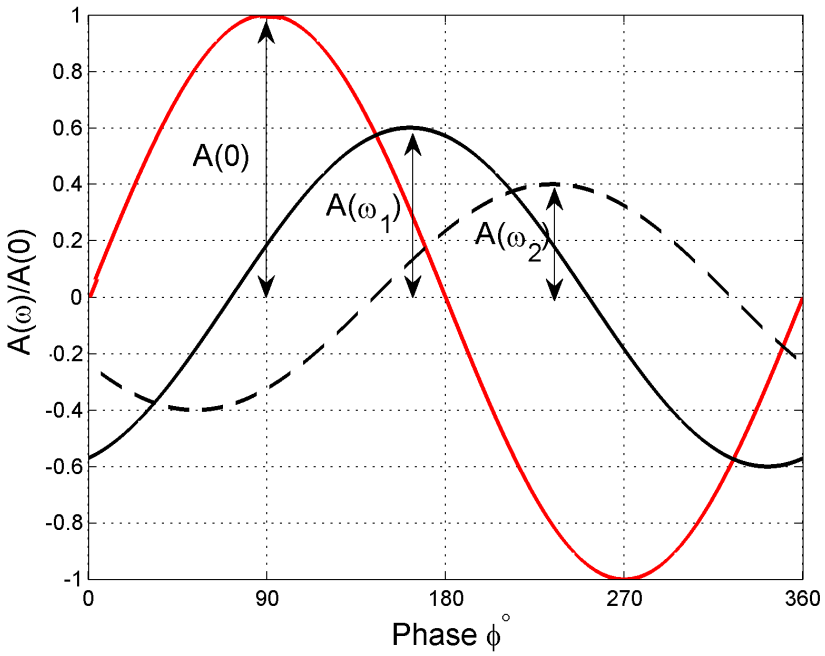

Figure 4.17: At high frequencies, direct, indirect and the signal heat transfer rates change with amplitude attenuation and phase lag relative to the quasi-steady heat transfer rates. The amplitude of the heat transfer rates at very low frequencies ($\omega \rightarrow 0$) are used as a reference to study the frequency response of the sensors.

however drops at very low frequencies, especially in the single-element and single-plane guard-heated designs. In both designs a significant attenuation of the signal amplitude happens when $\omega > 0.01z$. In the two-plane design, the signal response drops slightly at $\omega \approx 1Hz$, remaining higher than 0.8 up to $\omega \approx 10kHz$, after which it start to drop. At a high frequency of $\omega = 100kHz$ the response of the two-plane is about 0.5, whereas the response of the other designs is below 0.2.

The early drop in the frequency response of the single-element and single-plane guard-heated designs in air can be explained by the fact that their signals are dominated by substrate conduction and the energy equation in the substrate deviates from quasi-steady condition at a much lower frequency compared to air. To be able to use the results of our analysis from the previous chapter we plot the signal response of the sensors against $\omega^* Pe^{-\frac{2}{3}}$. These plots can be seen in Figure 4.19.

Recall that in our analysis we predicted that for the air-glass combination the response of the substrate drops if the conditions of $\omega^* Pe^{-\frac{2}{3}} \ll 10^{-5}$ is not met. Figure 4.19-b shows that in the single-element and single-plane guard-heated designs, where

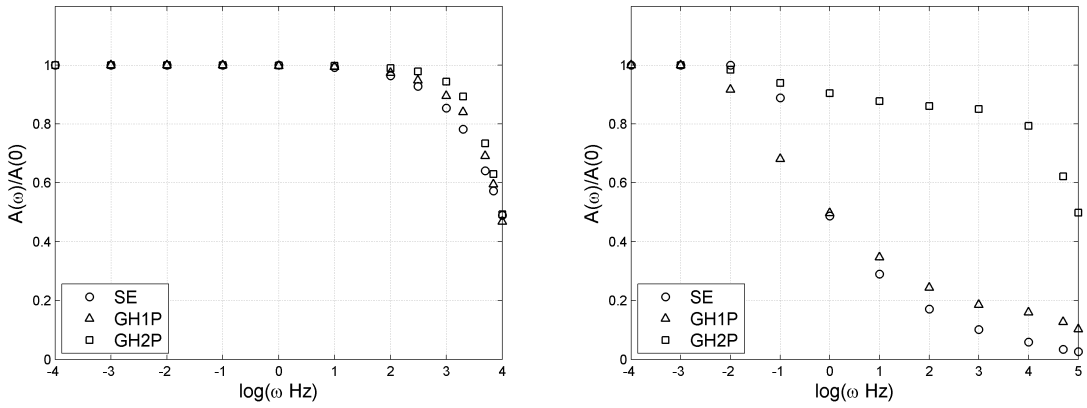

(a) Water (b) Air

Figure 4.18: Signal frequency response of different designs vs. ω. The GH2P design performs much better than the other two designs in air, since its signal only consists of Nu_F its signal response does not drop because of the substrate.

the signal is greatly dependent on the substrate, the response of the signal starts to drop at $\omega^* Pe^{-\frac{2}{3}} \approx 10^{-7}$. In contrast, the response of the signal for the two-plane design drops sharply when it reaches $\omega^* Pe^{-\frac{2}{3}} \approx 0.1$ which is the cut-off frequency of the fluid thermal boundary layer. In water-glass combination, we stated that the response of both direct and indirect heat transfers will drop if $\omega^* Pe^{-\frac{2}{3}}$ get close to 1. Figure 4.19-a shows that the signal response in water drops at $\omega^* Pe^{-\frac{2}{3}} \approx 0.1$ which agrees with our analysis. This drop is because the changes in shear rate become too fast for both fluid and the substrate.

Our results for frequency response of single-element hot-film sensors agree well with the results of Tardu *et al.* (2005), who showed that in the conventional hot-film sensors and in air-glass combination the response drops when $\omega^* \approx 10^{-6}$ at $Pe = 30$ [28]. This corresponds to $\omega^* Pe^{-\frac{2}{3}} \approx 10^{-7}$. They also showed that for water-glass the response drops at $\omega^* \approx 1$ which at $Pe = 30$ corresponds to $\omega^* Pe^{-\frac{2}{3}} \approx 0.1$. Our results for the guard-heated sensors, defined and investigated in this thesis, shows that the two-plane guard-heated sensor may be operated without substrate errors, up to the physical limits of frequency response imposed by the fluid thermal boundary layer.

We can plot the response of direct, indirect and signal heat transfers for each sensor to better understand their frequency response and compare them to the results of our analysis. Figures 4.20-4.22 show how for each sensor, the response of direct and indirect heat transfers change with frequency.

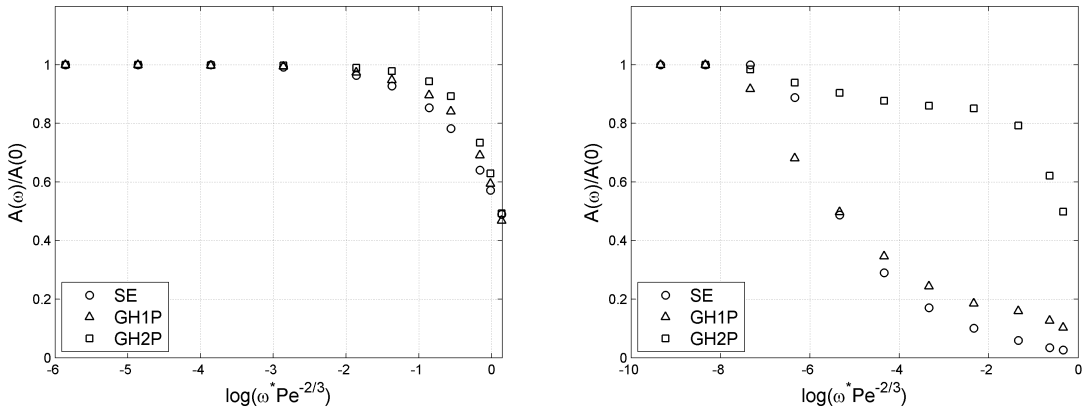

(a) Water (b) Air

Figure 4.19: Signal frequency response of different designs vs. $\omega^* Pe^{-\frac{2}{3}}$. The numerical results here can be compared to the results of our analysis in Chapter 3, which suggested that the response of the direct heat transfer drops when $\omega^* Pe^{-\frac{2}{3}} \approx 1$, and the response of the indirect heat transfer drops when $\omega^* Pe^{-\frac{2}{3}} \approx 1$ in water and $\omega^* Pe^{-\frac{2}{3}} \approx 10^{-5}$ in air. In air, the signal response of the SE and GH1P designs drop when $\omega^* Pe^{-\frac{2}{3}} \approx 10^{-7}$, since their signals are dominated by substrate conduction.

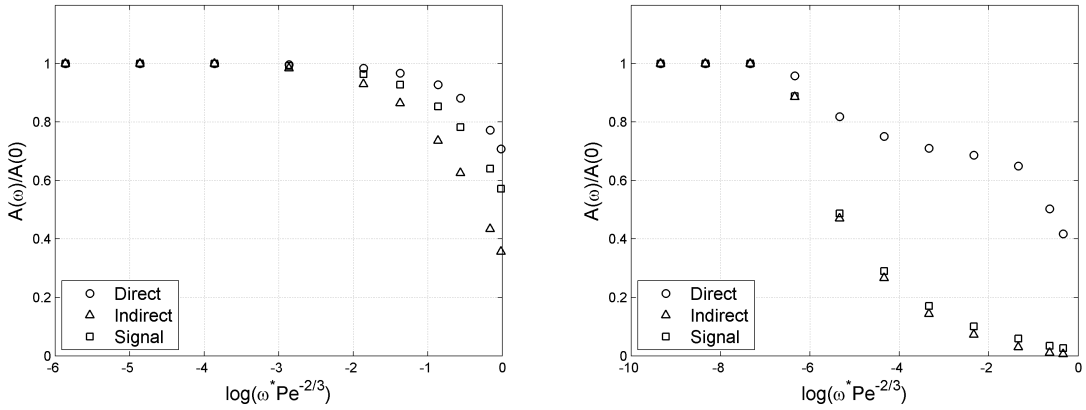

(a) Water (b) Air

Figure 4.20: Frequency response of the SE design vs. $\omega^* Pe^{-\frac{2}{3}}$. For water, response of both fluid and substrate, and hence the signal, drop at $\omega^* Pe^{-\frac{2}{3}} \approx 0.1$. For air, however, the substrate response drops at $\omega^* Pe^{-\frac{2}{3}} \approx 10^{-7}$ and the fluid response drops at $\omega^* Pe^{-\frac{2}{3}} \approx 0.1$. Since the signal is dominated by indirect heat transfer in the SE design, its response follows the response of the indirect heat transfer rate.

Figure 4.20-a shows that in the single-element design, the response of both water and substrate drop, and consequently the signal, at $\omega^* Pe^{-\frac{2}{3}} \approx 0.1$. The response of

the substrate however drops more rapidly. From Figure 4.20-b we can observe that the response of the substrate in the air-glass combination drops at $\omega^* Pe^{-\frac{2}{3}} \approx 10^{-7}$. The predictions we made in Chapter 3, using a choice of dimensionless parameters for the governing equations, regarding the response of the substrate, are seen, by these detailed numerical calculations, to be fairly accurate. In the single-plane guard-heated sensor the response of the indirect heat transfer rate drops more rapidly compared to the single-element sensor. However, since the single-plane guard-heated sensor has a better signal quality, its signal response is less dependent on the substrate and thus is better than that of the single-element. The indirect heat transfer rate of the two-plane guard-heated sensor is zero in both water and air, thus its signal frequency response is limited only by fluid thermal inertia.

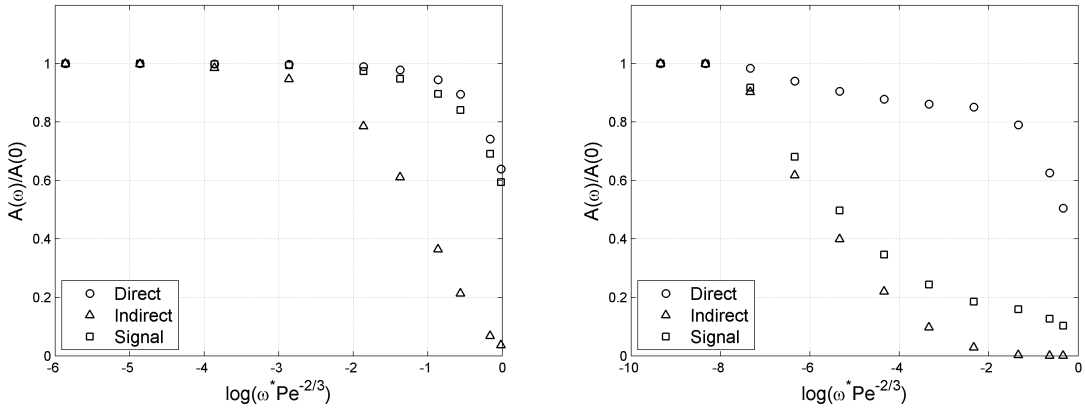

(a) Water (b) Air

Figure 4.21: Frequency response of the GH1P design vs. $\omega^* Pe^{-\frac{2}{3}}$. In water, the signal is dominated by direct heat transfer and its response follows that of the direct heat transfer rate. In air the indirect heat transfer is significant and the signal response is closer to the response of the indirect heat transfer rate, though not as much as the SE design.

An interesting and unpredicted result in the frequency response plots for air is the partial drop in the direct heat transfer response when the indirect heat transfer response drops. This phenomenon can be seen in both the single-element and the guard-heated results. Since at these frequencies the fluid energy equation is quasi-steady, the only plausible explanation for this partial drop is preheating of the fluid by the substrate. The in-plane guard-heater does additional preheating of the fluid, independent of shear rate and frequency, and thus reduces the effects of the substrate.

As a result both guard-heated sensors show less partial drop in the direct heat transfer response.

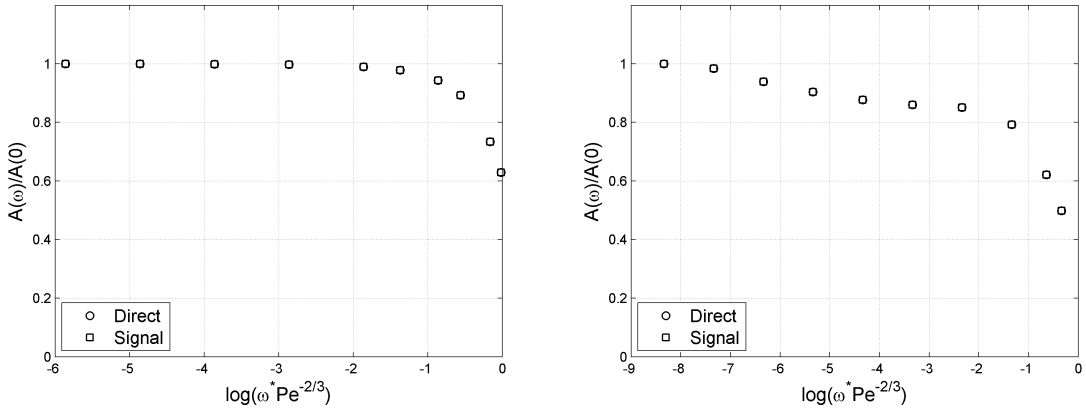

(a) Water (b) Air

Figure 4.22: Frequency response of the GH2P design vs. $\omega^* Pe^{-\frac{2}{3}}$. The signal response is the same as the direct heat transfer response, and the effects of substrate are removed. Thus the frequency of this design is only limited by the fluid thermal inertia.

Phase Lag

Another important quantity that should be studied is the phase lag between the WSS fluctuations and the sensor signal. Good frequency response alone does not guarantee accurate time-resolved measurements. If the sensor responds to some of the fluctuations in the flow -depending on their frequencies- with lag, then the measurements will suffer from phase distortion. Phase lag will introduce significant errors in multi-point WSS or WSS-velocity correlations necessary for proposing near-wall turbulence models or control schemes addressing turbulent boundary layer control. Frequency response plots must therefore be accompanied by phase lag plots to provide better information about the performance of the sensors at different frequencies and shear rates.

The phase lag between the WSS fluctuation and the sensor signal can be seen in Figure 4.23. Recall that $\Delta\phi$ is the phase lag in one cyclic variation of the shear rate. We can see from both plots that the signal of the two-plane guard-heated design remains in phase with WSS fluctuations until thermal inertia becomes significant at $\omega^* Pe^{-\frac{2}{3}} \approx 0.1$, a value up to which the sensor's signal response remains high. The

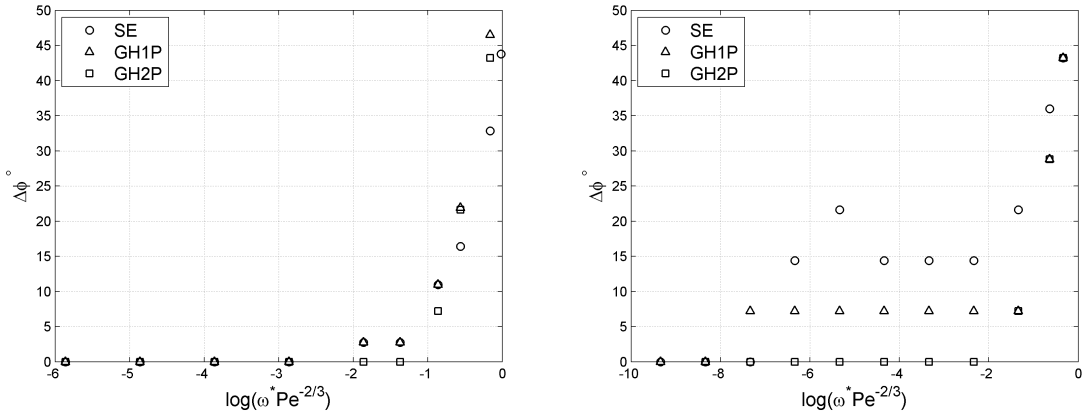

(a) Water (b) Air

Figure 4.23: Signal phase lag $\Delta\phi^\circ$ vs. $\omega^* Pe^{-\frac{2}{3}}$. The signal of the GH2P design does not suffer from phase lag until $\omega^* Pe^{-\frac{2}{3}}$ reaches close to 1. The other designs suffer from phase lag at low frequencies when the fluctuations become too fast for the substrate.

other two designs show acceptable results in water. However, in air the signal shows phase lag at $\omega^* Pe^{-\frac{2}{3}} = 10^{-7}$, where the fluctuations become too fast for the substrate. Figure 4.23-b also shows that the phase lag of the single-plane guard-heated design remains constant at about 7° between $\omega^* Pe^{-\frac{2}{3}} = 10^{-7}$ and $\omega^* Pe^{-\frac{2}{3}} = 0.1$, and then increases because of the fluid thermal inertia. The single-element design however shows complicated behaviour, once more proving the uncertainties and inaccuracies of the substrate in conventional hot-film sensors.

Similar to what we did for the frequency response results, we can plot the phase lag of the direct, indirect and signal heat transfer of the sensors separately. Figures 4.24, 4.25 and 4.26 show how the phase lag of Nu_F, Nu_S and Nu_{signal} changes with $\omega^* Pe^{-\frac{2}{3}}$.

In all plots, the phase lag of Nu_F starts at $\omega^* Pe^{-\frac{2}{3}} \approx 0.1$, which corresponds to the frequency at which the fluctuations become too fast for attenuation-free fluid heat transfer. The phase lag of Nu_S starts at about the same frequency as Nu_F for water, and at $\omega^* Pe^{-\frac{2}{3}} \approx 10^{-7}$ for air. Thus, as predicted it is the phase lag in the indirect heat transfer that causes phase lag in the signal.

Since the phase of the signal depends on the phase *and* amplitude of Nu_F and Nu_S, when plotted against $\omega^* Pe^{-\frac{2}{3}}$ it shows a complicated trend in air. The signal of the single-element and single-plane guard-heated sensors is dominated by indirect

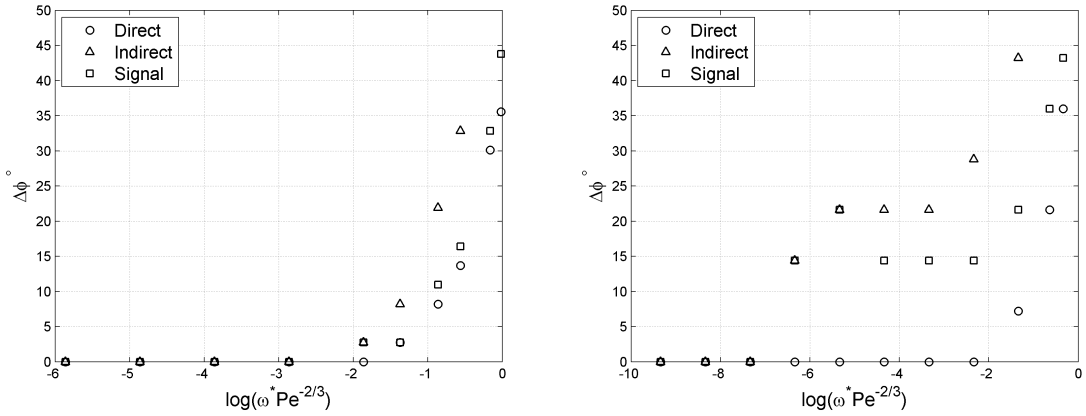

(a) Water (b) Air

Figure 4.24: Phase lag of the direct, indirect and total heat transfer rates for the SE design vs. $\omega^* Pe^{-\frac{2}{3}}$.

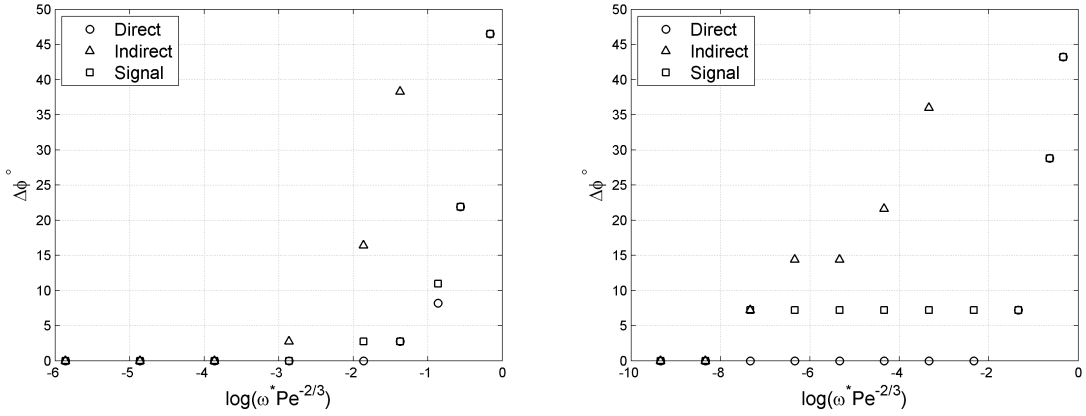

(a) Water (b) Air

Figure 4.25: Phase lag of the direct, indirect and total heat transfer rates for the GH1P design vs. $\omega^* Pe^{-\frac{2}{3}}$.

heat transfer and thus it is more in phase with Nu_S. When $\omega^* Pe^{-\frac{2}{3}}$ reaches at values close to $\omega^* Pe^{-\frac{2}{3}} \approx K_a = 10^{-5}$, amplitude attenuation and phase lag of Nu_S begins. When $\omega^* Pe^{-\frac{2}{3}} \approx 10^{-5}$ amplitude of the Nu_S variation is still bigger than Nu_F and the phase lag of the signal follows that of Nu_S. At higher frequencies, the amplitude of Nu_S variation becomes very damped and hence the signal becomes more in phase with Nu_F, which remain in phase with WSS until $\omega^* Pe^{-\frac{2}{3}}$ gets close to 1.

The two-plane guard-heated sensor has zero indirect heat transfer, thus its signal phase lag is exactly the same as Nu_F phase lag, which only starts to go up at

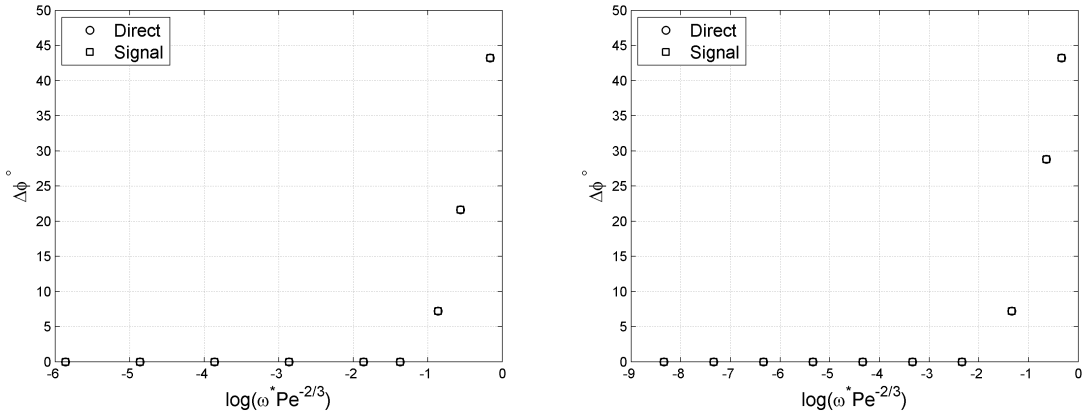

(a) Water (b) Air

Figure 4.26: Phase lag of the direct, indirect and total heat transfer rates for the GH2P design vs. $\omega^* Pe^{-\frac{2}{3}}$.

$\omega^* Pe^{-\frac{2}{3}} \approx 0.1$. The importance of zero phase lag becomes significant when corrections are to be done to the sensor signal. When the signal does not suffer from phase lag, the partial attenuation of the signal amplitude shown in Figure 4.22 can be corrected. The results for the two-plane guard-heated sensor show that it maintains a good frequency response and zero signal phase lag until the thermal inertia becomes significant, which is the theoretical limit of hot-film sensors.

4.3 Chapter Summary

In this chapter we numerically studied water and air flow over single-element and guard-heated sensors, based on the results of our analysis from Chapter 3. The performance of the different designs were compared regarding their signal quality (independence of signals from substrate conduction), spatial resolution, validity of calibration equation assumptions, frequency response and signal phase lag. The steady-state studies were done in a range of Peclet numbers corresponding to pipe Reynolds number of $Re_D = 5 \times 10^4$ to $Re_D = 5 \times 10^6$, assuming a pipe diameter of $D = 30cm$. The unsteady studies were done at $Re_D = 10^6$, resulting in low Peclet numbers of $Pe = 11.24$ in water and $Pe = 1.17$ in air.

We can summarize our findings from the numerical results as follows:

- The signal of the single-element hot-film sensor is dominated by unwanted indirect heat transfer (heat going indirectly to the fluid through the substrate).

In the case of air-glass combination, more than 90% of the signal of the single-element sensor is indirect heat transfer. Substrate conduction is responsible for significant deviation of the sensor signal from the analytically dervied calibration equation (Leveque solution). We found that the two-plane guard-heated sensor completely removes the indirect heat transfer from the signal. The results show that its signal is purely due to direct heat transfer from the sensor to the fluid.

- The effective length of the single-element sensor is much larger than its physical length, and changes with shear rate. For water, the equivalent length of the sensor (defined in Chapter 3 as a measure of the effective length of the sensor) is more than 3 times the physical length of the sensor, and for air this ratio is more than 300. This variable effective length results in variable spatial resolution for the single-element sensor. The two-plane guard-heated sensor ensures fixed spatial resolution over all shear rate values, by eliminating the indirect heat transfer.

- The guard-heated design removes the lower limit on the sensor size by removing the effects of axial heat conduction in the fluid on the heat transfer rates, making it possible for small-scale fabrication techniques to extend the limits of spatial resolutions, by making sensor elements as small as signal-to-noise ratio limits will allow.

- For conventional single-element hot-film sensors, the high frequency response which may be expected from the low thermal inertia (sub-micron thickness) of metal films is reduced by substrate heat transfer. The reduction is drastic in air. The signal response of the single-element sensor begins to drop at frequencies much lower (10^5 times) than the cut-off frequency due to thermal inertia of the fluid. The two-plane guard-heated design significantly enhances the frequency response by eliminating the substrate conduction from the sensor signal, and minimizing the effects of substrate on the signal response. For the studied case ($L = 10\mu m$, $Pe = 1.17$) the response of the single-element sensor drops at $\omega = 0.01Hz$, whereas the two-plane guard-heated sensor maintains high response up to $\omega = 10kHz$.

- The signal of the single-element sensor suffers from phase lag even at very low frequencies. The two-plane guard-heated sensor shows zero phase lag right up

to $10kHz$, where the thermal inertia of the fluid becomes significant. This is of great importance since it enables us to do to amplitude corrections and enables accurate multi-point WSS or simultaneous WSS-velocity measurements and correlations, which are impossible to obtain using single-element sensors, expect perhaps in impractically small ranges of flow parameters.

The two-plane guard-heated design proves to eliminate the most severe source of errors in hot-film sensors, which is substrate heat conduction. The promising results show that this new design will enable accurate WSS measurements in air with high spatial and temporal resolution, minimal amplitude attenuation and zero phase lag at high frequencies.

Chapter 5

Conclusions

This thesis provides a detailed analysis of hot-film sensors for wall shear stress measurements and examines a new design proposed to address several serious deficiencies of the conventional single-element hot-film sensor.

A large fraction of this thesis was dedicated to examining the substrate error reduction expected from guard-heated sensors. This required quantifying the several limits and design requirements of conventional single-element sensors. This was done by non-dimensionalizing the governing equations in the fluid, solid substrate and their interface and using available steady relations for turbulent flows. In an attempt to prepare a guideline for choosing a sensor to meet the design requirements, the dependency of the determining quantities on flow conditions and sensor size was provided. Analysis using the dimensionless parameters was then examined in a pipe flow, to help the reader use the analysis for a physical problem.

A numerical model was built to examine the statements made in the analysis, and to address the unanswered questions. The performance of single-plane and two-plane guard-heated designs were compared to the conventional single-element sensor. The numerical study consisted of two steps: 1) Steady-state analysis of the sensors to examine their signal characteristics and effective lengths, 2) Unsteady, time-dependent analysis to examine the dynamic behaviour of the sensors and quantify their frequency response and phase lag. Water-glass and air-glass combinations for fluid and substrate materials were studied since they provide different substrate-fluid conductivity ratios.

The two-plane guard-heated design demonstrated encouraging results in eliminating the errors and deficiencies of the conventional hot-film sensors, even at the very low Peclet numbers examined. This design proved to be able to completely block the indirect heat transfer to the fluid through the substrate, and thus remove the

severe effects of the substrate on the hot-film sensors such as variable spatial resolution, poor signal frequency response, spectral and phase distortion and other errors arising from invalidation of the calibration equation assumptions,. The single-plane guard-heated design was also studied since it is easier to fabricate and consumes less power compared to the two-plan sensor. Although it showed improvements in results compared to the single-element sensor, the results were far from satisfactory in air.

The encouraging results of the new, two-plane guard-heated design promise accurate wall shear stress measurements in air. By removing the lower limit on the sensor size and ensuring high signal frequency response and zero phase lag, this new design enables us to do point measurements with high temporal resolution and, hence, be able to achieve better understanding of turbulent flows, for instance by examining WSS-velocity correlations. The only disadvantage of guard-heating can be a weak signal, particularly in air, and at low Peclet numbers. Using a higher signal gain, an A/D board with flexible low voltage range, a larger sensor and higher over-temperature can be used to enhance the signal strength and resolution.

5.1 Recommendations for Future Work

The immediate recommendation is to fabricate the two-plane guard-heated design and test it in wind tunnel or pipe flow facility. A commercial CTA system can be used with the fabricated micro-sensor for WSS measurements. However, more detailed investigation can be done on hot-film sensors. The first recommendation is to extend the current two-dimensional model to a three-dimensional one. This would enable quantification of the effects of spanwise velocity and WSS fluctuations on the sensor signal, as well as the performance of two-component WSS sensors. Additionally, the WSS fluctuations in this thesis were confined to sinusoidal variations with a fixed amplitude. Large amplitude fluctuations and variable amplitude fluctuations can also be investigated. Another interesting recommendation is to model an array of hot-films, which can be useful for force distribution measurement or multi-point correlations. More accurate modelling of the substrate and boundary conditions and implementing natural convection into the model, are other areas that can be studied in future work.

Bibliography

[1] F. M. White. *Fluid Mechanics*. McGraw-Hill, 2009.

[2] J. Kim. Active control of turbulent boundary layers for drag reduction. In S. Biringen, H. Ors, A. Tezel, and J. H. Ferziger, editors, *Industrial and Environmental Applications of Direct and Large-Eddy Simulation*, volume 529 of *Lecture Notes in Physics*, pages 142–152. Springer Berlin Heidelberg, 1999.

[3] J. D. Swearingen and R. F. Blackwelder. The growth and breakdown of streamwise vortices in the presence of a wall. *Journal of Fluid Mechanics*, 182:255–290, 1987.

[4] N. Kasagi, Y. Suzuki, and K. Fukagata. Microelectromechanical systemsbased feedback control of turbulence for skin friction reduction. *Annual Review of Fluid Mechanics*, 41:231–251, 2009.

[5] U. Piomelli. Wall-layer models for large-eddy simulations. *Progress in Aerospace Sciences*, 44:437–446, 2008.

[6] U. Piomelli and E. Balaras. Wall-layer models for large-eddy simulations. *Annual Review of Fluid Mechanics*, 34:349–374, 2002.

[7] H. Choi, P. Moin, and J. Kim. Active turbulence control for drag reduction in wall-bounded flows. *Journal of Fluid Mechanics*, 262:75–110, 1994.

[8] B. Honglei. *Wall Shear Stress Sensing, Friction Drag Reduction, And The Wake of Two Staggered Cylinders*. PhD thesis, The Hong Kong Polytechnic University, 2011.

[9] L. Lofdahl and M. Gad-el-Hak. MEMS-based pressure and shear stress sensors for turbulent flows. *Measurement Science and Technology*, 10:665–686, 1999.

[10] M. Gad-el-Hak. *Flow Control: Passive, Active, and Reactive Flow Management*. Cambridge University Press, 2007.

[11] T. Yamagami, Y. Suzuki, and N. Kasagi. Development of feedback control system of wall turbulence using MEMS devices. In *Proc. 6th Symp. Smart Control of Turbulence*, pages 135–141, 2005.

[12] L. Lofdahl and M. Gad-el-Hak. MEMS applications in turbulence and flow control. *Progress in Aerospace Sciences*, 35:101–203, 1999.

[13] J. W. Naughton and M. Sheplak. Modern developments in shear-stress measurement. *Progress in Aerospace Sciences*, 38:515–570, 2002.

[14] M. A. Schmidt, R. T. Howe, S. D. Senturia, and J. H. Haritonidis. Design and calibration of a microfabricated floating-element shear-stress sensor. *IEEE Transactions on Electron Devices*, 35:750–757, 1988.

[15] H. Lv, C. Jiang, Z. Xiang, B. Ma, J. Deng, and W. Yuan. Design of a micro floating element shear stress sensor. *Flow Measurement and Instrumentation*, 30:66–74, 2013.

[16] S. Grosse and W. Schroder. Wall-shear stress patterns of coherent structures in turbulent duct flow. *Journal of Fluid Mechanics*, 633:147, 2009.

[17] U. K. Ayaz. Wall shear stress sensor based on the optical resonances of dielectric microspheres. *Measurement Science and Technology*, 22:075203, 2011.

[18] J. E. Mitchell and T. J. Hanratty. A study of turbulence at a wall using an electrochemical wall shear-stress meter. *Journal of Fluid Mechanics*, 26:199–221, 1966.

[19] Q. Lin, F. Jiang, X. Wang, Y. Xu, Z. Han, Y. Tai, J. Lew, and C. Ho. Experiments and simulations of MEMS thermal sensors for wall shear-stress measurements in aerodynamic control applications. *Journal of Micromechanics and Microengineering*, 14:1640–1649, 2004.

[20] A. N. Menendez and B. R. Ramaprian. The use of flush-mounted hot-film gauges to measure skin friction in unsteady boundary layers. *Journal of Fluid Mechanics*, 161:139–159, 1985.

[21] B. J. Bellhouse and D. L. Schultz. Determination of mean and dynamic skin friction, separation and transition in low-speed flow with a thin-film heated element. *Journal of Fluid Mechanics*, 24:379–400, 1966.

[22] L.M. Fingerson and P. Freymuth. *Fluid Mechanics Measurements*, chapter Thermal Anemometers. Taylor & Francis, Washington, DC, 1996.

[23] J. H. Haritonidis. *The Measurement of Wall Shear Stress*, page 229. Advances in Fluid Mechanics Measurements. Springer-Verlag, 1989.

[24] B. J. Bellhouse and D. L. Schultz. Determination of mean and dynamic skin friction, separation and transition in low-speed flow with a thin-film heated element. *Journal of Fluid Mechanics*, 24:379, 1966.

[25] A. Lévêque. *Les Lois de la transmission de chaleur par convection*. Dunod, 1928.

[26] H. Ludwieg. *Instrument for Measuring the Wall Shearing Stress of Turbulent Boundary Layers*. National Advisory Committee for Aeronautics, Washington, DC, 1950.

[27] D. Meunier, S. Tardu, D. Tsamados, and J. Boussey. Realization and simulation of wall shear stress integrated sensors. *Microelectronics Journal*, 34:1129–1136, 2003.

[28] F. S. Tardu and C. T. Pham. Response of wall hot-film gages with longitudinal diffusion and heat conduction to the substrate. *Journal of Heat Transfer-Transactions of the ASME*, 127:812–819, 2005.

[29] C. O. Ajagu, P. A. Libby, and J. C. LaRue. Modified gauge for time-resolved skin-friction measurements. *Review of Scientific Instruments*, 53:1920–1926, 1982.

[30] P. H. Alfredsson, A. V. Johansson, J. H. Haritonidis, and H. Eckelmann. The fluctuating wall-shear stress and the velocity field in the viscous sublayer. *Physics of Fluids*, 31:1026, 1988.

[31] C. Liu, J.-B. Huang, Z. Zhu, F. Jiang, S. Tung, Y.-C. Tai, and C.-M. Ho. A micromachined flow shear-stress sensor based on thermal transfer principles. *Journal of Microelectromechanical Systems*, 8:90–99, 1999.

[32] J. B. Huang, C. M. Ho, S. Tung, C. Liu, and Y. C. Tai. Micro thermal shear stress sensor with and without cavity underneath. In *Instrumentation and Measurement Technology Conference, Proceedings. 'Integrating Intelligent Instrumentation and Control'.*, page 171. IEEE, 1995.

[33] L. Lofdahl, V. Chernoray, S. Haasl, G. Stemme, and M. Sen. Characteristics of a hot-wire microsensor for time-dependent wall shear stress measurements. *Experiments in Fluids*, 35:240–251, 2003.

[34] B. C. Khoo, Y. T. Chew, C. P. Lim, and C. J. Teo. Dynamic response of a hot-wire anemometer. part I: A marginally elevated hot-wire probe for near-wall velocity measurements. *Measurement Science and Technology*, 9:751, 1998.

[35] D. Sturzebecher, S. Anders, and W. Nitsche. The surface hot wire as a means of measuring mean and fluctuating wall shear stress. *Experiments in Fluids*, 31:294–301, 2001.

[36] M. Aoyagi, N. Takehana, S. Masuda, and I. Ariga. Improvement of hot film surface gage for wall shear stress measurement. In *Proceedings of the International Symposium FLUCOME*, volume 2 of *Fluid Control and Measurement*, page 863, 1985.

[37] R. B. Bhiladvala. Guard-heated thermal sensor for turbulent wall-shear stress fluctuations. In *The 20th International Symposium on Transport Phenomena*, Victoria, BC, 2009.

[38] T. Hanratty and J. Campbell. *Fluid Mechanics Measurements*, chapter Measurement of Wall Shear Stress. Taylor & Francis, Washington, DC, 1996.

[39] S. C. Ling. Heat transfer from a small isothermal spanwise strip on an insulated boundary. *Journal of Heat Transfer-Transactions of the ASME*, 85:230–236, 1963.

[40] P. H. Alfredsson, A. V. Johansson, J. H. Haritonidis, and H. Eckelmann. The fluctuating wall-shear stress and the velocity field in the viscous sublayer. *Physics of Fluids*, 31:1026, 1988.

[41] B. J. Bellhouse and D. L. Schultz. The measurement of fluctuating skin friction in air with heated thin-film gauges. *Journal of Fluid Mechanics*, 32:675–680, 1968.

[42] L. Pera and B. Gebhart. Natural convection boundary layer flow over horizontal and slightly inclined surfaces. *International Journal of Heat and Mass Transfer*, 16:1131 – 1146, 1973.

[43] S. E. Haaland. Simple and explicit formulas for the friction factor in turbulent pipe flow. *Journal of Fluids Engineering-Transactions of the ASME*, 105, 1983.

Appendix A

Leveque Solution Derivation

The energy equation for incompressible, constant properties fluid flow is

$$\frac{\partial \theta}{\partial t} + u\frac{\partial \theta}{\partial x} + v\frac{\partial \theta}{\partial y} + w\frac{\partial \theta}{\partial z} = \alpha_f \left[\frac{\partial^2 \theta}{\partial x^2} + \frac{\partial^2 \theta}{\partial y^2} + \frac{\partial^2 \theta}{\partial z^2}\right], \tag{A.1}$$

where θ is the dimensionless temperature $(T_h - T)/(T_h - T_f)$ with T_h and T_f begin the hot-film and ambient fluid temperatures, respectively. α_f is the thermal diffusivity of the fluid.

If the thermal boundary layer is contained within the viscous sublayer, in which $\overline{u}$ is know to vary linearly with y, and $u^{'}$ is also assumed to do so, we may define axial velocity gradient $s_x = \overline{s}_x + s_x^{'}$, through $\overline{u} = \overline{s}_x y$ and $u^{'} = s_x^{'} y$. If the heat transport due to all processes, expect for axial convection and wall-normal diffusion, can be neglected, the energy equation reduces to

$$\frac{\partial \theta}{\partial t} + s_x y\frac{\partial \theta}{\partial x} = \alpha_f \frac{\partial^2 \theta}{\partial y^2}. \tag{A.2}$$

If we assume the fluctuations are slow enough that the time it takes for them to pass the length of the hot-film is greater than the time it takes for heat to diffuse across the thickness of the thermal boundary layer, the time derivative term may be ignored. Hence we can describe the problem as

$$s_x y\frac{\partial \theta}{\partial x} = \alpha_f \frac{\partial^2 \theta}{\partial y^2}, \tag{A.3}$$

with the following boundary conditions

$$\theta(0, y) = 1, \quad \theta(x, \infty) = 1, \quad \text{and} \quad \theta(x, 0) = 0. \tag{A.4}$$

While the time derivative is negligible, s_x is time-dependent and the problem is referred to as quasi-steady.

Introducing the similarity variable $\eta = y(s_x/9\alpha_f x)^{1/3}$, we obtain the ordinary differential equation

$$\frac{\partial^2\theta}{\partial\eta^2} + 3\eta^2\frac{\partial\theta}{\partial\eta} = 0, \tag{A.5}$$

with the boundary conditions

$$\theta(\infty) = 1, \quad \text{and} \quad \theta(0) = 0. \tag{A.6}$$

The solution to this ODE is

$$\theta(\eta) = \frac{\int_0^\eta e^{-r^3}dr}{\int_0^\infty e^{-r^3}dr} = \frac{1}{\Gamma\left(\frac{4}{3}\right)}\int_0^\eta e^{-r^3}dr. \tag{A.7}$$

The integrals are evaluated numerically. Only the gradient $(\partial\theta/\partial\eta)_{\eta=0}$ is needed to evaluate the heat transfer rate

$$\begin{aligned} Q &= \int_0^L k_f \left(\frac{\partial T}{\partial y}\right)_{y=0} W dx \\ &= (T_f - T_h)k_f W \left(\frac{\partial\theta}{\partial y}\right)_{y=0}\int_0^L \left(\frac{s_x}{9\alpha_f x}\right)^{1/3} dx \\ &= (T_f - T_h)k_f W C_1 \left(\frac{s_x}{\alpha_f}\right)^{1/3} L^{2/3}. \end{aligned} \tag{A.8}$$

k_f is the thermal conductivity of the fluid and $C_1 = 0.807$ accounts for the constants from the integration and the θ derivative from the integral for $\theta(\eta)$.

Since $Q = hLW(T_f - T_h)$, where h is the convective heat transfer coefficient, the Nusselt number $Nu = hL/k_f$ is

$$Nu = 0.807 Pe^{\frac{1}{3}}. \tag{A.9}$$

where $Pe = s_x L^2/\alpha_f$ is the Peclet number.

Appendix B

Calculations

The pipe Reynolds number is defined as

$$Re_D = \frac{UD}{\nu}, \tag{B.1}$$

where U is the average pipe velocity, D is the pipe diameter and ν is the fluid viscosity. To find the relation between $\overline{s}_x$ and Re_D, we will first use the Haaland [43] equation for smooth pipes to find out the equation relating the Fanning friction factor and Re_D

$$f = \frac{1}{4}\left[-1.8\log\left(\frac{6.9}{Re_D}\right)\right]^{-2}. \tag{B.2}$$

From the definition of the Fanning friction factor we have

$$f = \frac{\overline{\tau}_w}{\frac{1}{2}\rho U^2}, \tag{B.3}$$

where $\overline{\tau}_w$ is the average wall shear stress. Knowing $\overline{\tau}_w = \mu\overline{s}_x$ we can write

$$\overline{s}_x = \frac{U^2}{\nu}\frac{f}{2}. \tag{B.4}$$

We can combine Equation B.2 with Equation B.4 to find the relation between $\overline{s}_x$ and Re_D

$$\overline{s}_x = \frac{1}{2\sqrt{2}}\frac{\nu}{D^2}Re_D^2\left[-1.8\log\left(\frac{6.9}{Re_D}\right)\right]^{-1}. \tag{B.5}$$

We can plot Re_D vs. $\overline{s}_x$ using the above relation for water and air and a constant pipe diameter. Fitting a curve to these plots show that $\overline{s}_x$ changes with $Re_D^{1/9}$ in the

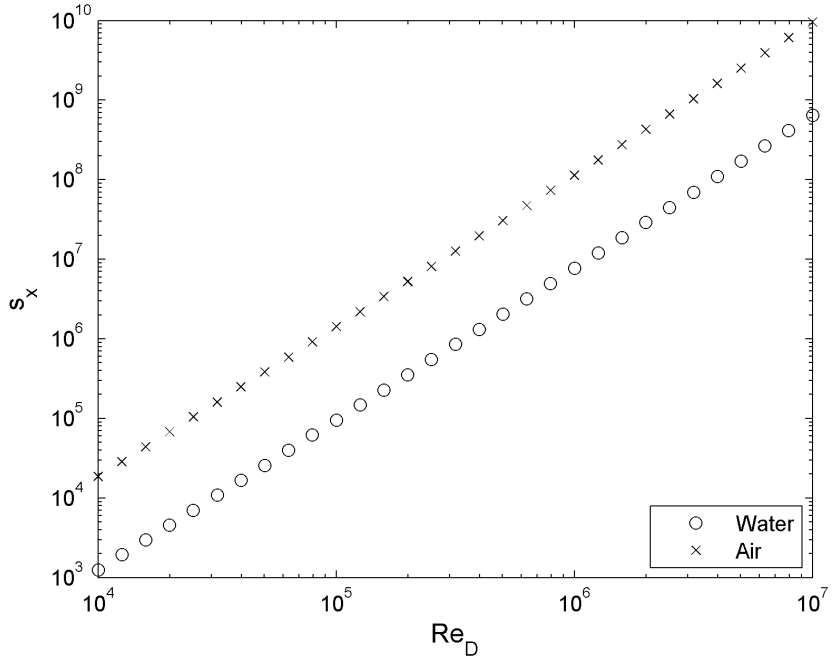

Figure B.1: $\overline{s}_x$ vs Re_D for both water and air. $\overline{s}_x$ changes with $Re_D^{1/9}$ in the range plotted.

range of $Re_D = 10^4 - 10^7$. Once $\overline{s}_x$ is found for a given Re_D, Peclet number can be calculated as $Pe = \overline{s}_x L^2/\alpha_F$.

One viscous wall unit or viscous length scale is ν/u_τ. Using the definition of friction velocity $u_\tau = \sqrt{\overline{\tau}_w}$ we can write

$$\frac{u_\tau}{\nu} = \frac{U}{\nu}\sqrt{\frac{f}{2}}. \tag{B.6}$$

We can thus find the viscous length scale for a given fluid properties and Re_D to scale the sensor length L or frequency ω and get L^+ and ω^+.

Appendix C

Additional Results

C.1 Guard-Heated Design

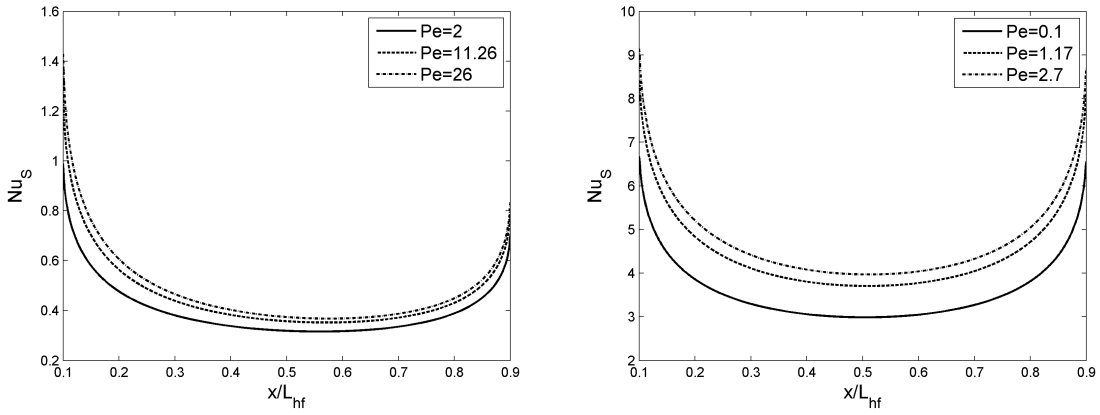

(a) Water (b) Air

Figure C.1: The indirect heat transfer rate Nu_S of single-plane guard-heated sensor vs. sensor position within the guard-heater. Nu_S is minimum near the center of the guard-heater and does not change greatly by moving the center of the sensor within 0.4 and 0.6 of the guard-heater length. The distribution is more symmetrical for air, because of the lower Pe.

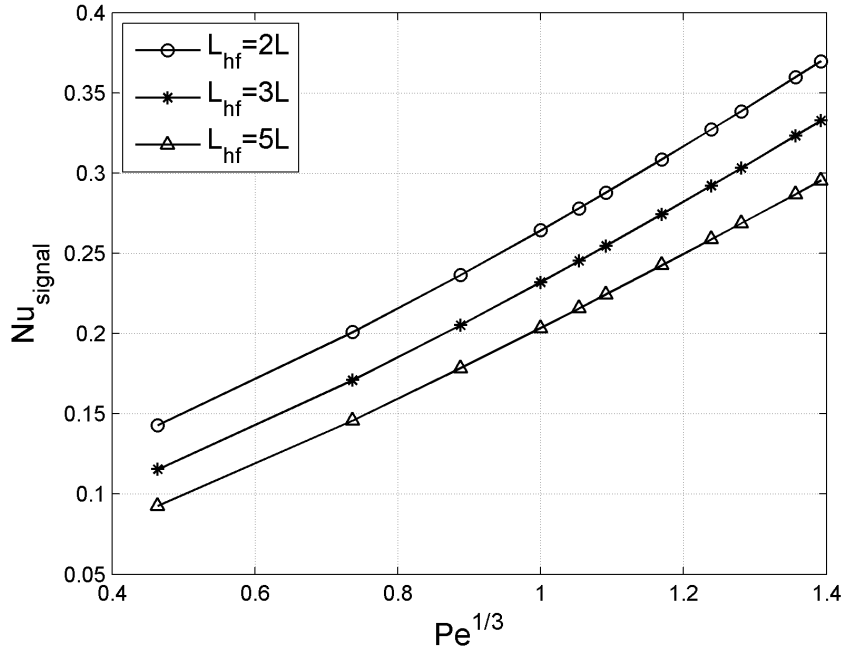

(a) Signal Strength

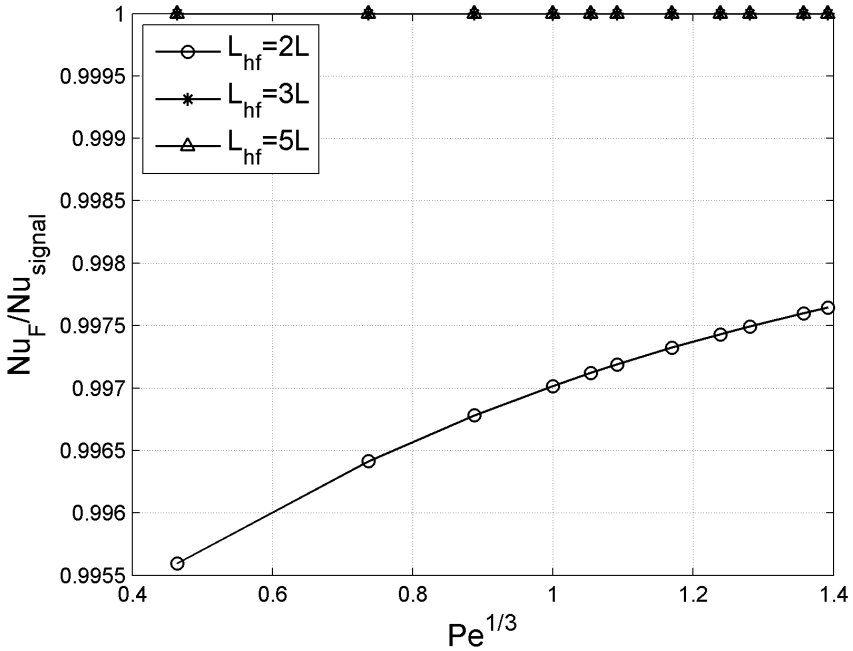

(b) Signal Quality

Figure C.2: The signal strength and signal quality of the two-plane guard-heated design in air is compared between different designs, with different guard-heater lengths. The results show that a smaller guard-heater can be used to increase the signal strength and yet maintain a high signal quality.

C.2 Extended Range of Peclet Number

This section includes results of steady runs in a wide range of Peclet numbers for reference. The Peclet number in all plots changes from $Pe = 0.1$ to $Pe = 1000$. Since different sensor lengths or pipe Reynolds numbers result in different values of Peclet number, these plots can be used to study the behaviour of the sensors for given flow conditions.

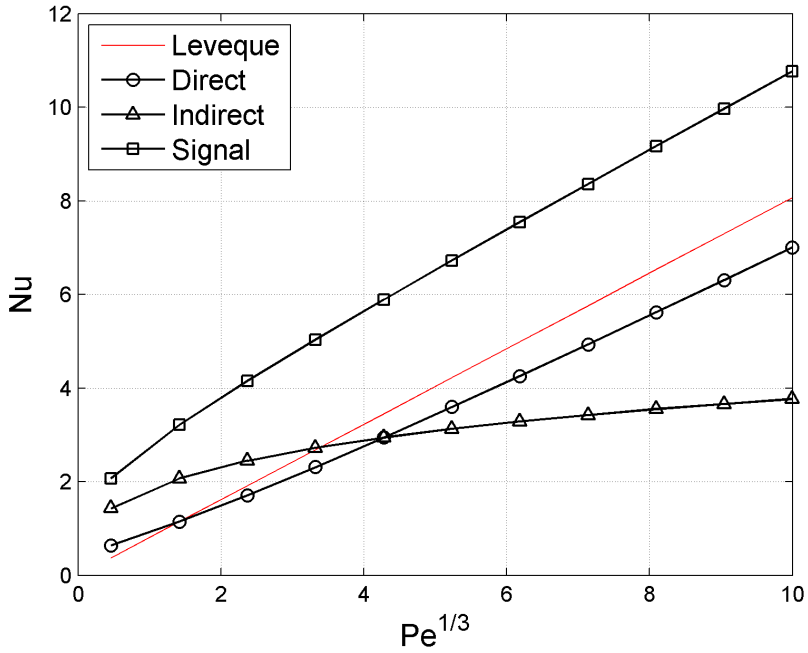

(a) Water

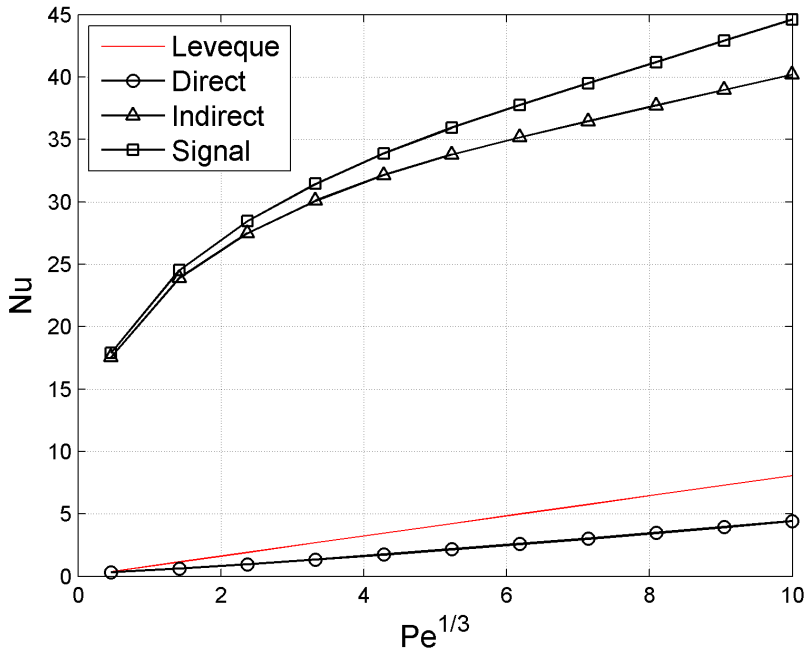

(b) Air

Figure C.3: Direct (Nu_F), indirect (Nu_S) and signal (Nu_{signal}) heat transfer rates vs. $Pe^{1/3}$ for the SE sensor design.

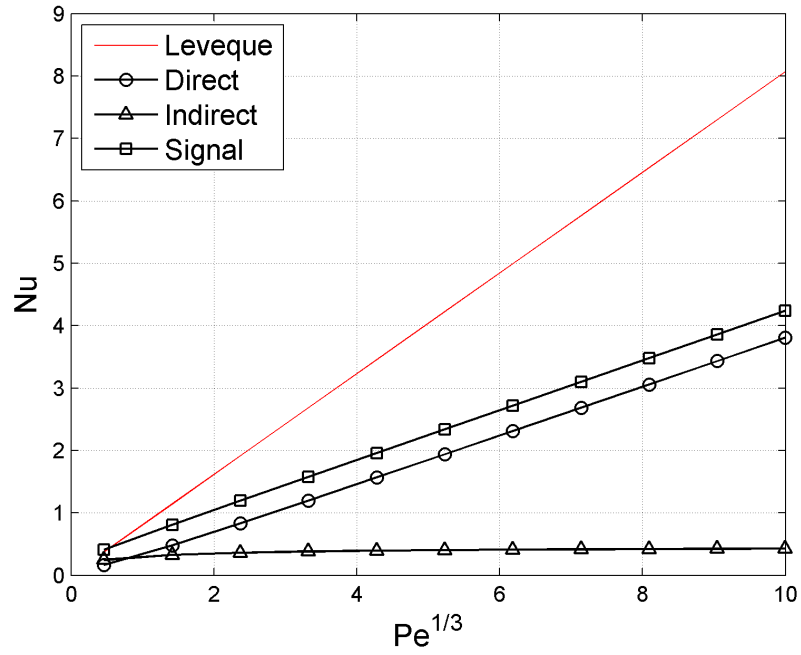

(a) Water

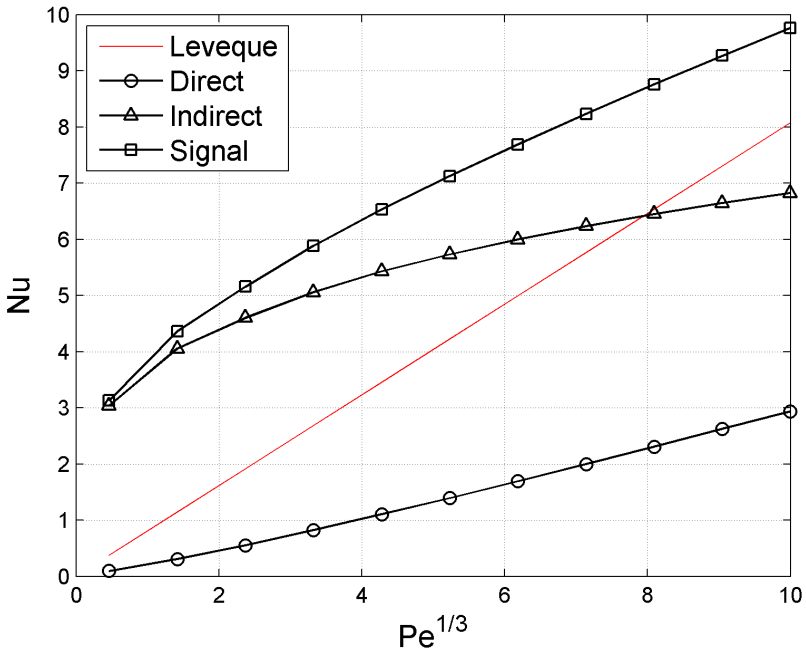

(b) Air

Figure C.4: Direct (Nu_F), indirect (Nu_S) and signal (Nu_{signal}) heat transfer rates vs. $Pe^{1/3}$ for the $GH1P$ sensor design.

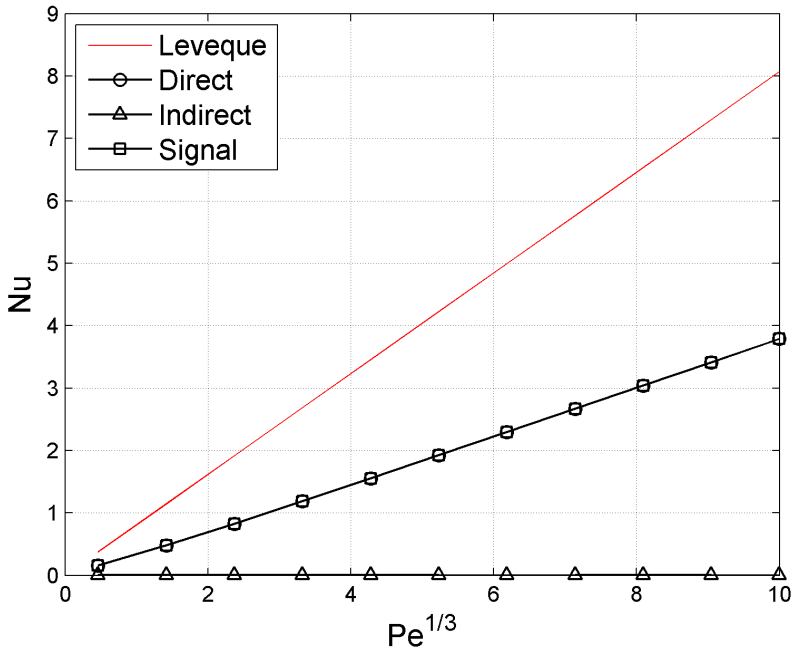

(a) Water

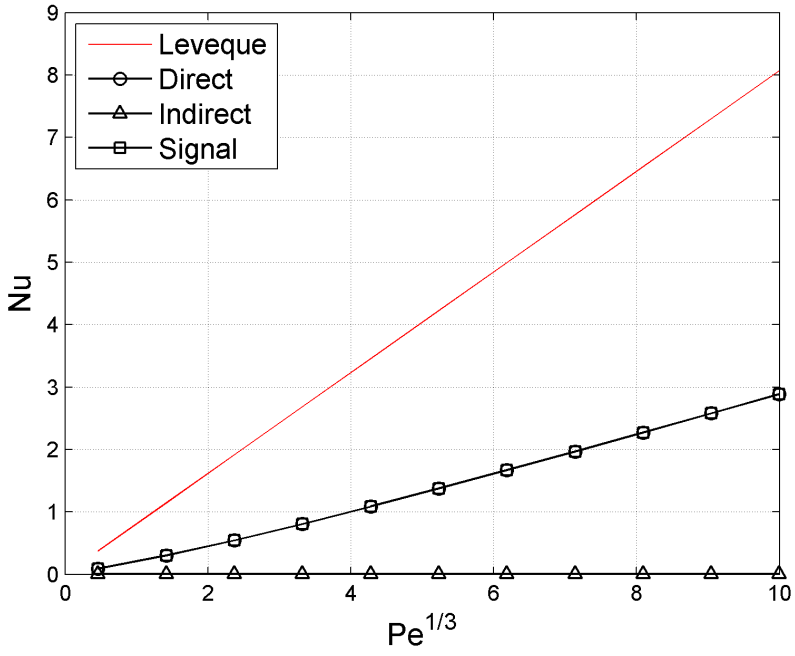

(b) Air

Figure C.5: Direct (Nu_F), indirect (Nu_S) and signal (Nu_{signal}) heat transfer rates vs. $Pe^{1/3}$ for the $GH2P$ sensor design.

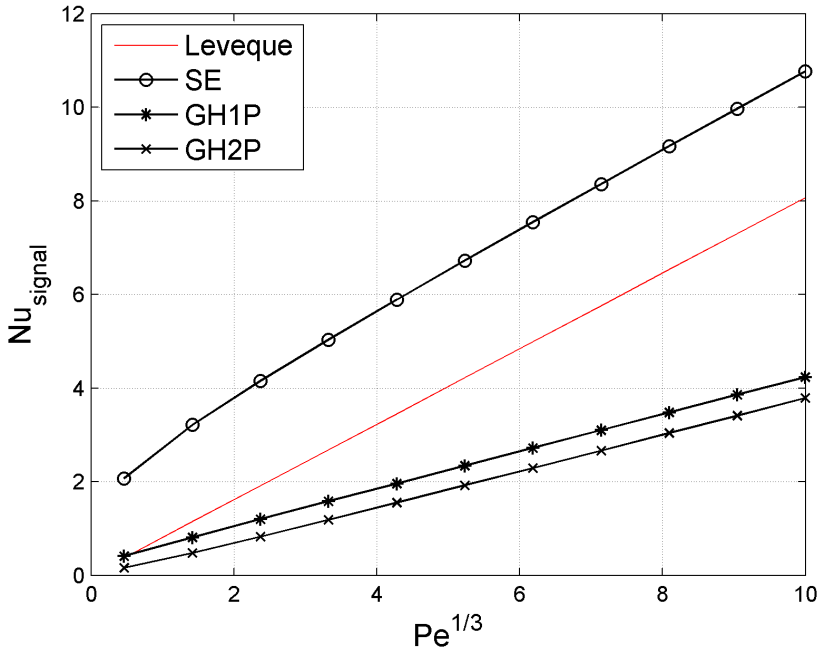

(a) Water

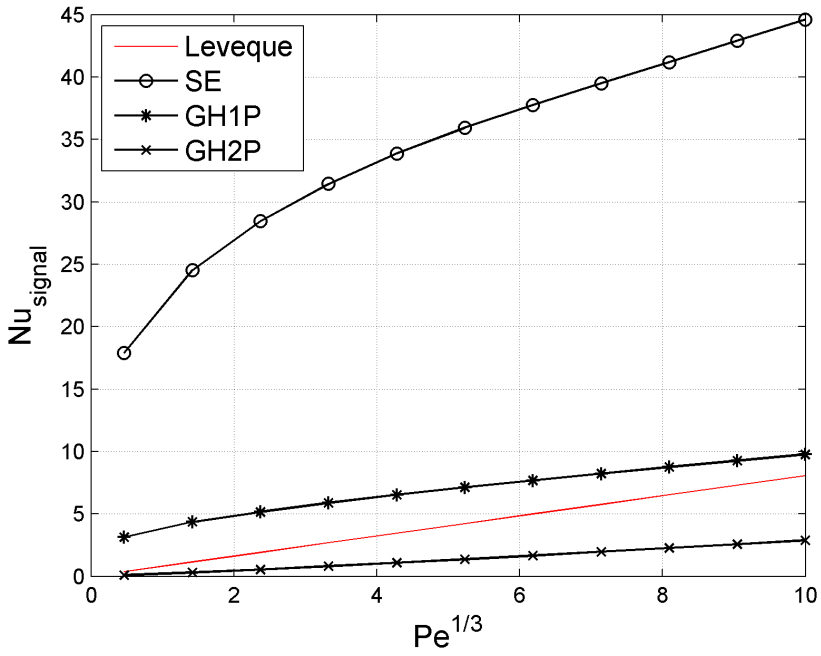

(b) Air

Figure C.6: Signal heat transfer rate (Nu_{signal}) vs. $Pe^{1/3}$ for different sensor designs.

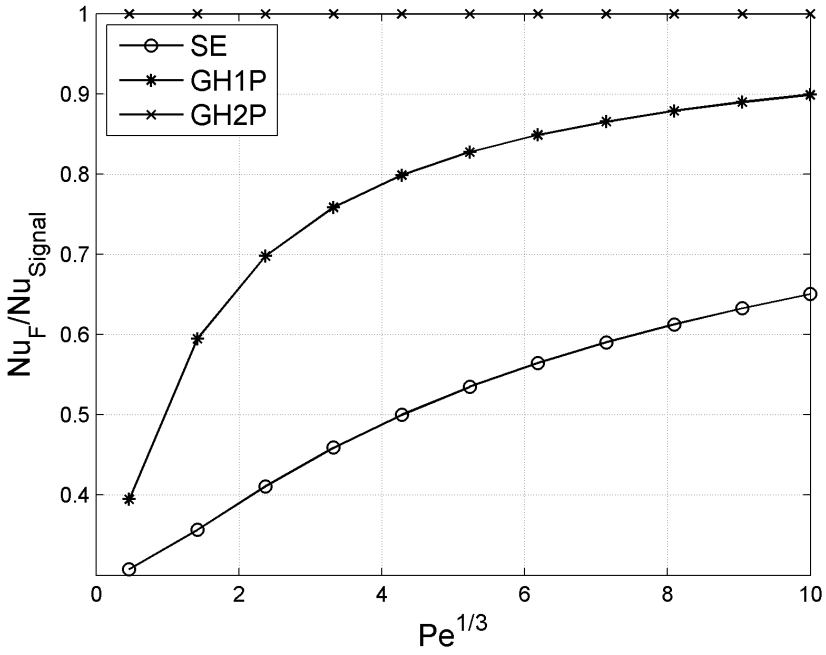

(a) Water

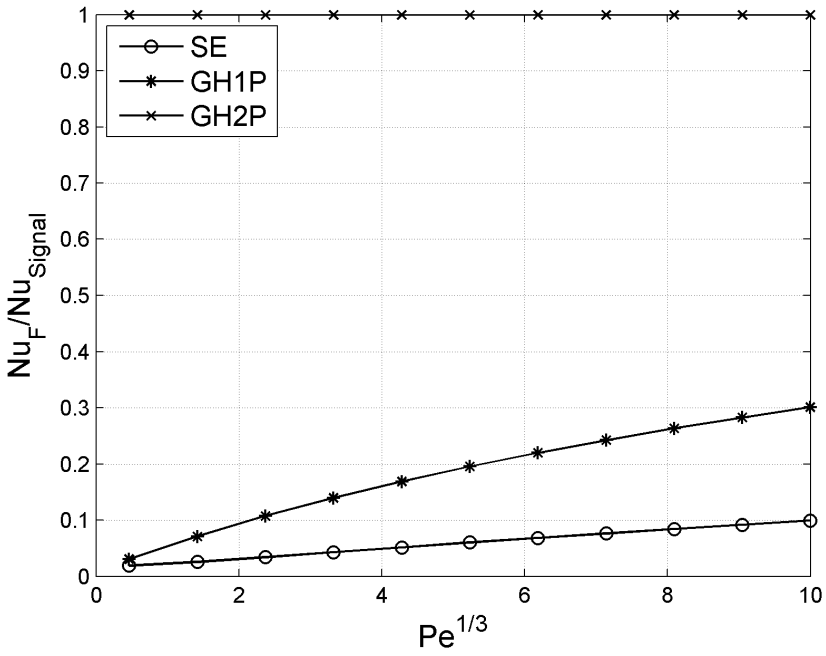

(b) Air

Figure C.7: Direct-to-signal heat transfer ratio vs. $Pe^{1/3}$ for different sensor designs.

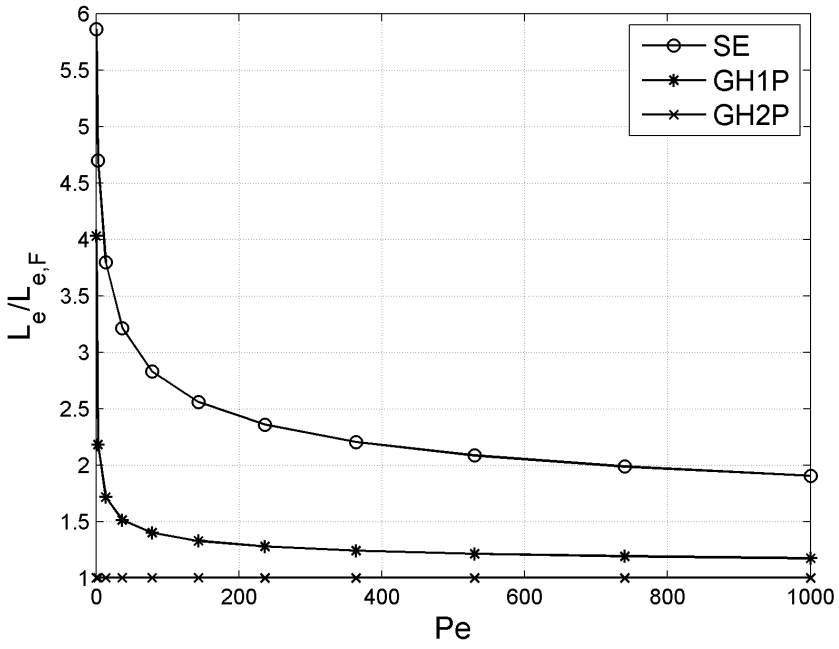

(a) Water

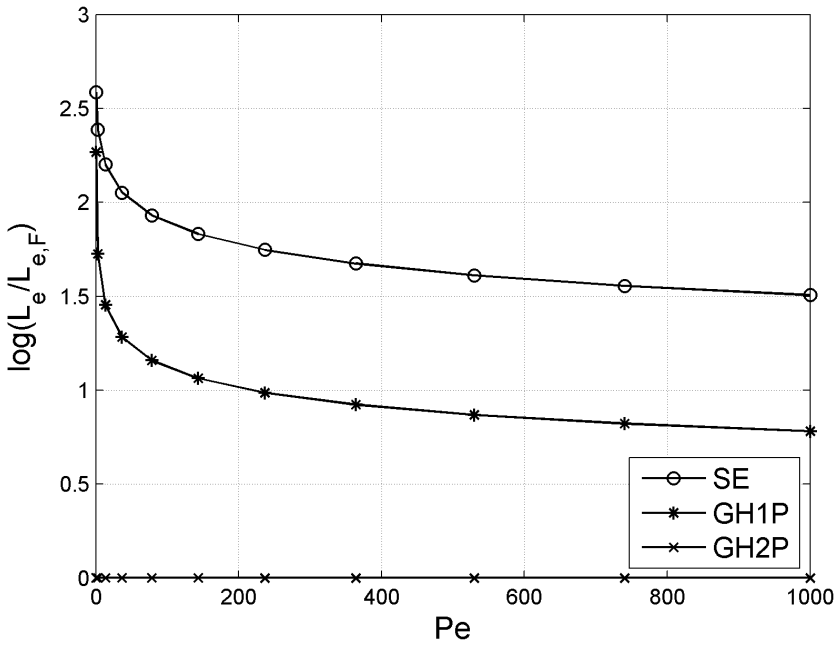

(b) Air

Figure C.8: The ratio of the equivalent length based on total heat transfer rate L_e and the equivalent length based on direct heat transfer rate $L_{e,F}$ vs. Pe for different designs. $L_e/L_{e,F}$ great than 1 means loss of spatial resolution.